



The
University
Of
Sheffield.

On the Optimization of PV Cells' Orientation Angles and Their Deployment at Base Stations for Energy-efficient Cellular Networks

By:

Doris Christine Benda

A thesis submitted in partial fulfillment of the requirements
for the degree of Doctor of Philosophy

The University of Sheffield
Faculty of Engineering
Department of Electronic & Electrical Engineering

Submission Date: September 27, 2019

Abstract

The inherent problem of solar-powered base stations (BSs) will be tackled in this thesis, i.e., the problem that the energy generation of the photovoltaic (PV) cells does not match the energy consumption of the BS in time, which results in energy being wasted.

In Chapter 1, a comprehensive literature review is given.

In Chapter 2, the orientation angles of N PV cells powering one BS are jointly optimized to improve the match between the two profiles on a daily timescale. The energy generation profiles of randomly inclined and oriented PV cells are analytically derived based on the Reindl model. The energy drawn per day from the main grid by the BS given its energy consumption profile is used as the performance metric to determine the optimal set of orientation angles. The main results are that deploying one PV cell (or several PV cells) with the (same) optimized orientation angle is recommended for BSs with an energy consumption profile that has one significant local maximum between sunrise and sunset. Deploying two PV cells (or two equal-sized groups of PV cells) where the two orientation angles (of the two groups) are jointly optimized is recommended for BSs with an energy consumption profile that has significant local maxima in the morning as well as in the afternoon or with a constant energy consumption profile.

In Chapter 3, a battery model is added to the system model. The battery model is based on a Markov chain. The effects of different battery capacities on the optimal PV cell orientation angle are investigated. It is shown that PV cell orientation angle optimization should be done for BSs deployed with small batteries.

In Chapter 4, the system model is extended to a multi-cell cellular network and a mixed-integer linear programming problem is developed to determine how energy harvesters with anti-correlated energy generation profiles should be deployed to every BS.

In Chapter 5, the thesis is concluded.

Statement of Originality

This thesis, submitted in fulfillment of the requirements for the degree of Doctor of Philosophy, is the original work of the author unless otherwise stated, while enrolled in the School of Electronic & Electrical Engineering at the University of Sheffield. The content in this thesis has not been previously submitted for the award of any other academic qualification in any other university or educational institution. Most of the results contained herein have been published in journals or conferences of international standing. The author's contribution in terms of published material is listed in the chapter "List of Publications".

These studies were conducted under the supervision of Xiaoli Chu from the University of Sheffield, Sumei Sun from the Institute for Infocomm Research in Singapore, Alastair Buckley from the University of Sheffield, and Tony Q.S. Quek from the Singapore University of Technology and Design.



Doris Benda

September 27, 2019

Date

Acknowledgements

First of all, I would like to express my sincere gratitude to my advisers Xiaoli Chu, Sumei Sun, Alastair Buckley, and Tony Q.S. Quek for their continuous support of my Ph.D. study and related research, for their constructive feedback, motivation, patience, and immense knowledge. Their guidance helped me during the time of research and writing of this thesis.

I thank my fellow Ph.D. students for the stimulating discussions, for the exchange of information, and for the companionship we have had in the last four years.

My sincere thanks also goes to the University of Sheffield and A*STAR for setting up this opportunity of doing research in two different countries and environments.

Last but not least, I would like to thank my family and friends in Germany, Sheffield, and Singapore. Special thanks go to my parents and my siblings for supporting me mentally throughout writing this thesis and my whole life.

Dedication

This work was supported by the A*STAR-Sheffield Research Attachment Programme. This work was partly funded by the European Unions Horizon 2020 Research and Innovation Programme under grant agreement No. 645705 and by the A*STAR Industrial Internet of Things Research Program under the RIE2020 IAF-PP grant A1788a0023.

List of Publications

Published journal papers:

[1] **D. Benda**, X. Chu, S. Sun, T. Q. S. Quek, and A. Buckley, “Renewable energy sharing among base stations as a min-cost-max-flow optimization problem,” *IEEE Transactions on Green Communications and Networking*, vol. 3, no. 1, pp. 67–78, March 2019.

[2] **D. Benda**, S. Sun, X. Chu, T. Q. S. Quek, and A. Buckley, “PV cell angle optimization for energy generation-consumption matching in a solar powered cellular network,” *IEEE Transactions on Green Communications and Networking*, vol. 2, no. 1, pp. 40–48, March 2018.

Published conference papers:

[3] **D. Benda**, X. Chu, S. Sun, T. Q. S. Quek, and A. Buckley, “Optimal clustering of energy-harvesting base stations,” in *Proc. IEEE VTS APWCS*, Hsinchu, Taiwan, Aug 2018.

[4] **D. Benda**, X. Chu, S. Sun, T. Q. S. Quek, and A. Buckley, “Modeling and optimization of energy sharing among base stations as a minimum-cost-maximum-flow problem,” in *Proc. IEEE VTC-Spring*, Porto, Portugal, Jun 2018.

[5] **D. Benda**, X. Chu, S. Sun, T. Q. S. Quek, and A. Buckley, “PV cell orientation angle optimization for a solar energy harvesting base station,” in *Proc. IEEE GLOBECOM*, Singapore, Dec 2017.

[6] **D. Benda**, X. Chu, S. Sun, T. Q. S. Quek, and A. Buckley, “PV cell angle optimisation for energy arrival-consumption matching in a solar energy harvesting cellular network,” in *Proc. IEEE ICC*, Paris, France, May 2017.

Submitted journal paper which is currently under review:

[7] **D. Benda**, S. Sun, X. Chu, T. Q. S. Quek, and A. Buckley, “PV cell orientation angles optimization for a base station equipped with several PV cells”, submitted to *IEEE Transactions on Green Communications and Networking*

Submitted conference paper which is currently under review:

[8] **D. Benda**, S. Sun, X. Chu, T. Q. S. Quek, and A. Buckley, “Optimal deployment of energy harvesters with anti-correlated energy generation at base stations”, submitted to *GLOBECOM 2019*

Table of Contents

Abstract	i
Statement of Originality	ii
Acknowledgements	iii
Dedication	iv
List of Publications	v
Table of Contents	vii
List of Tables	xii
List of Figures	xiii
Nomenclature	xvii
1 Introduction	1
1.1 Background	1
1.2 PV Cell Angles	3

1.3	Types of PV Cells	6
1.4	Motivation and Main Objective	8
1.5	Contributions	9
1.6	Organization	12
2	PV Cell Orientation Angles Optimization for a Base Station Equipped with Several PV Cells	14
2.1	Literature Review: Orientation Angle Optimization	14
2.2	Contributions of Chapter 2	17
2.3	System Model 1 - Several PV Cells Powering One BS	18
2.3.1	Energy Generation of a PV Cell	19
2.3.2	Ground-reflected Irradiance $I_g(t)$	22
2.3.3	Direct-beam Irradiance $I_{b_\theta}(t)$	23
2.3.4	Sky-diffuse Irradiance $I_{d_\theta}(t)$	26
2.3.5	Energy Consumption of a BS	27
2.3.6	Problem Formulation	30
2.4	Analytical Insights obtained from Section 2.3	32
2.5	Results and Discussion	35
2.5.1	Remarks on the Presentation of the Results	38
2.5.2	Summary of the Key Findings and Discussions of the Results .	49
2.6	Summary of Chapter 2	52

3 Impact of the Battery Capacity on the Optimal Orientation Angle of a PV Cell	54
3.1 Literature Review: Batteries at BSs	54
3.2 Contributions of Chapter 3	56
3.3 System Model 2 - One PV Cell Powering a BS with Battery	57
3.3.1 Solar Energy Storage Model	57
3.3.2 Energy Generation Flow and Load-independent Energy Consumption Flow	58
3.3.3 Load-dependent Energy Consumption Flow	59
3.3.4 Determination of the Average Number of Served UEs	60
3.4 Orientation Angle Optimization Algorithm with Markov Chain Based Battery	61
3.4.1 Markov Chain Initialization	62
3.4.2 Energy Generation Flow and Load-independent Energy Consumption Flow of Algorithm 1	62
3.4.3 Load-dependent Energy Consumption Flow of Algorithm 1	63
3.4.4 Determination of the Average Number of Served UEs of Algorithm 1	65
3.5 Derivation of a Simulation Algorithm as Baseline	66
3.6 Results and Discussion	67
3.6.1 Running Time of the proposed Algorithm and the Simulation Algorithm	67

3.6.2	Accuracy of the Proposed Algorithm and the Simulation Algorithm	68
3.6.3	Dependency of the Optimal PV Cell Orientation Angle on the Given Battery Capacity	70
3.7	Summary of Chapter 3	71
4	Optimal Deployment of Energy Harvesters with Anti-correlated Energy Generation Profiles at Base Stations	73
4.1	Background: Different Power Sharing Methods	74
4.1.1	Wireless Power Transfer	74
4.1.2	Traffic Offloading	74
4.1.3	Smart Grid/ Main Grid Trading	75
4.1.4	Batteries	76
4.2	Literature Review: Benefits of Anti-correlated Energy Generation . .	76
4.3	Proof of Concept	77
4.4	Contributions of Chapter 4	79
4.5	System Model 3 - Deployment of Anti-correlated Energy Harvesters .	79
4.5.1	Power Surplus/Deficit Values	80
4.5.2	Distance-dependent Power Loss in the Distribution Lines . . .	82
4.5.3	Topology of the Cellular Network	82
4.5.4	Justification of Assumptions	83
4.6	Mixed-Integer Linear Programming Problem	84

4.7	Numerical Results	87
4.8	Summary of Chapter 4	92
5	Conclusion and Future Work	93
5.1	Summary of Thesis Achievements	93
5.2	Future Work and Applications	96
	Appendix A	99
	Appendix B	104
	References	120

List of Tables

1.1	Default optimal orientation angle θ and inclination angle γ for different locations [9]	5
2.1	Input parameters of system model 1	36
2.2	Orientation angles optimization for 1 PV cell with different load profiles	40
2.3	Summary of all optimal orientation angles for 1 PV cell with the different load profiles from Table 2.2	41
2.4	Orientation angles optimization for 2 PV cells with different load profiles	43
2.5	Summary of all optimal orientation angles for 2 PV cells with the different load profiles from Table 2.4	44
2.6	Orientation angles optimization for 3 PV cells with different load profiles	47
2.7	Summary of all optimal orientation angles for 3 PV cells with the different load profiles from Table 2.6	48
3.1	Input parameters of system model 2	68
4.1	Input parameters of system model 3	87

List of Figures

1.1	Depiction of a PV cell installed with the orientation angle θ and inclination angle γ	4
1.2	Effects of the orientation angle θ on the energy generation profile of the PV cell	5
1.3	Depiction of a fixed PV cell, a single-axis sun tracking PV cell, a dual-axis sun tracking PV cell, and an adjustable PV cell	7
1.4	Example of an energy generation profile of a PV cell and an energy consumption profile of a BS to illustrate their mismatch	8
2.1	Illustration of system model 1	19
2.2	PVGIS data sheet	20
2.3	Irradiance model	22
2.4	Definition of the angle of incidence $AOI_{\theta}(t)$	24
2.5	Declination angle δ_d throughout the year	25
2.6	Definition of the hour angle ω_t	25
2.7	Hour angle ω_t throughout the day of a PV cell located on the reference meridian of its time zone	25

2.8	Constant traffic load profile, business traffic load profile, and residential traffic load profile throughout the day	28
2.9	Energy consumption profiles with constant traffic load and energy generation profiles of 2 PV cells	29
2.10	Energy consumption profiles with business-area traffic load and energy generation profiles of 2 PV cells	30
2.11	Energy consumption profiles with residential-area traffic load and energy generation profiles of 2 PV cells	30
2.12	Values of a_t , b_t , and c_t throughout one day for the spring equinox, summer solstice, autumn equinox, and winter solstice	33
2.13	Irradiance values of differently oriented PV cells in Greenwich (London, UK) and Singapore	35
3.1	Illustration of system model 2	57
3.2	Energy generation flow and load-independent energy consumption flow if $\tilde{G}_{\theta,1}(t) > c_{\text{con}}$	63
3.3	Energy generation flow and load-independent energy consumption flow if $\tilde{G}_{\theta,1}(t) < c_{\text{con}}$	63
3.4	Energy consumption flow for the battery state $\frac{c_{\text{UE}}}{\mu}$	64
3.5	Energy consumption flow for the battery state 0	64
3.6	Comparison between the proposed algorithm and the simulation algorithm. b_{max} was set at 3.	70
3.7	Average number of served UEs per day $\overline{S_{\text{UE}}}(\theta)$ vs. PV cell orientation angle θ for different battery capacities b_{max}	71

4.1	Demonstration of the concept of energy harvesters with anti-correlated energy generation profiles	78
4.2	Illustration of the considered cellular network	81
4.3	The graph representation of the cellular network	81
4.4	Average normalized renewable power received at the deficit BSs M of the proposed MILPP and of random BS cluster allocation vs. number of BSs B	88
4.5	Average normalized renewable power received at the deficit BSs M of the proposed MILPP and of random BS cluster allocation vs. distribution line existence probability q	89
4.6	Average normalized renewable power received at the deficit BSs M of the proposed MILPP and of random BS cluster allocation vs. power loss coefficient per l meters of distribution line C	90
4.7	Average normalized renewable power received at the deficit BSs M of the proposed MILPP and of random BS cluster allocation vs. power surplus value b_0	91
1	PVGIS data sheet from [10]. γ is set at 36° , θ is set at 0° , month is set at June, and the location is Greenwich ($lat = 51.4767^\circ$ North, $lon = 0.0003^\circ$ West).	100
2	Normalized energy generation profiles of a southeast-oriented, south-oriented, and southwest-oriented PV cell. Each of the PV cells is covering the total surface area $A = 5\text{m}^2$. The south-oriented PV cell generates at noon the most energy among all orientation angle settings and among all time steps throughout the day. This normalized peak energy generation is exactly 1 unit of normalized energy.	101

3	Energy generation profile $G_{0^e,1}^{\text{original}}(t)$ and energy consumption profile $C^{\text{original}}(t)$ before normalization.	102
4	Energy generation profile $G_{0^e,1}(t)$ and energy consumption profile $C(t)$ after normalization.	103

Nomenclature

Greek Letters

α	Albedo of ground
γ	Inclination angle of PV cell, $\gamma \in [0^\circ, 90^\circ]$
Δ_1	Gain of adding the 1 st PV cell, cf. (2.26)
Δ_n	Gain of adding the n^{th} PV cell, $n \in \{2, \dots, N\}$, cf. (2.25)
δ_d	Declination angle, cf. (2.11)
ζ_t	Zenith angle, cf. (2.13)
η	Energy conversion efficiency of PV cell
θ	Orientation angle of PV cell, $\theta \in [-90^\circ, 90^\circ]$
θ^*	Optimal orientation angle of PV cell, $\theta^* \in [-90^\circ, 90^\circ]$
θ_n	Orientation angle of PV cell n , $\theta_n \in [-90^\circ, 90^\circ]$
θ_n^*	Optimal orientation angle of PV cell n , $\theta_n^* \in [-90^\circ, 90^\circ]$
$\lambda(t)$	Density parameter of Poisson distributed random variable at time step t , cf. (3.4)
μ	Precision of the discretization of the energy values/ battery states
ρ	Resistivity of the distribution line

τ Duration of one time step

ω_t Hour angle, cf. Figure 2.7

Roman Letters - Upper Case

A Total surface area of N PV cells

A_c Cross-sectional area of the distribution line

A_t Anisotropy index at time step t , cf. (2.14)

$AOI_\theta(t)$ Angle of incidence of a PV cell deployed with orientation angle θ at time step t , cf. (2.7)

B Number of BSs in the square area of l^2 square meters, cf. Figure 4.2

BS_i BS with index i

C Power loss coefficient per l meters of distribution line

$C(t)$ Energy consumption of the BS at time step t , cf. Figures 2.9 - 2.11

$C_{\text{bus}}(t)$ Business-area traffic load profile at time step t , cf. Figure 2.8

$C_{\text{con}}(t)$ Constant traffic load profile at time step t , cf. Figure 2.8

$C_{\text{res}}(t)$ Residential-area traffic load profile at time step t , cf. Figure 2.8

DHI_t Diffuse horizontal irradiance at time step t , obtained from PVGIS [10]

DNI_t Direct normal irradiance at time step t , obtained from PVGIS [10]

E Set of edges in the graph/cellular network, cf. (4.4)

E_{con} Solar constant set at $1367 \frac{\text{W}}{\text{m}^2}$ [11]

E_d	Extraterrestrial radiation on day d , cf. (2.15)
$G(t)$	Energy generation of the PV cell/cells at time step t
$G_{\theta,N}^{\text{original}}(t)$	Energy generated by one PV cell installed with θ (N is the total number of PV cells) at time step t , cf. (2.1)
$G_{\theta,N}(t)$	Normalized energy generated by one PV cell installed with θ (N is the total number of PV cells) at time step t , cf. (2.2)
$\tilde{G}_{\theta,1}(t)$	Closest multiple of μ from $G_{\theta,1}(t)$
$G_{(\theta_1,\dots,\theta_N)}(t)$	Normalized total energy generated by N PV cells installed with $\theta_1, \dots, \theta_N$ at time step t , cf. (2.3)
GHI_t	Global horizontal irradiance at time step t , obtained from PVGIS [10]
$I_{\theta}(t)$	Irradiance on PV cell installed with orientation angle θ at time step t , cf. (2.4)
$I_{b_{\theta}}(t)$	Direct-beam irradiance at time step t , cf. (2.6)
$I_{d_{\theta}}(t)$	Sky-diffuse irradiance at time step t , cf. (2.12)
$I_g(t)$	Ground-reflected irradiance at time step t , cf. (2.5)
I_{ele}	Electric current traveling through the distribution line
L	Number of loops in simulation algorithm
M	Total normalized renewable power received at the deficit BSs during the two time steps
N	Number of PV cells at the BS
P_{loss}	Power loss in the transmission due to resistive heating, cf. (4.3)
S_{max}	Number of battery energy states, cf. (Algorithm 1 line: 5)

S_{Shift}	New battery state after $\tilde{G}_{\theta,1}(t)$ is added and c_{con} is subtracted, cf. (Algorithm 1 line: 16)
$S_{\text{UE}}(\theta)$	Number of UEs served per day by the BS, cf. (3.8)
$\overline{S_{\text{UE}}}(\theta)$	Average number of UEs served per day by the BS, cf. (3.8)
T	Number of time steps per day
V	Set of vertices in the graph/ cellular network, cf. (4.4)
V_{ele}	Electric potential in the distribution line

Roman Letters - Lower Case

$a_{\theta}(t)$	Available energy in the battery at the beginning of time step t , cf. (3.1)
a_t	Part of $\cos(AOI_{\theta}(t))$ that is independent of θ , cf. (2.8)
b_t	Part of $\cos(AOI_{\theta}(t))$ that is multiplied by $\sin(\theta)$, cf. (2.9)
$b_{\theta}(t)$	Stored energy in the battery at the end of time step t , cf. (3.7)
b_{begin}	Amount of energy stored in the battery at time step 0
b_{max}	Battery capacity
b_0	Power surplus value, $b_0 \in \mathbb{R}^+$
b_1	Power deficit value, $b_1 \in \mathbb{R}^-$
\hat{b}_0	Normalize power surplus value with respect to $\max\{b_0, b_1 \}$, cf. (4.5)
\hat{b}_1	Normalize power deficit value with respect to $\max\{b_0, b_1 \}$, cf. (4.5)
$c_{\theta}(t)$	Load-dependent energy consumption of the BS at time step t , cf. (3.6)

c_{con}	Load-independent part of the energy consumption at the BS in one time step
c_i	Cluster allocation value of BS_i , $c_i \in \{0, 1\}$
c_t	Part of $\cos(AOI_\theta(t))$ that is multiplied by $\cos(\theta)$, cf. (2.10)
c_{UE}	Average energy consumption of the BS to serve one UE during a time step
d	Day of the year with 1 st of January is $d = 1$
$d((i, j))$	Normalize Euclidean distance between BS_i and BS_j with respect to l meters, cf. (4.2)
e	Edge e in a graph
$f^t((i, j))$	Power flow on the directed edge from BS_i to BS_j at time step t or second power of the current flow on the directed edge from BS_i to BS_j at time step t
$\hat{f}^t((i, j))$	Normalize power flow value with respect to $\max\{b_0, b_1 \}$ on the directed edge from BS_i to BS_j at time step t , cf. (4.5)
$f(\theta_1, \dots, \theta_N)$	Normalized energy drawn from the grid, Optimization objective, cf. (2.20)
l	Side length of the square in Fig 4.2
lat	Latitude of location
lon	Longitude of location
$l(t)$	Number of UEs connected to the BS at time step t , cf. (3.3)
n	Index of BS, $n \in \{1, \dots, N\}$
p_i^t	Surplus/Deficit power of BS_i at time step t , cf. (4.1)

q Probability that two BSs are connected by a distribution line,
 $q \in [0, 1]$

$s_\theta(t)$ Number of served UEs by the BS at time step t , cf. (3.5)

t Index of time step, $t \in \{1, \dots, T\}$

v Vertex v in a graph

Superscripts

*

Optimal value

Subscripts

θ Parameter depends on the PV cell orientation angle θ

d Parameter depends on the day of the year with 1st of January is
 $d = 1$

i Index of BS, $i \in \{1, \dots, B\}$

j Index of BS, $j \in \{1, \dots, B\}$

n Index of PV cell, $n \in \{1, \dots, N\}$

t Index of time step, $t \in \{1, \dots, T\}$

Other Symbols

\forall For all

$n!$ Factorial of non-negative integer n , $n \in \mathbb{N}_0$

$\lceil x \rceil$ x is rounded to the nearest integer value

$\lfloor x \rfloor$ x is rounded down to the nearest integer value

\mathbb{N} Set of natural numbers

\mathbb{R} Set of real numbers

\mathbb{Z}	Set of integer numbers
$\mathbb{P}(X = x)$	Probability that the random variable X is equal to x
$\mathbb{P}(X \geq x)$	Probability that the random variable X is not less than the value x
$X := \text{PD}(\lambda)$	X is a Poisson distributed random variable with density parameter λ
$G \ll C$	Energy generation of PV cell/cells is significantly smaller than energy consumption of BS
$G < C$	Energy generation of PV cell/cells is slightly smaller than energy consumption of BS
$G > C$	Energy generation of PV cell/cells is slightly greater than energy consumption of BS
$G \gg C$	Energy generation of PV cell/cells is significantly greater than energy consumption of BS
$\ BS_i - BS_j\ $	Euclidean distance between BS_i and BS_j
(i, j)	Directed edge from BS_i to BS_j

Acronyms / Abbreviations

A*STAR	Agency for Science, Technology and Research in Singapore
AC	Alternating current
BS	Base station
DC	Direct current
GIS	Geographic information system
MILPP	Mixed-integer linear programming problem

PV	Photovoltaic
PVGIS	Photovoltaic geographic information system
SINR	Signal-to-interference-plus-noise ratio
UE	User equipment

Chapter 1

Introduction

1.1 Background

The information and communications industry accounts for 3% of the global electricity costs with an annual increase rate of 15 - 20% [12]. Base stations are responsible for more than half of the energy costs in the cellular network infrastructure [13], indicating a huge demand to take advantage of renewable energy generation. Many countries have set green taxation and incentive schemes to achieve ambitious CO_2 emission reduction targets, making renewable energy harvesting technologies attractive for cellular network operators. Experts estimated that energy harvesting technology can reduce 20% of the CO_2 emissions in the information and communications industry [14].

Data traffic in cellular networks is growing rapidly [15]. Recently, the traffic is growing 70 – 200% per year [16]. As a result, base station (BS) densification is necessary for the implementation of 5G cellular networks and future generations of cellular networks [17]. Dense deployment of BSs can meet the increasing traffic demand of new applications, such as ultra high definition video streaming, autonomous driving, and virtual reality based applications [18]. As a consequence, the accumulated BS energy consumption is rising considerably. To alleviate the impact on the envi-

ronment and the cost burden on cellular network operators, photovoltaic (PV) cell powered BSs have been considered for future cellular networks [13,14,19]. PV cells have been used for considerable time to power stand-alone BSs, which have no main grid connectivity [20]. Compared with other renewable energy technologies, PV cells are often chosen to power a BS due to their small physical footprint in dense built environments, technology maturity, low maintenance cost, and production cost reduction in recent years [14].

Main grid energy is always on demand. In contrast, profiles of renewable energy harvesters have significant spatial [21] and temporal variations [22]. In addition, the energy consumption profile of a BS is linked to the traffic load profile of the deployment area. For example, if the BS is located in a residential area, and in a business area, the energy consumption peak of the BS is at 23:00, and 11:30, respectively [23]. Consequently, the energy generation profile of a PV cell does not match the energy consumption profile of a BS in general [24]. The most common solutions to this problem reported in the literature are either energy storage technologies, such as batteries, supply side management, or demand side management [25].

This paragraph will highlight why demand side management is extremely difficult in a cellular network context. Demand side management at a BS is challenging, because it would imply to change the behavior of the users in terms of that they use their UEs at different times of the day or night. Users value cellular network services because of their convenience and always on demand property. A cellular network which is not always on demand would negatively affect the quality of service that the users expect from it. In more detail, that a BS needs less energy at a specific time of the day, fewer UEs have to request service, or less energy demanding jobs have to be requested by the UEs. This would mean in practice that users should use their UEs not during the day but rather at 3 am in the night or that users should not live screen ultra high definition videos but rather download videos in advance at 3 am in the night. Such a behavioral change is unlikely to happen due to the nature of the circadian rhythm of the human being. In addition, using a UE is often

an impulse decision rather than a several hours in advanced planned decision.

Since demand side management is not an effective solution in a cellular network context, this thesis will focus on supply side management by deriving a new methodology based on orientation angle optimization to adjust the solar energy supply to meet the energy demand of the BS in the time domain. In addition, energy storage technologies, such as batteries, will also be evaluated in Chapter 3 in this thesis.

1.2 PV Cell Angles

Section 1.2 will define the two PV cell angles that are commonly used in the solar industry, which are denoted by orientation angle and inclination angle in this thesis. All angles in this thesis are in degrees. Hence, all derived formulas, expressions, and statements in this thesis are given with respect to degrees and not radians.

As shown in Figure 1.1, the inclination angle of a PV cell, denoted by γ , is defined as the angle between the horizontal plane and the PV cell plane. The orientation angle of a PV cell, denoted by θ , is defined with respect to the southern direction. Orientating the PV cell to the east (west) is indicated by a negative (positive) algebraic sign added to the orientation angle. For instance, the orientation angles of a PV cell orientated towards the east, south, and west are $\theta = -90^\circ$, $\theta = 0^\circ$, and $\theta = 90^\circ$, respectively.

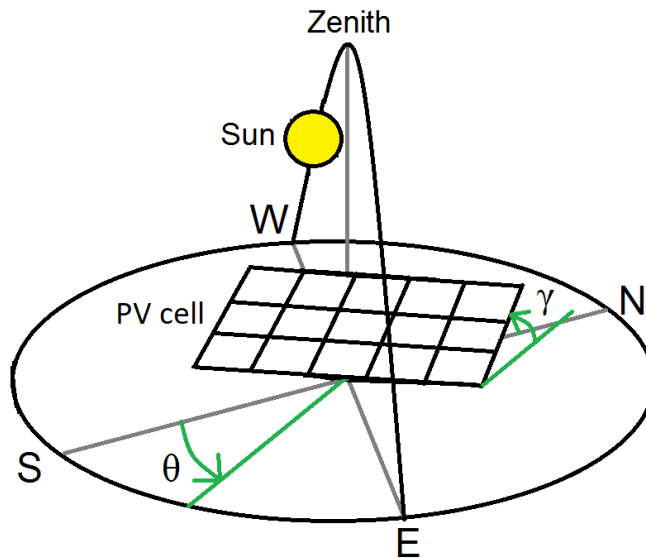


Figure 1.1: Depiction of a PV cell installed with the orientation angle $\theta = -30^\circ$ and inclination angle $\gamma = 20^\circ$

The daily energy generation profile of a PV cell depends on the day of the year, the deployment location, the orientation angle θ , and the inclination angle γ of the PV cell.

The orientation and inclination angles of PV cells are usually fixed after the initial installation. Therefore, it is necessary to optimize the orientation and inclination angles of PV cells prior to the deployment. Without considering the energy consumption profile of the appliance, PV cells are deployed with default angles that are derived from the PV cell's geographic location as summarized in Table 1.1. The default inclination angle is set at a value similar to the latitude of the deployment area, and the default orientation angle is 0° , and 180° in the northern, and southern hemispheres, respectively [9]. Deploying PV cells with the default angles from Table 1.1 guarantees that the PV cells harvest the most energy on a yearly timescale among all possible orientation and inclination angles.

Table 1.1:
Default optimal orientation angle θ and inclination angle γ for different locations [9]

Location	θ	γ
Northern hemisphere	0°	similar to the location's latitude
Southern hemisphere	180°	similar to the location's latitude
Equator	any orientation angle	0°

This paragraph will investigate how the shape of the energy generation profile changes for different orientation angles on a daily timescale. Figure 1.2 shows the daily energy generation profiles of southeast-oriented, south-oriented, and southwest-oriented PV cells, which are denoted by $G_{-45^\circ,1}(t)$, $G_{0^\circ,1}(t)$, and $G_{45^\circ,1}(t)$, respectively, for Greenwich (London, UK) during the summer. Orientating a PV cell eastwards (westwards) shifts the energy generation profile towards the morning (afternoon) hours in the northern hemisphere. The farther a PV cell is oriented away from the southern direction the less energy it harvests throughout the day. In other words, the more the energy generation profile peak is shifted away from noon the less energy is produced by the PV cell throughout the day. This tradeoff will be addressed in this thesis to determine the optimal orientation angle.

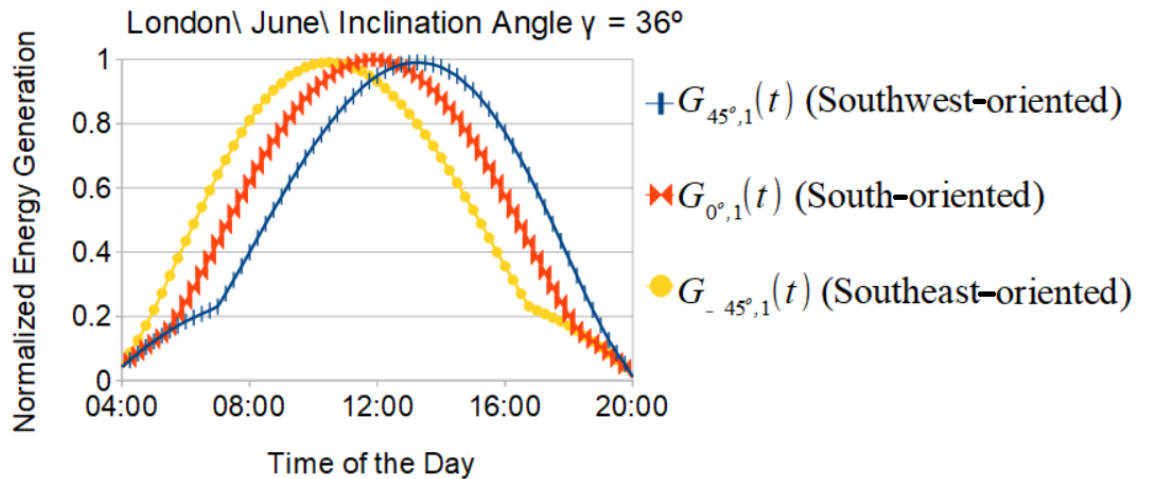


Figure 1.2: Effects of the orientation angle θ on the energy generation profile of the PV cell

Optimizing the PV cell orientation angle is done on a daily timescale because it is a method to shift the energy generation peak from a surplus time (e.g. noon)

to a deficit time (e.g. morning or afternoon), as seen in Figure 1.2. In contrast, optimizing the PV cell inclination angle is done on a yearly timescale because it is a method to shift the energy generation peak from a surplus season (e.g. summer) to a deficit season (e.g. winter). The focus of this thesis is to match the daily energy consumption profile of a BS with the daily energy generation profile of several PV cells. Hence, the orientation angles will be optimized in this thesis because the orientation angles affect the shape of the energy generation profile on a daily timescale.

1.3 Types of PV Cells

PV cells can be classified into fixed, sun tracking, and adjustable PV cells (cf. Figure 1.3). A fixed PV cell (cf. Figure 1.3(a)) has fixed orientation and inclination angles which cannot be changed anymore after the initial installation. A single-axis sun tracking PV cell (cf. Figure 1.3(b)) can mechanically track the sun throughout the day via adjusting the orientation angle. The single-axis sun tracking PV cell improves herein its daily energy yield compared with a fixed PV cell. A dual-axis sun tracking PV cell (cf. Figure 1.3(c)) can mechanically track the sun throughout the day and the season, e.g., winter and summer, via adjusting both the orientation and inclination angles. The dual-axis sun tracking PV cell improves herein its yearly energy yield compared with a single-axis sun tracking PV cell.

Despite the potentially higher energy yield of sun tracking PV cells than fixed PV cells, they are currently not widely deployed. The reasons are mainly the additional parts needed (e.g. axis motor), the higher maintenance (e.g. mechanical parts like the axis and the motor break more often than static parts), and the energy needed to operate the axis motor, which can be higher than the additional energy generated due to the sun tracking for some locations [26].

An adjustable PV cell (cf. Figure 1.3(d)) requires an engineer to visit the site several

times throughout the year to adjust the angles manually. Frequent (infrequent) adjustments of the angles will result in higher (lower) operational expenditure in combination with a higher (lower) energy yield of the PV cell. Due to the high wages in many countries, the increasing number of BSs in future cellular networks, and the problem that many BSs are difficult to access (e.g. on top of buildings or mountains), fixed PV cells are more suitable for powering BSs than adjustable PV cells. Hence, this thesis will focus on orientation angle optimization of fixed PV cells. Nonetheless, the derived optimization process in this thesis can equivalently be used to optimize the orientation angles of adjustable PV cells. For example, if the optimization method in this thesis is done on two days throughout the year (e.g. one day in winter, and one day in summer), the two derived optimal orientation angles can be altered every 6 months. The engineer should change the orientation angles of the adjustable PV cells during spring equinox and autumn equinox every year for this example. In general, fixed PV cells can be seen as a special case of an adjustable PV cell that does not require additional visits of engineers after its initial installation.

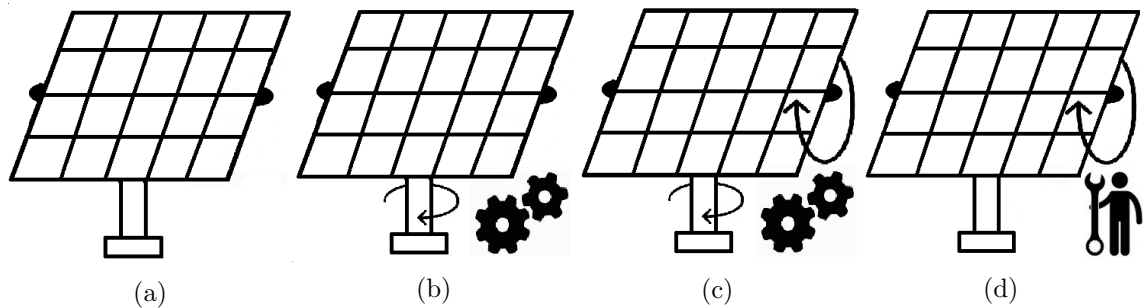


Figure 1.3: Depiction of a fixed PV cell (a), a single-axis sun tracking PV cell (b), a dual-axis sun tracking PV cell (c), and an adjustable PV cell (d)

1.4 Motivation and Main Objective

In general, there is a mismatch between the daily energy generation profile of PV cells and the daily energy consumption profile of a BS, as seen in Figure 1.4. The profiles in Figure 1.4 are given as an example in this paragraph. Many different types of energy generation profiles, and energy consumption profiles typical for PV cells, and typical for BSs will be evaluated in the following chapters, respectively.

The objective of this thesis is to develop a method to shift the surplus energy (green color area in Figure 1.4) to the deficit period (gray color area in Figure 1.4). This thesis will derive a new methodology based on orientation angle optimization to adjust the solar energy supply to meet the energy demand of the BS in the time domain (black arrow in Figure 1.4). This is the main objective of this thesis and will be presented in Chapter 2.

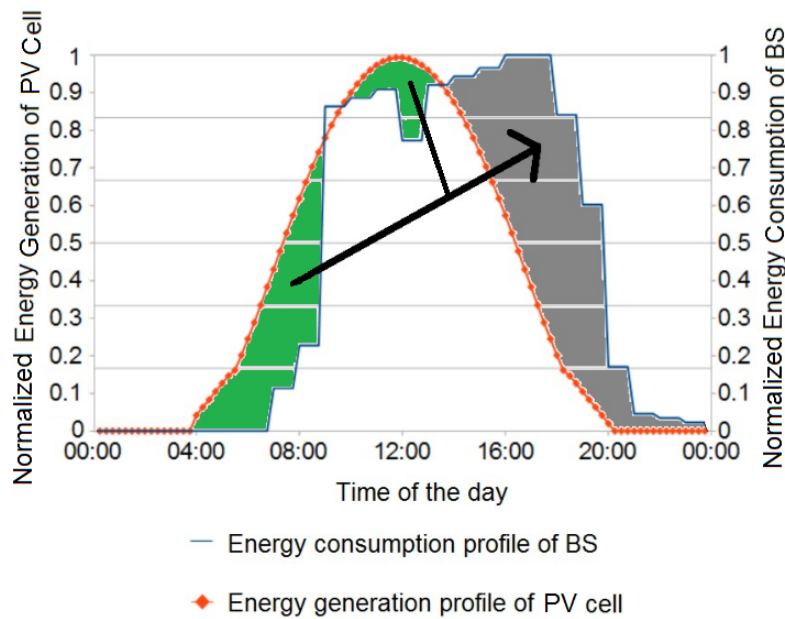


Figure 1.4: Example of an energy generation profile of a PV cell and an energy consumption profile of a BS to illustrate their mismatch

1.5 Contributions

This section will summarize the main contributions of Chapter 2, Chapter 3, and Chapter 4.

Contributions of Chapter 2:

- Developing an algorithm to jointly optimize the orientation angles of several PV cells powering one BS. The algorithm achieves the best possible match between the energy generation profiles of the PV cells and the energy consumption profile of the BS. The proposed optimization algorithm only needs to be run a single time offline and the obtained optimal angles can be used for all solar-powered BSs with similar geographic locations and energy consumption profiles.
- Deriving analytically the irradiance values on any randomly inclined and oriented PV cell. A horizontally-mounted PV cell is used as a baseline and its irradiance values have to be given to derive the irradiance values on any randomly inclined and oriented PV cell at the same location.
- Identifying and discussing analytically to what extent the orientation angle θ shifts the energy generation profile away from noon if the PV cells are not south-oriented ($\theta \neq 0^\circ$).
- Evaluating the effectiveness of the proposed orientation angle optimization on three different types of BS energy consumption profiles: constant traffic load profiles, business-area traffic load profiles, and residential-area traffic load profiles. The energy drawn from the main grid by the BS per day is used as the performance metric.
- Giving recommendations on how many differently oriented PV cells should be deployed for a given energy consumption profile. To the best of my knowledge, this has never been investigated in the literature before.

Contributions of Chapter 3:

- Developing a PV cell's orientation angle optimization algorithm with Markov chain based battery model of a solar-powered BS with battery. The algorithm takes into account the battery capacity and the energy consumption profile of the BS. The number of user equipments (UEs) served by the BS throughout the day $\overline{S_{\text{UE}}}(\theta)$ is used as the performance metric to identify the optimal orientation angle.
- Verifying the accuracy of the proposed algorithm by showing that simulation trials converge based on the law of large numbers to the output $\overline{S_{\text{UE}}}(\theta)$ of the proposed algorithm.
- Showing that the proposed algorithm (depends on the number of battery states) requires a shorter running time than the simulation trials (depends on the number of trials) for moderate battery state resolutions.
- Investigating the dependency of the optimal PV cell orientation angle on the given battery capacity.

Contributions of Chapter 4:

- Developing an optimization algorithm that can be run once during the cellular network planning to determine what type of energy harvesters should be deployed to every BS in a cellular network. There are two different types of energy harvesters available for deployment which have anti-correlated energy generation profiles.
- Taking into account the topology of the cellular network as well as the distance-dependent power loss in the distribution lines during the optimization.
- Developing an optimization objective that maximizes the power that can be transmitted from surplus BSs to deficit BSs in the cellular network.

- Comparing the proposed optimization algorithm with randomly deploying anti-correlated energy harvesters to the BSs. The effects of different numbers of BSs, different distribution line existence probabilities, different distribution line power loss coefficients, and different power surplus values are investigated.

1.6 Organization

This section will present the organization of the thesis in detail. Section 1.1 gives a general overview of the developments and emerging problems in future cellular networks and how solar-powered BSs can alleviate these emerging issues. Section 1.2 defines the orientation and inclination angles of the PV cells and provides a basic rule of thumb how these angles should be chosen based on the geographical location of the PV cell. This rule of thumb only maximizes the yearly energy output of the PV cell but it cannot take into account the energy consumption profile of the appliance. Section 1.3 justifies the focus on fixed PV cells with respect to other types of PV cells in this thesis. Section 1.4, Section 1.5, and Section 1.6 present the main objectives, the contributions, and the organization of this thesis, respectively. Chapter 2, Chapter 3, and Chapter 4 are the main parts of this thesis and are based on my published papers. Each of the three chapters develops a system model to address and to evaluate a specific problem explained in more detail later. Guidelines and key findings are summarized at the end of each chapter.

Chapter 2 addresses the main objective of this thesis. It develops a methodology to jointly optimize the orientation angles of several PV cells at one BS so that the energy generation profile of the PV cells matches the energy consumption profile of the BS. The system model of this chapter is presented in Section 2.3 and consists of an energy generation model, a ground-reflected irradiance model, a direct-beam irradiance model, a sky-diffuse irradiance model, an energy consumption model, and an objective function. Section 2.4 evaluates analytically to what extent the orientation angle θ determines the position of the peak of the energy generation profile in the time domain. The numerical results and the key findings are presented in Section 2.5. Finally, the chapter is summarized in Section 2.6.

Chapter 3 extends the system model from Chapter 2 by adding a battery to the BS. The battery is modeled by a Markov chain. Section 3.3 presents the system model of this chapter. Section 3.4 derives the PV cell's orientation angle optimiza-

tion algorithm with Markov chain based battery model of a solar-powered BS with battery. Section 3.5 introduces a simulation algorithm as a baseline for the comparison and evaluation of the proposed algorithm. Section 3.6 discusses and presents numerical results. In more detail, Section 3.6.1 investigates the running time of both algorithms. Section 3.6.2 verifies the accuracy of the proposed algorithm with simulation results. Section 3.6.3 shows the strong dependency of the optimal PV cell orientation angle on the battery capacity. Finally, the chapter is summarized in Section 3.7.

Chapter 4 extends the previous system model to a multi-cell cellular network. There are now several BSs distributed in an area and some of them are connected by distribution lines to share the renewable energy among them. The problem investigated in this chapter is how energy harvesters with anti-correlated energy generation profiles should be deployed to every BS so that the renewable energy can be shared most efficiently in the multi-cell cellular network. Two PV cells that have significantly different orientation angles, such as east-oriented and west-oriented PV cells, are an example for energy harvesters with anti-correlated energy generation profiles. Section 4.5 presents the system model of this chapter, which consists of the definition of the power surplus/deficit values, the derivation of the distance-dependent power loss in the distribution lines, and the definition of the topology of the cellular network. The objective function of this chapter is derived in Section 4.6 and based on a mixed-integer linear programming problem (MILPP). Section 4.7 presents the system performance improvements achieved by optimizing the deployment of the energy-harvesters with the MILPP in comparison with randomly deploying the energy harvesters. Finally, the chapter is summarized in Section 4.8.

Chapter 5 concludes the thesis by summarizing its achievements, highlighting future application areas, and outlining future work in this area. An appendix and a list of references are attached at the end of this thesis.

Chapter 2

PV Cell Orientation Angles

Optimization for a Base Station

Equipped with Several PV Cells

2.1 Literature Review: Orientation Angle Optimization

Many papers in the literature map for a given PV cell its performance in a wide geographical area. The average yearly or daily energy output of the PV cell is used as the performance metric. For each geographical location in the investigated area, the latitude, the longitude, the altitude, the ambient temperature, the wind speed, the solar spectrum, and site-specific weather conditions are often used to determine the performance of the PV cell. Nonetheless, these papers do not optimize any of the parameters of the PV cell, such as the orientation angle, instead they derive a guideline for the best deployment area for the given PV cell type. For example, [27], [28] and [29] derive comprehensive guides for PV cell deployment areas in South Africa, Europe, and Eurasia, respectively. In addition, geographic information

systems (GISs) provide such guides for various geographical areas online, such as for the USA [30], for Europe [10], and worldwide [31, 32].

Most papers investigating differently oriented PV cells, such as [33], have not actually optimized the PV cell angles but considered some deployment constraints, e.g., that the PV cells are mounted on residential rooftops, which predefine the PV cell angles.

Other papers, such as [34], optimize the orientation of objects to increase or decrease the sun irradiance on the object. These objects do not have to be PV cells. For example, [34] determines the optimal orientation of a building (no PV cells are deployed) so that less sun irradiance can enter the building through the windows. In climates with abundant sun irradiance, orientating the buildings so that less irradiance can enter the buildings through the windows reduces the need for cooling the buildings with air conditioning.

PV cell angle optimization for maximizing the total energy output of the PV cells has been done for Singapore in [35], however, without considering the potential mismatch between the energy generation profile of the PV cells and the energy consumption profile of the appliance. This may result in service outage if the PV cells are the only energy source or additional expenditures if the energy deficit has to be compensated by using alternative energy sources. Different from [35], the optimal PV cell orientation angles are derived in this thesis to match a given energy consumption profile rather than maximizing the total energy output of the PV cells.

In [36], the PV cell angle optimization considered the energy demand of the Ontario province of Canada, where the authors investigated orientation angles from 15° east of due south to 15° west of due south, i.e., $\theta \in [-15^\circ, 15^\circ]$. But propagation losses along the power lines among the widely-distributed PV cell installations were not included, which are significant factors when operating on a provincial scale [1, 4]. Different from [36], the optimal PV cell orientation angles are derived in the range from east ($\theta = -90^\circ$) to west ($\theta = 90^\circ$) in this thesis.

The authors of [37] investigated five orientation angle settings (east, southeast, south, southwest, and west) and concluded that in some scenarios a mix of east-oriented and west-oriented PV cells and in other scenarios south-oriented PV cells reduce the needs for storage and backup from dispatchable energy sources in a fully renewable European power system. Because they adjusted the installed capacity of the PV cells for each angle configuration, such that the average power production of each PV cell remains the same, it is difficult to fairly judge if the reduced needs for storage and backup are a good trade-off for the increased installed capacity of PV cells. Different from [37], the installed capacity of the PV cells is kept unchanged in this thesis. Hence, it is possible to fairly present the improvements caused by different PV cell orientation angles in this thesis.

Optimizing the PV cell inclination angle to power an isolated island was studied in [38], where the PV cell inclination angle was optimized on a yearly timescale. Because the PV cell inclination angle was optimized, the energy can be shifted on a yearly timescale, i.e., from a surplus season (e.g. summer) to a deficit season (e.g. winter), but the energy cannot be shifted on a daily timescale, i.e., from a surplus time (e.g. noon) to a deficit time (e.g. morning or afternoon) with the proposed method in [38].

In my papers [2, 5, 6], I have been optimizing the PV cell orientation angle of one PV cell deployed at the BS to match the energy generation of this single PV cell with the energy consumption of a BS. Optimizing the PV cell orientation angle of several PV cells deployed at the BS to match the energy generation of the PV cells with the energy consumption of a BS has been studied in my paper [7]. Hence, my paper [7] is an extension to my previous papers [2, 5, 6]. Chapter 2 of this thesis is based on [7]. In contrast to [2, 5, 6], [7] can investigate how the number of PV cells and the composition of differently oriented PV cells improve the match between the energy generation profile of the PV cells and the energy consumption profile of the BS.

2.2 Contributions of Chapter 2

The contributions of Chapter 2 are summarized as follows:

- Developing an algorithm to jointly optimize the orientation angles of several PV cells powering one BS. The algorithm achieves the best possible match between the energy generation profiles of the PV cells and the energy consumption profile of the BS. The proposed optimization algorithm only needs to be run a single time offline and the obtained optimal angles can be used for all solar-powered BSs with similar geographic locations and energy consumption profiles.
- Deriving analytically the irradiance values on any randomly inclined and oriented PV cell. A horizontally-mounted PV cell is used as a baseline and its irradiance values have to be given to derive the irradiance values on any randomly inclined and oriented PV cell at the same location.
- Identifying and discussing analytically to what extent the orientation angle θ shifts the energy generation profile away from noon if the PV cells are not south-oriented ($\theta \neq 0^\circ$).
- Evaluating the effectiveness of the proposed orientation angle optimization on three different types of BS energy consumption profiles: constant traffic load profiles, business-area traffic load profiles, and residential-area traffic load profiles. The energy drawn from the main grid by the BS per day is used as the performance metric.
- Giving recommendations on how many differently oriented PV cells should be deployed for a given energy consumption profile. To the best of my knowledge, this has never been investigated in the literature before.

2.3 System Model 1 - Several PV Cells Powering One BS

Figure 2.1 depicts the system model 1 considered in Chapter 2. The energy generation part consists of N identical PV cells, denoted by PV cell 1, PV cell 2, ..., and PV cell N , $N \in \mathbb{N}$. The energy consumption part consists of a BS. The total surface area of all N PV cells is A . Each PV cell has a surface area of $\frac{A}{N}$. The day is divided into T time steps, $T \in \mathbb{N}$. The index of a time step is denoted by t , $t \in \{1, \dots, T\}$. The BS uses the energy generated by the N PV cells, denoted by $G(t)$, to support its energy consumption $C(t)$ at every time step t . If there is an energy deficit, i.e., $C(t) - G(t) > 0$, the BS draws the remaining energy from the main grid at time step t . If there is an energy surplus, i.e., $C(t) - G(t) < 0$, the surplus energy is wasted at time step t or fed to the grid¹

The optimization object in the system model 1 is to minimize the amount of energy that has to be drawn from the main grid by the BS on a daily time scale. The energy drawn from the main grid can only be altered by choosing different orientation angles θ_1 , ..., and θ_N for PV cell 1, ..., and PV cell N , respectively. All the other parameters of the system, including the inclination angles of all N PV cells, are fixed. In this thesis, the system is located in Greenwich (London, UK) as example, i.e., the Latitude lat , and the Longitude lon are fixed to 51.4767° North, and 0.0003° West, respectively, but the analysis can be applied to other locations as well. Hence,

¹There are no feed-in tariffs considered in this thesis because I want to incentivize that the generated energy is used locally. Large amounts of intermittent generated energy which is fed into the grid often causes unbalancing issues, and voltage drops in the grid or in the worst-case scenario a black out. Matching the energy generation profile with the energy consumption profile on-site at a BS reduces therefore the stress on the power grid. This assumption is justified because most power grids nowadays are still designed for one-directional energy flow from a few large-scale centralized energy generators, such as coal power plants or nuclear power plants, to many small-scale energy consumers, such as domestic households or BSs. Current power grid infrastructure is often not assigned to accommodate huge amounts of energy flow in opposite direction and to redistribute such intermittent generated energy sufficiently without causing grid instability or jeopardizing the reliability of the power grid. Even if surplus energy can be sold to the grid, the system model 1 aims to match the energy generation profile with the energy consumption profile on-site at a BS, which is more cost-effective for the BS/ PV cells owner than wasting the surplus energy or selling the surplus energy to the grid for redistribution. Grid operators always sell energy at a higher price than they buy it.

all formulas in this thesis are given for a location in the northern hemisphere.

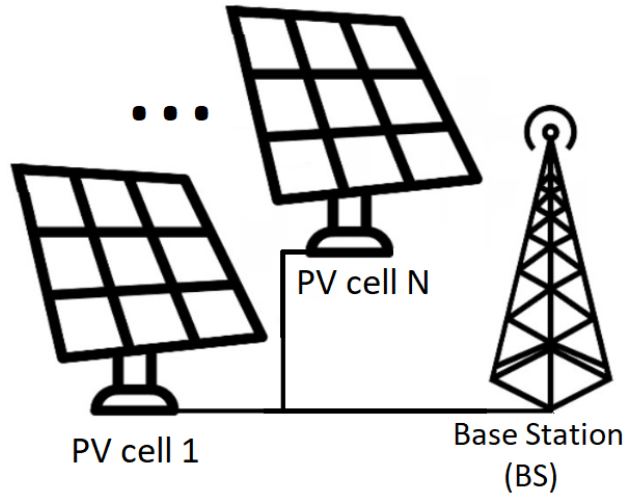


Figure 2.1: Illustration of system model 1

2.3.1 Energy Generation of a PV Cell

A horizontally-mounted PV cell in Greenwich (London, UK) is used as the baseline. From this baseline, a method will be developed to calculate the energy generated by a PV cell at the same location but installed with any orientation angle $\theta \in [-90^\circ, 90^\circ]$ and any inclination angle $\gamma \in [0, 90^\circ]$. The time is modeled in discrete time steps denoted by the time step index t , $t \in \{1, \dots, T\}$, hence all variables dependent on t are discrete. The global horizontal irradiance GHI_t , the diffuse horizontal irradiance DHI_t , and the direct normal irradiance DNI_t for a horizontally-mounted PV cell in Greenwich (London, UK) are obtained from the PVGIS database (cf. Figure 2.2) for every time step t . Hence, GHI_t , DHI_t , and DNI_t , are considered given values for every time step t and can be used throughout the thesis.

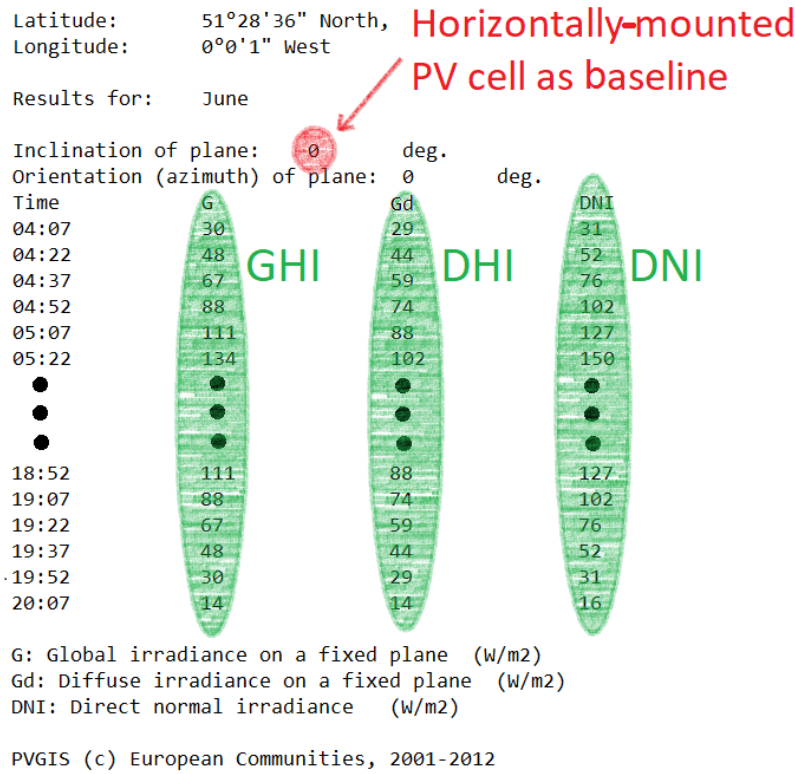


Figure 2.2: PVGIS data sheet from [10]

The energy generated by one PV cell installed with orientation angle θ and surface area $\frac{A}{N}$ is denoted by $G_{\theta,N}^{\text{original}}(t)$ and can be calculated by [39]² as follows:

$$G_{\theta,N}^{\text{original}}(t) = I_{\theta}(t) \cdot \eta \cdot \frac{A}{N} \cdot \tau, \quad (2.1)$$

where $I_{\theta}(t)$ is the irradiance received by the PV cell, η is the energy conversion efficiency, $\frac{A}{N}$ is the surface area of the PV cell, and τ is the duration of one time step.

To facilitate a fair comparison in Section 2.5, all energy generation values are normalized with respect to a south-orientated PV cell in Greenwich at noon with sur-

²The total irradiance received by the PV cell $I_{\theta}(t)$ adjusted for angle of incidence losses inside of the PV cell module, for soiling, e.g., dust or snow, for temporal losses, and for spectral mismatch is called the effective irradiance (irradiance that is “available” to the PV cell for power conversion). The material covering a cell in a PV module, e.g., glass, and encapsulate, causes due to reflection and absorption different losses at different angles of incidence. It is out of the scope of this thesis to calculate any internal energy losses of the PV cell due to its structure or composition. Therefore, it is assumed for simplicity that the total irradiance received by the PV cell $I_{\theta}(t)$ is the effective irradiance available by the PV cell for conversion in this thesis.

face area A , and inclination angle $\gamma = 36^\circ$ (optimal inclination angle for Greenwich (London, UK) in summer). Among all orientation angle settings and among all time steps throughout the day, the peak energy generation occurs during noon when all available PV cells are south-oriented in Greenwich. This is because Greenwich is located on the reference meridian of its time zone. The time step $t = \frac{T}{2}$ is noon. Because a south-oriented PV cell in Greenwich has its peak energy generation at noon, i.e., $I_{0^\circ}(\frac{T}{2}) \geq I_{0^\circ}(t) \quad \forall t \in \{1, \dots, T\}$, the peak irradiance value at noon, i.e., $614[\frac{W}{m^2}] = I_{0^\circ}(\frac{T}{2})$, is used as normalization factor in this thesis. The peak irradiance value is derived from [10] by downloading the data sheet for a south-oriented PV cell in Greenwich with inclination angle $\gamma = 36^\circ$. The normalization factor 614 has the effect that exactly 1 unit of normalized energy is generated by the south-oriented PV cell at noon after normalization. This normalization is done for convenience. Any normalization factor can be used but normalization the peak energy generation to 1 unit of energy is convenient when representing the results in graphs. Other locations than Greenwich (London, UK) will have to use their respective normalization factor and their respective optimal inclination angle. Appendix A will do the normalization process step by step for a better understanding.

Hence, $G_{\theta,N}(t)$ is the normalized energy generated by one PV cell out of the N PV cells installed with orientation angle θ and can be calculated by

$$G_{\theta,N}(t) = \frac{G_{\theta,N}^{\text{original}}(t)}{G_{0^\circ,1}^{\text{original}}(\frac{T}{2})} = \frac{I_\theta(t)}{I_{0^\circ}(\frac{T}{2}) \cdot N} = \frac{I_\theta(t)}{614 \cdot N}. \quad (2.2)$$

The normalized energy generated by N PV cells, denoted by $G_{(\theta_1, \dots, \theta_N)}(t)$, is calculated as follows:

$$G_{(\theta_1, \dots, \theta_N)}(t) = \sum_{i=1}^N G_{\theta_i, N}(t). \quad (2.3)$$

As a result, if all N PV cells are oriented to the south, they generate exactly 1 unit of energy at noon, i.e., $G_{(\theta_1, \dots, \theta_N)}(\frac{T}{2}) = G_{(0^\circ, \dots, 0^\circ)}(\frac{T}{2}) = 1$.

The irradiance $I_\theta(t)$ received by one PV cell installed with orientation angle θ at time step t can be calculated by [40] as follows:

$$I_\theta(t) = I_{b_\theta}(t) + I_{d_\theta}(t) + I_g(t), \quad (2.4)$$

where $I_{b_\theta}(t)$ is the direct-beam component, $I_{d_\theta}(t)$ is the sky-diffuse component, and $I_g(t)$ is the ground-reflected component. Figure 2.3 shows the three components graphically. The three irradiance components are investigated in the next three sections separately.

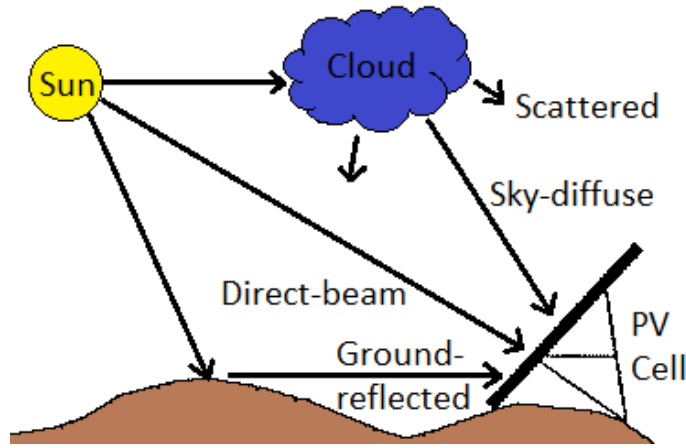


Figure 2.3: Irradiance model

2.3.2 Ground-reflected Irradiance $I_g(t)$

The ground-reflected irradiance $I_g(t)$ is independent of the orientation angle θ and can be calculated by [41] as follows:

$$I_g(t) = GHI_t \cdot \alpha \cdot \frac{1 - \cos(\gamma)}{2}, \quad (2.5)$$

where $\alpha \in [0, 1]$ is the albedo of the ground. The albedo is dimensionless and measures the amount of sunlight that a surface reflects. A black body that absorbs all sunlight has an albedo value of 0. A body that reflects all sunlight has an albedo

value of 1. For example, snow has a high albedo and hence, appears bright. Trees have a low albedo and hence, appear dark.

2.3.3 Direct-beam Irradiance $I_{b_\theta}(t)$

The direct-beam irradiance $I_{b_\theta}(t)$ depends on the orientation angle θ and can be calculated by [40] as follows:

$$I_{b_\theta}(t) = DNI_t \cdot \max(0, \cos(AOI_\theta(t))), \quad (2.6)$$

where $AOI_\theta(t)$ is the angle of incidence at time step t .

It is important to include the max in (2.6) to model that no energy can be harvest if the PV cell is illuminated from the back, i.e., $AOI_\theta(t) > 90^\circ$. For example, if the PV cell is oriented to the east then $AOI_\theta(t)$ will be greater than 90° in the evening. Hence, $\cos(AOI_\theta(t))$ will be smaller than 0. This will result in a negative irradiance value $I_{b_\theta}(t)$ during the evening, which makes no sense. As a result, the max in (2.6) is necessary.

The angle of incidence $AOI_\theta(t)$ is the angle between the line that points to the sun and the normal vector to the PV cell panel (cf. Figure 2.4). $AOI_\theta(t)$ can be calculated by [11] as follows:

$$\begin{aligned} \cos(AOI_\theta(t)) &= +\sin(\delta_d) \sin(lat) \cos(\gamma) \\ &\quad + \cos(\delta_d) \cos(lat) \cos(\gamma) \cos(\omega_t) \\ &\quad + \cos(\delta_d) \sin(\gamma) \sin(\omega_t) \sin(\theta) \\ &\quad - \sin(\delta_d) \cos(lat) \sin(\gamma) \cos(\theta) \\ &\quad + \cos(\delta_d) \sin(lat) \sin(\gamma) \cos(\omega_t) \cos(\theta) \\ &= a_t + b_t \sin(\theta) + c_t \cos(\theta), \text{ with} \end{aligned} \quad (2.7)$$

$$a_t = + \sin(\delta_d) \sin(lat) \cos(\gamma) + \cos(\delta_d) \cos(lat) \cos(\gamma) \cos(\omega_t), \quad (2.8)$$

$$b_t = + \cos(\delta_d) \sin(\gamma) \sin(\omega_t), \quad (2.9)$$

$$c_t = - \sin(\delta_d) \cos(lat) \sin(\gamma) + \cos(\delta_d) \sin(lat) \sin(\gamma) \cos(\omega_t), \quad (2.10)$$

where lat is the latitude of the deployment area, δ_d is the declination angle, and ω_t is the hour angle at time step t . a_t , b_t , and c_t include the parts that are independent of θ , are multiplied by $\sin(\theta)$, and are multiplied by $\cos(\theta)$, respectively.

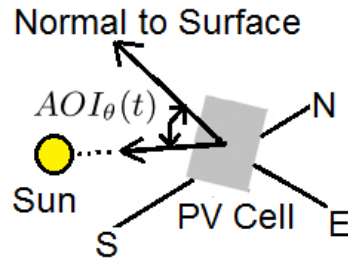


Figure 2.4: Definition of the angle of incidence $AOI_\theta(t)$

The declination angle δ_d can be calculated by [42] as follows:

$$\delta_d = 23.45^\circ \cdot \sin\left(\frac{360}{365}(d + 284)\right), \quad (2.11)$$

where d is the day of the year with 1st of January as $d = 1$.

The declination angle models the different seasons (cf. Figure 2.5). 23.45° is the axial tilt of the earth.

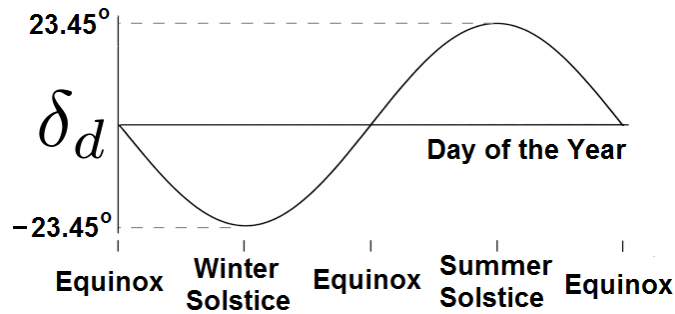


Figure 2.5: Declination angle δ_d throughout the year

The hour angle ω_t is defined as the angle between the meridian that intersects with the line that points to the sun and the meridian containing the observer (cf. Figure 2.6). The hour angle ω_t is depicted for Greenwich (London, UK) in Figure 2.7. Because Greenwich (London, UK) is located on the reference meridian of its time zone, the straight line in Figure 2.7 intersects the x-axis at noon³. ω_t has a period of 24 hours and ranges from -180° to 180° .

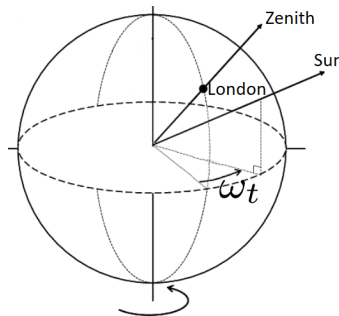


Figure 2.6: Definition of the hour angle ω_t

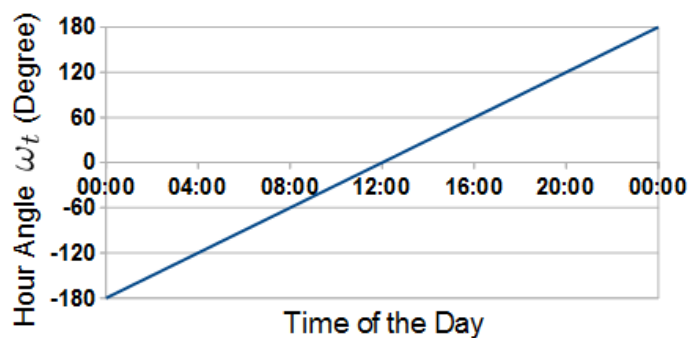


Figure 2.7: Hour angle ω_t throughout the day of a PV cell located on the reference meridian of its time zone

³The hour angles ω_t of locations that are not on their reference meridian of their time zone can be depicted by a straight line as well which is shifted along the x-axis. The formula to calculate the x-axis shift is given in [43].

2.3.4 Sky-diffuse Irradiance $I_{d_\theta}(t)$

The sky-diffuse irradiance $I_{d_\theta}(t)$ is derived from the Reindl model⁴ [48,49] as follows:

$$\begin{aligned}
 I_{d_\theta}(t) &= \underbrace{DHI_t \cdot A_t \cdot \frac{\max(0, \cos(AOI_\theta(t)))}{\cos(\zeta_t)}}_{\text{Circumsolar Component}} + \underbrace{DHI_t \cdot (1 - A_t) \cdot \frac{1 + \cos(\gamma)}{2}}_{\text{Isotropic Component}} + \\
 &\quad \underbrace{DHI_t \cdot (1 - A_t) \cdot \frac{1 + \cos(\gamma)}{2} \cdot \sqrt{\frac{DNI_t \cdot \cos(\zeta_t)}{GHI_t}} \sin^3\left(\frac{\gamma}{2}\right)}_{\text{Horizon Brightening Component}} = \\
 &DHI_t \left[A_t \cdot \frac{\max(0, \cos(AOI_\theta(t)))}{\cos(\zeta_t)} + (1 - A_t) \cdot \frac{1 + \cos(\gamma)}{2} \cdot \left(1 + \sqrt{\frac{DNI_t \cdot \cos(\zeta_t)}{GHI_t}} \sin^3\left(\frac{\gamma}{2}\right) \right) \right],
 \end{aligned} \tag{2.12}$$

where A_t is the anisotropy index, and ζ_t is the solar zenith angle. The Reindl model breaks the diffuse-sky irradiance into three separate parts: the isotropic component, the circumsolar component, and the horizon brightening component (cf. (2.12)). The circumsolar component depends on the orientation angle θ . The isotropic component, and the horizon brightening component do not depend on the orientation angle θ .

The solar zenith angle ζ_t can be calculated by [50] as follows:

$$\cos(\zeta_t) = \sin(lat) \sin(\delta_d) + \cos(lat) \cos(\delta_d) \cos(\omega_t). \tag{2.13}$$

The anisotropy index A_t of time step t can be calculated by [48] as follows:

⁴The difference between different irradiance models are usually in the way they model the sky-diffuse irradiance [44–46]. The simplest and most commonly used model is the Liu and Jordan model, which assumes an isotropic diffuse sky [35]. In other words, the diffuse-sky irradiance is uniform across the sky and hence, the diffuse-sky irradiance is independent of the orientation angle θ . The more advanced Reindl model is used in this thesis [47], which breaks the diffuse-sky irradiance into three separate parts: the isotropic component, the circumsolar component, and the horizon brightening component. The first component is the same as the Liu and Jordan model, while the other components are small correction terms. The circumsolar component depends on the orientation angle θ .

$$A_t = \frac{DNI_t}{E_d}, \quad (2.14)$$

where E_d is the extraterrestrial radiation. It can be calculated by [51] as follows:

$$E_d = E_{\text{con}} \cdot \left(\frac{\bar{r}}{r_d}\right)^2 = E_{\text{con}} \cdot \left(1 + 0.033 \cdot \cos\left(\frac{360 \cdot d}{365}\right)\right), \quad (2.15)$$

where E_{con} is the solar constant set at $1367 \frac{\text{W}}{\text{m}^2}$ [11], \bar{r} is the mean sun-earth distance also called 1 astronomical unit (1 AU), r_d is the actual sun-earth distance, which depends on the day of the year, and d is the day of the year with 1st of January as $d = 1$.

2.3.5 Energy Consumption of a BS

$C^{\text{original}}(t)$ is the original energy consumption by the BS during time step t (τ is the duration of one time step) and $C(t)$ is the normalized energy consumption by the BS at time step t and can be calculated by

$$C(t) = \frac{C^{\text{original}}(t)}{G_{0^\circ,1}^{\text{original}}\left(\frac{T}{2}\right)}, \quad (2.16)$$

where $G_{0^\circ,1}^{\text{original}}\left(\frac{T}{2}\right)$ is the peak energy generation of the PV cells if they are all south-oriented at noon. A practical example is given in Appendix A to show step by step the process of normalization.

$C(t)$ consists of a load-dependent part and a load-independent part. Three different load scenarios are investigated: a BS deployed with constant traffic load $C_{\text{con}}(t)$, with business-area traffic load $C_{\text{bus}}(t)$, and with residential-area traffic load $C_{\text{res}}(t)$ (cf. Figure 2.8). Three different example energy consumption profiles are given to show the composition of $C(t)$ into a load-dependent part and a load-independent part as follows:

$$C(t) = \underbrace{C_{\text{con}}(t)}_{\text{load-dependent part}} + \underbrace{1}_{\text{load-independent part}} \quad (2.17)$$

$$C(t) = \underbrace{C_{\text{bus}}(t)}_{\text{load-dependent part}} + \underbrace{0.2}_{\text{load-independent part}} \quad (2.18)$$

$$C(t) = \underbrace{C_{\text{res}}(t)}_{\text{load-dependent part}} + \underbrace{0.7}_{\text{load-independent part}} \quad (2.19)$$

The load-dependent part of the energy consumption profile determines the shape of the energy consumption profile, i.e., whether there is one significant peak in the profile, or several significant peaks in the profile or a very flat profile without any peaks.

The exact values for $C_{\text{con}}(t)$, $C_{\text{bus}}(t)$, and $C_{\text{res}}(t)$ are given in Appendix B "Input File (Load Profiles)" for all time steps $t \in \{1, \dots, T\}$ as well as in Figure 2.8. It can be observed that the traffic load in a business area ($C_{\text{bus}}(t)$) is significantly higher during business hours than the rest of the day, while it drops a bit during lunch hours. Hence, there is one significant peak in the business area traffic load profile during afternoon hours. The traffic load in a residential area ($C_{\text{res}}(t)$) is anti-correlated to the traffic load in a business area because it is higher during times when people are usually not working with its peak during late evening. This profile has peaks in the morning as well as in the evening.

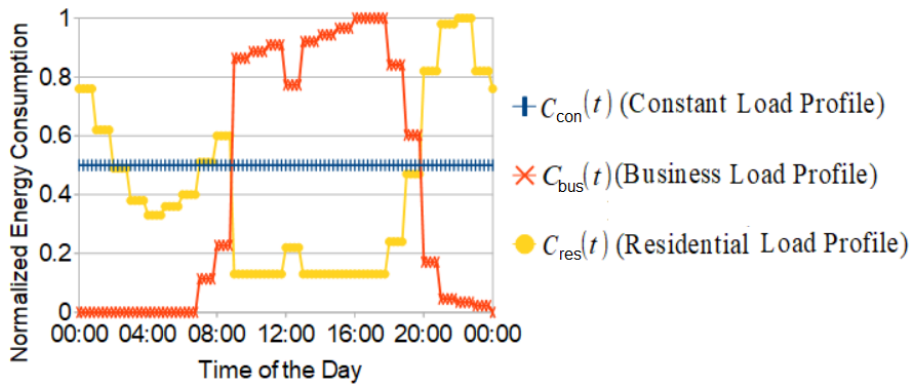


Figure 2.8: Constant traffic load profile, business traffic load profile, and residential traffic load profile throughout the day. Data source: [52]

For each of the three different load scenarios, I want to investigate how the relationship between the energy generation profile and the energy consumption profile affects the outcome of the orientation angles optimization. Therefore, I choose different values for the load-independent part of the energy consumption so that I have a case study in which the energy generation is significantly greater than the energy consumption ($G \gg C$), the energy generation is slightly greater than the energy consumption ($G > C$), the energy generation is slightly smaller than the energy consumption ($G < C$), and the energy generation is significantly smaller than the energy consumption ($G \ll C$). Figures 2.9 - 2.11 show all energy consumption profiles $C(t)$ which will be numerically investigated in section 2.5. The energy consumption profiles with the highest load-independent part in each figure belongs to the category $G \ll C$. The energy consumption profiles with the lowest load-independent part in each figure belongs to the category $G \gg C$.

To see the relationships between the energy consumption profiles $C(t)$ and the energy generation profiles $G(t)$, the combined energy generation profile of two south-oriented PV cells $G_{(0^\circ,0^\circ)}(t)$ as well as the combined energy generation profile of an east-oriented PV cell with a west-oriented PV cell $G_{(-90^\circ,90^\circ)}(t)$ are shown.

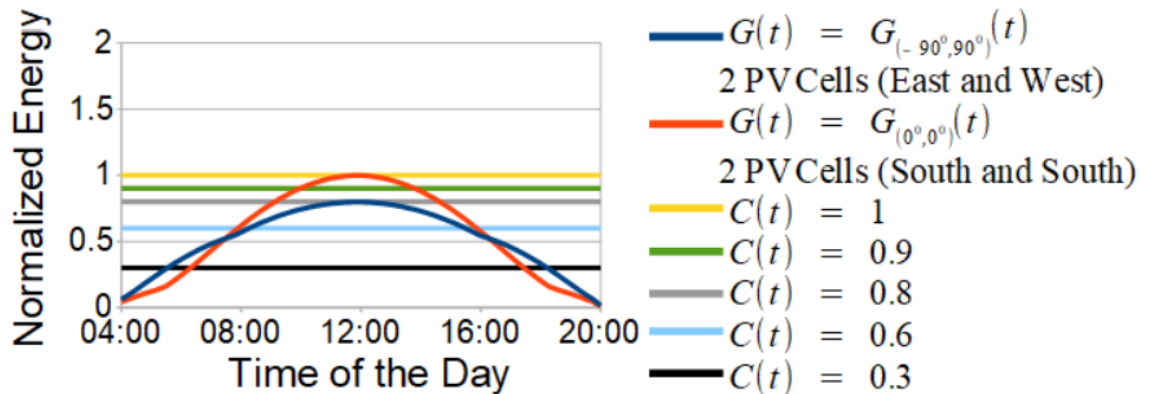


Figure 2.9: Energy consumption profiles with constant traffic load and energy generation profiles of 2 PV cells

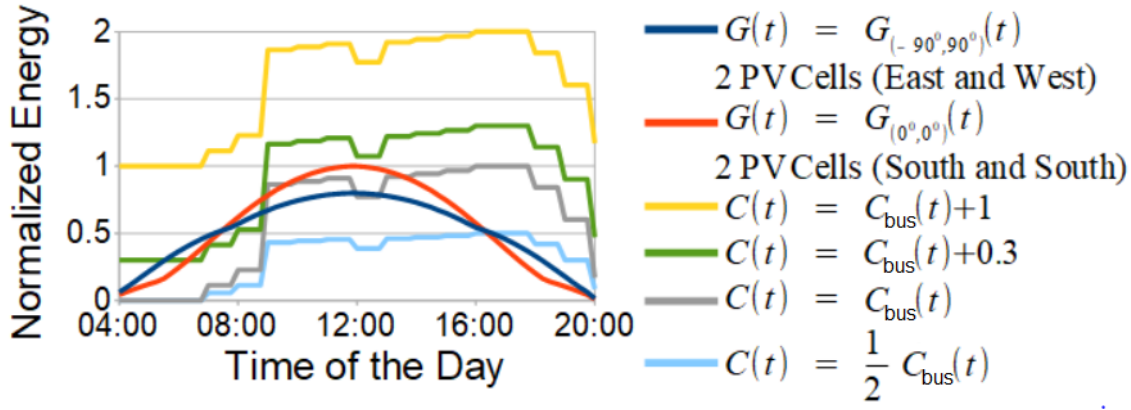


Figure 2.10: Energy consumption profiles with business-area traffic load and energy generation profiles of 2 PV cells

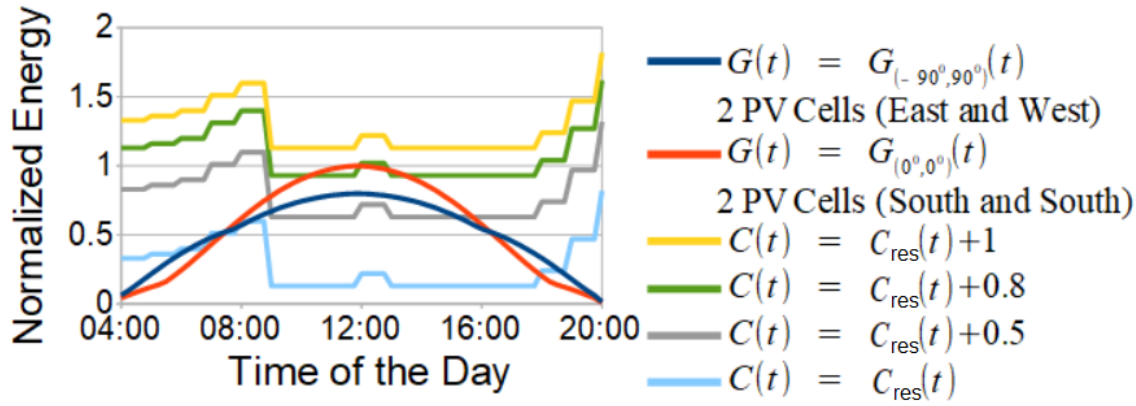


Figure 2.11: Energy consumption profiles with residential-area traffic load and energy generation profiles of 2 PV cells

2.3.6 Problem Formulation

The optimization objective is to minimize the normalized energy drawn from the main grid $f(\theta_1, \dots, \theta_N)$ by the BS throughout the day which is defined in (2.20). The optimization problem is formulated as follows:

$$f(\theta_1, \dots, \theta_N) = \sum_{t=1}^T \max\{0, C(t) - G_{(\theta_1, \dots, \theta_N)}(t)\} \quad (2.20)$$

$$(\theta_1^*, \dots, \theta_N^*) = \arg \min_{(\theta_1, \dots, \theta_N)} f(\theta_1, \dots, \theta_N), \quad (2.21)$$

where $(\theta_1^*, \dots, \theta_N^*)$ are the optimal orientation angles for the N PV cells.

Because surplus energy is wasted or fed to the grid with no feed-in tariff in the system model 1, the maximum out of 0 and $C(t) - G_{(\theta_1, \dots, \theta_N)}(t)$ has to be taken in (2.20). It is assumed that energy can be bought from the grid at a fixed price throughout the day (flat rates). Hence, the objective function is to minimize the accumulated energy deficit throughout the day in (2.20)-(2.21). $f(\theta_1, \dots, \theta_N)$ is transformed in (2.22) - (2.24). Eq. (2.24) is used in Appendix B.

$$f(\theta_1, \dots, \theta_N) = \sum_{t=1}^T \max \left\{ 0, C(t) - \sum_{n=1}^N G_{\theta_n, N}(t) \right\} \quad (2.22)$$

$$= \sum_{t=1}^T \max \left\{ 0, \underbrace{C(t) - \frac{I_g(t)}{614}}_{I_{\text{fix}}(t)} - \sum_{n=1}^N \frac{I_{b_{\theta_n}}(t) + I_{d_{\theta_n}}(t)}{614 \cdot N} \right\} \quad (2.23)$$

$$= \sum_{t=1}^T \max \left\{ 0, I_{\text{fix}}(t) - \sum_{n=1}^N \frac{I_{b_{\theta_n}}(t) + I_{d_{\theta_n}}(t)}{614 \cdot N} \right\} \quad (2.24)$$

The gain Δ_n of adding the n^{th} PV cell with optimal orientation angle θ_n^* to the system model 1 is defined as follows:

$$\Delta_n = f(\theta_1^*, \dots, \theta_{n-1}^*) - f(\theta_1^*, \dots, \theta_n^*), \quad n \in \{2, \dots, N\}. \quad (2.25)$$

The gain of adding the first PV cell with optimal orientation angle θ_1^* to the system model 1 is defined as follows:

$$\Delta_1 = f(0^\circ) - f(\theta_1^*). \quad (2.26)$$

A positive (negative) Δ_n value represents an improvement (deterioration) in performance of the system if the n^{th} PV cell is added, $n \in \{1, \dots, N\}$.

2.4 Analytical Insights obtained from Section 2.3

This section identifies and discusses analytically to what extent the orientation angle θ shifts the energy generation profile away from noon if the PV cells are not south-oriented ($\theta \neq 0^\circ$). The direct-beam irradiance $I_{b\theta}(t)$ and the sky-diffuse irradiance $I_{d\theta}(t)$ depend on θ . Nonetheless, because the main component of the sky-diffuse irradiance is independent of θ (isotropic component), while the other two components, which are dependent on θ , are small correction terms, the focus will be on the direct-beam irradiance in this section.

Figure 2.12 shows the values of a_t , b_t , and c_t throughout one day for the spring equinox ($d = 81$), summer solstice ($d = 172$), autumn equinox ($d = 264$), and winter solstice ($d = 355$). γ is fixed to 36° , and the location to Greenwich ($lat = 51.4767^\circ$ North, $lon = 0.0003^\circ$ West) to calculate the a_t , b_t , and c_t values. Only the hour angle ω_t changes throughout the day, whereas all other parameters are constant throughout the day in (2.8) - (2.10). Therefore, a_t , b_t , and c_t have a sine or cosine behavior with the y-axis shifts and amplitudes are summarized in (2.27) - (2.29). Because w_t has a period of 24 hours, a_t , b_t , and c_t have a period of 24 hours as well. The only angle that changes for different seasons is δ_d because it depends on the day of the year d . Therefore, the differences between the four a_t curves, the four b_t curves as well as the four c_t curves are caused only by δ_d . The curves for the spring equinox and autumn equinox are identical, i.e., $a_t(d = 81) = a_t(d = 264)$, $b_t(d = 81) = b_t(d = 264)$, and $c_t(d = 81) = c_t(d = 264)$.

$$a_t = \underbrace{+\sin(\delta_d)\sin(lat)\cos(\gamma)}_{\text{y-axis shift}} + \underbrace{\cos(\delta_d)\cos(lat)\cos(\gamma)}_{\text{amplitude}}\cos(\omega_t) \quad (2.27)$$

$$b_t = \underbrace{+\cos(\delta_d)\sin(\gamma)}_{\text{amplitude}}\sin(\omega_t) \quad (2.28)$$

$$c_t = \underbrace{-\sin(\delta_d)\cos(lat)\sin(\gamma)}_{\text{y-axis shift}} + \underbrace{\cos(\delta_d)\sin(lat)\sin(\gamma)}_{\text{amplitude}}\cos(\omega_t) \quad (2.29)$$

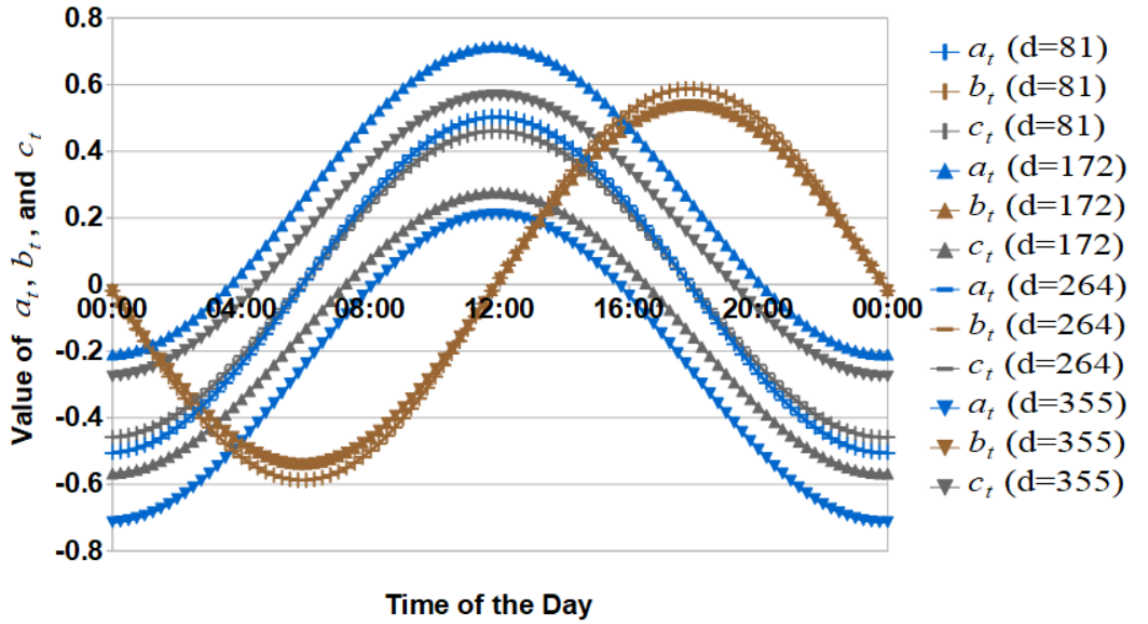


Figure 2.12: Values of a_t , b_t , and c_t throughout one day for the spring equinox ($d = 81$), summer solstice ($d = 172$), autumn equinox ($d = 264$), and winter solstice ($d = 355$). γ is set at 36° , and the location is Greenwich ($lat = 51.4767^\circ$ North, $lon = 0.0003^\circ$ West) for all scenarios.

The following insights are obtained from (2.27) to (2.29):

- a_t and c_t are symmetrical to noon. Hence, if $\theta \neq 0^\circ$, i.e., $\sin(\theta) \neq 0$, b_t is solely responsible for shifting the energy generation peak towards the morning or afternoon hours. If θ is orientated eastwards (westwards), then $\theta < 0^\circ$

($\theta > 0^\circ$), and $\sin(\theta) < 0$ ($\sin(\theta) > 0$), and hence the energy generation peak is shifted toward the morning (afternoon) hours.

- Also (2.6) causes an asymmetric energy generation profile if $\theta \neq 0^\circ$. The max in (2.6) removes the direct-beam irradiance if the PV cell is illuminated from the back. The more the PV cell is orientated eastwards (westwards), the longer the PV cell is illuminated from the back in the evening (morning) and the more energy is lost in the evening (morning).
- If the location of the PV cell is on the equator, the PV cell should be installed with the default inclination angle $\gamma = 0^\circ$ (cf. Table 1.1). As a consequence, $\sin(\gamma) = 0$, and $b_t = c_t = 0$. As a result, any orientation angle can be chosen for a PV cell on the equator because the orientation angle does not affect the energy generation profile of a PV cell on the equator. Figure 2.13 provides graphically the proof by using the data from PVGIS [10]. Hence, orientation angle optimization should be done for PV cells a bit farther away from the equator, where PV cells are not horizontally mounted. Alternatively, PV cells on the equator can be inclined ($\gamma \neq 0^\circ$) a bit to facilitate orientation angle optimization at the cost of reducing the average daily energy yield of the PV cells.

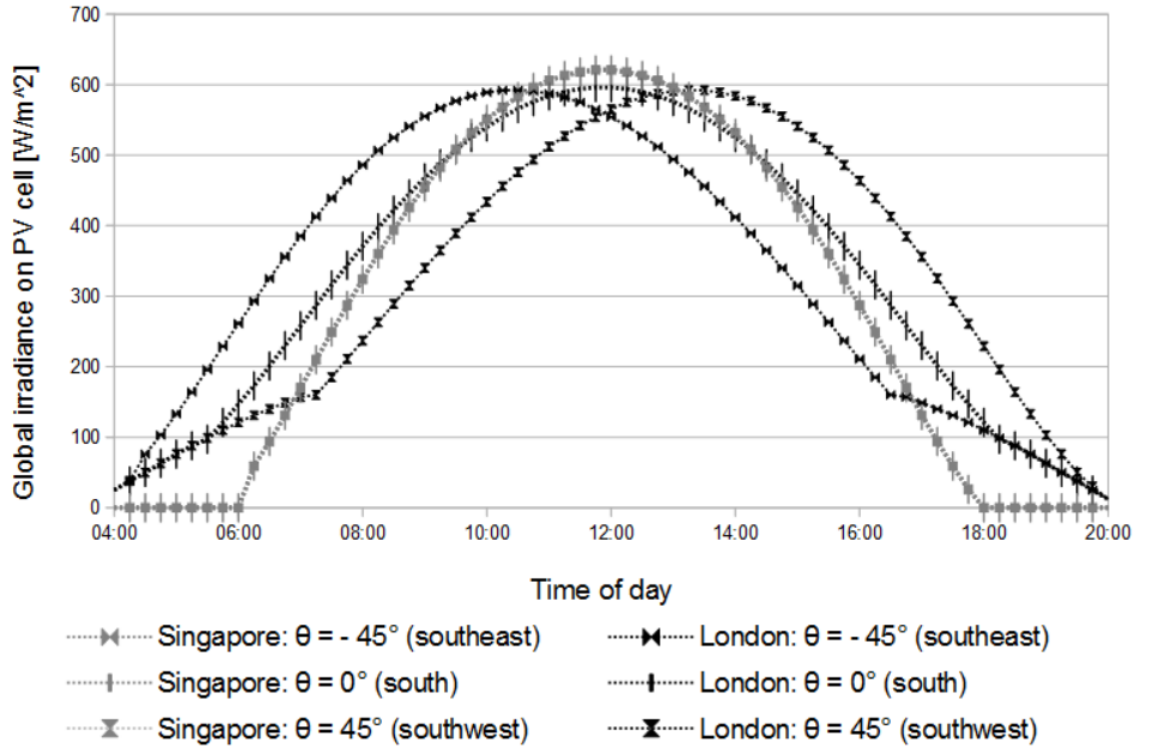


Figure 2.13: Irradiance values of differently orientated PV cell installations in Greenwich (temperate zone on northern hemisphere) and Singapore (close to equator) in June. An inclination angle of 38° (0°) was chosen for Greenwich (Singapore).

Data source: [10]

- The amplitude of b_t is equal to the amplitude of c_t at the north and south poles, whereas the amplitude of b_t is greater than the amplitude of c_t at any other location.

2.5 Results and Discussion

Table 2.1 summarizes all parameters and their values. The total surface area of the N PV cells, denoted by A , the duration of one time step, denoted by τ , and the energy conversion efficiency of the PV cells, denoted by η , do not appear in (2.2) anymore due to the normalization of the energy generation in (2.2). As a result, there is no value assigned to these parameters in Table 2.1.

The derived $I_\theta(t)$ values in this thesis were compared with the modeled irradiance values from the PVGIS database (daily data profiles [53]). Both values were the

same. This proves that our derivation and implementation of the irradiance model is correct. The irradiance model implemented in PVGIS [10] is the Muneer model [54], but it is mentioned on the PVGIS website [55] that the Muneer model performs very similar to the Reindl model. The Reindl model was used in this thesis.

Table 2.1:
Input parameters of system model 1

Parameter	Description	Value
α	Albedo of ground	0.2 (Grassland)
γ	Inclination angle	36°
δ_d	Declination angle	Eq. (2.11)
ζ_t	Zenith angle	Eq. (2.13)
η	Energy conversion efficiency of the PV cells	
θ	Orientation angle	$\in [-90^\circ, 90^\circ]$
$\theta_1, \dots, \theta_N$	Orientation angles of PV cells 1, ..., N	$\in [-90^\circ, 90^\circ]$
$\theta_1^*, \dots, \theta_N^*$	Optimal orientation angles $\theta_1, \dots, \theta_N$	$\in [-90^\circ, 90^\circ]$
τ	Duration of one time step	
ω_t	Hour angle	Figure 2.7
Δ_1	Gain of adding the 1 st PV cell	Eq. (2.26)
Δ_n	Gain of adding the n^{th} PV cell, $n \in \{2, \dots, N\}$	Eq. (2.25)
A	Total surface area of N PV cells	
A_t	Anisotropy index at time step t	Eq. (2.14)
$AOI_\theta(t)$	Angle of incidence	Eq. (2.7)
$C(t)$	Energy consumption of BS at time step t	Figures 2.9 - 2.11
$C_{\text{bus}}(t)$	Business-area traffic load profile at time step t	Figure 2.8
$C_{\text{con}}(t)$	Constant traffic load profile at time step t	Figure 2.8
$C_{\text{res}}(t)$	Residential-area traffic load profile at time step t	Figure 2.8
DHI_t	Diffuse horizontal irradiance at time step t	PVGIS [10]
DNI_t	Direct normal irradiance at time step t	PVGIS [10]
E_d	Extraterrestrial radiation	Eq. (2.15)

E_{con}	Solar constant	$1367 \frac{\text{W}}{\text{m}^2}$ [11]
$G(t)$	Energy generation of PV cell/cells at time step t	
$G_{\theta, N}^{\text{original}}(t)$	Energy generated by one PV cell installed with θ at time step t (N is the total number of PV cells)	Eq. (2.1)
$G_{\theta, N}(t)$	Normalized energy generated by one PV cell installed with θ at time step t (N is the total number of PV cells)	Eq. (2.2)
$G_{(\theta_1, \dots, \theta_N)}(t)$	Normalized total energy generated by N PV cells at time step t installed with $\theta_1, \dots, \theta_N$	Eq. (2.3)
GHI_t	Global horizontal irradiance at time step t	PVGIS [10]
$I_{\theta}(t)$	Irradiance on PV cell installed with θ at time step t	Eq. (2.4)
$I_{b_{\theta}}(t)$	Direct-beam irradiance at time step t	Eq. (2.6)
$I_{d_{\theta}}(t)$	Sky-diffuse irradiance at time step t	Eq. (2.12)
$I_g(t)$	Ground-reflected irradiance at time step t	Eq. (2.5)
N	Number of PV cells	$\in \{1, 2, 3\}$
T	Number of time steps	96
a_t	Independent of θ	Eq. (2.8)
b_t	Multiplied by $\sin(\theta)$	Eq. (2.9)
c_t	Multiplied by $\cos(\theta)$	Eq. (2.10)
d	Day of the year	165 (June)
$f(\theta_1, \dots, \theta_N)$	Optimization objective	Eq. (2.20)
lat	Latitude	51.4767° North (Greenwich)
lon	Longitude	0.0003° West (Greenwich)

2.5.1 Remarks on the Presentation of the Results

The optimal orientation angle(s) will be investigated for 1, 2, and 3 PV cell(s) in Subsections 2.5.1.1, 2.5.1.2, and 2.5.1.3, respectively. The optimal orientation angle will be obtained for each PV cell in the complete range from -90° to 90° with an angular resolution of 1° .

The graphs in the Table 2.2, Table 2.4, and Table 2.6 are generated with MATLAB. The source code of Chapter 2 is given in the Appendix B of this thesis and is available on GitHub [56].

Normalized energy generation and consumption profiles are used in this thesis. That means the given recommendations in this section can be scaled up for the intended application in the real world. For example, if the derived recommendation for the normalized consumption profile $C(t)$ is to deploy one PV cell with optimal orientation angle θ_1^* , that means to deploy several PV cells with the same orientation angle θ_1^* in the real world if $C(t)$ was the consumption profile of a large-scale BS. Another example, if the derived recommendation for the normalized consumption profile $C(t)$ is to deploy two PV cells with jointly optimized orientation angles θ_1^* and θ_2^* , that means to deploy several PV cells where half of them are deployed with θ_1^* and the other half with θ_2^* in the real world if $C(t)$ was the consumption profile of a large-scale BS.

2.5.1.1 Results for 1 PV Cell (N=1)

Table 2.2 and Table 2.3 show the results for 1 PV cell.

The orientation angle is optimized for three different types of load profiles: the constant load profile $C_{\text{con}}(t)$, the business load profile $C_{\text{bus}}(t)$, and the residential load profile $C_{\text{res}}(t)$ (cf. Figure 2.8). The left, middle, and right columns in Table 2.2 represent the constant, business, and residential load profiles, respectively. Each row in Table 2.2 represents the relative relationship between the energy generation

profile and energy consumption profile. In other words, the first, second, third, and fourth rows in Table 2.2 represent the scenario that the energy generation is significantly smaller, is slightly smaller, is slightly greater, is significantly greater than the energy consumption, denoted by $G \ll C$, $G < C$, $G > C$, and $G \gg C$, respectively. The red lines in Table 2.2 are the optimal orientation angles.

Table 2.2:
Orientation angles optimization for 1 PV cell with different load profiles

	Constant Load Profile	Business Load Profile	Residential Load Profile
$G \ll C$	<p>Table cell (a):</p> <p>Orientation Angle of PV Cell 1 (θ_1)</p> <p>Normalized Energy drawn from the Grid</p> <p>$C(t) = 1$ (Figure 2.9 yellow line)</p>	<p>Table cell (b):</p> <p>Orientation Angle of PV Cell 1 (θ_1)</p> <p>Normalized Energy drawn from the Grid</p> <p>$C(t) = C_{bus}(t) + 1$ (Figure 2.10 yellow line)</p>	<p>Table cell (c):</p> <p>Orientation Angle of PV Cell 1 (θ_1)</p> <p>Normalized Energy drawn from the Grid</p> <p>$C(t) = C_{res}(t) + 1$ (Figure 2.11 yellow line)</p>
$G < C$	<p>Table cell (d):</p> <p>Orientation Angle of PV Cell 1 (θ_1)</p> <p>Normalized Energy drawn from the Grid</p> <p>$C(t) = 0.8$ (Figure 2.9 gray line)</p>	<p>Table cell (e):</p> <p>Orientation Angle of PV Cell 1 (θ_1)</p> <p>Normalized Energy drawn from the Grid</p> <p>$C(t) = C_{bus}(t) + 0.3$ (Figure 2.10 green line)</p>	<p>Table cell (f):</p> <p>Orientation Angle of PV Cell 1 (θ_1)</p> <p>Normalized Energy drawn from the Grid</p> <p>$C(t) = C_{res}(t) + 0.8$ (Figure 2.11 green line)</p>
$G > C$	<p>Table cell (g):</p> <p>Orientation Angle of PV Cell 1 (θ_1)</p> <p>Normalized Energy drawn from the Grid</p> <p>$C(t) = 0.6$ (Figure 2.9 light blue line)</p>	<p>Table cell (h):</p> <p>Orientation Angle of PV Cell 1 (θ_1)</p> <p>Normalized Energy drawn from the Grid</p> <p>$C(t) = C_{bus}(t)$ (Figure 2.10 gray line)</p>	<p>Table cell (i):</p> <p>Orientation Angle of PV Cell 1 (θ_1)</p> <p>Normalized Energy drawn from the Grid</p> <p>$C(t) = C_{res}(t) + 0.5$ (Figure 2.11 gray line)</p>
$G \gg C$	<p>Table cell (j):</p> <p>Orientation Angle of PV Cell 1 (θ_1)</p> <p>Normalized Energy drawn from the Grid</p> <p>$C(t) = 0.3$ (Figure 2.9 black line)</p>	<p>Table cell (k):</p> <p>Orientation Angle of PV Cell 1 (θ_1)</p> <p>Normalized Energy drawn from the Grid</p> <p>$C(t) = \frac{1}{2}C_{bus}(t)$ (Figure 2.10 light blue line)</p>	<p>Table cell (l):</p> <p>Orientation Angle of PV Cell 1 (θ_1)</p> <p>Normalized Energy drawn from the Grid</p> <p>$C(t) = C_{res}(t)$ (Figure 2.11 light blue line)</p>

Table 2.3:
Summary of all optimal orientation angles for 1 PV cell with the different load profiles from Table 2.2

	Constant Load Profile	Business Load Profile	Residential Load Profile
$G < < C$	Table cell (a) of Table 2.2: 1 optimal line $\in \{0^\circ\}$	Table cell (b) of Table 2.2: 1 optimal line $\in \{0^\circ\}$	Table cell (c) of Table 2.2: 1 optimal line $\in \{0^\circ\}$
	θ_1^*		
	$f(0^\circ)$	60.0712	101.3440
	$f(\theta_1^*)$	60.0712	101.3440
	Δ_1	0	0
$G < C$	Table cell (d) of Table 2.2: 2 optimal lines $\in \{-12^\circ, 12^\circ\}$	Table cell (e) of Table 2.2: 1 optimal line $\in \{32^\circ\}$	Table cell (f) of Table 2.2: 1 optimal line $\in \{7^\circ\}$
	θ_1^*		
	$f(0^\circ)$	43.7613	35.2500
	$f(\theta_1^*)$	43.7530	34.3548
	Δ_1	0.0083	0.0168
$G > > C$	Table cell (g) of Table 2.2: 2 optimal lines $\in \{-35^\circ, 35^\circ\}$	Table cell (h) of Table 2.2: 1 optimal line $\in \{59^\circ\}$	Table cell (i) of Table 2.2: 1 optimal line $\in \{-70^\circ\}$
	θ_1^*		
	$f(0^\circ)$	29.9956	12.3939
	$f(\theta_1^*)$	29.9630	10.0621
	Δ_1	0.0326	1.2631
$G > C$	Table cell (j) of Table 2.2: 2 optimal lines $\in \{-90^\circ, 90^\circ\}$	Table cell (k) of Table 2.2: 1 optimal line $\in \{90^\circ\}$	Table cell (l) of Table 2.2: 1 optimal line $\in \{-90^\circ\}$
	θ_1^*		
	$f(0^\circ)$	12.6629	3.3316
	$f(\theta_1^*)$	12.2800	1.2400
	Δ_1	0.3829	2.0916

2.5.1.2 Results for 2 PV Cells (N=2)

Table 2.4 and Table 2.5 show the results for 2 PV cells.

The orientation angles are optimized for three different types of load profiles: the constant load profile $C_{\text{con}}(t)$, the business load profile $C_{\text{bus}}(t)$, and the residential load profile $C_{\text{res}}(t)$ (cf. Figure 2.8). The left, middle, and right columns in Table 2.4 represent the constant, business, and residential load profiles, respectively. Each row in Table 2.4 represents the relative relationship between the energy generation profile and energy consumption profile. In other words, the first, second, third, and fourth rows in Table 2.4 represent the scenario that the energy generation is significantly smaller, is slightly smaller, is slightly greater, is significantly greater than the energy consumption, denoted by $G \ll C$, $G < C$, $G > C$, and $G \gg C$, respectively. The red points in Table 2.4 are the optimal orientation angles. Each square in Table 2.4 has one line of symmetry $L := \{(\theta_1, \theta_2) \in [-90^\circ, 90^\circ]^2 \mid \theta_1 = \theta_2\}$.

Table 2.4:
Orientation angles optimization for 2 PV cells with different load profiles

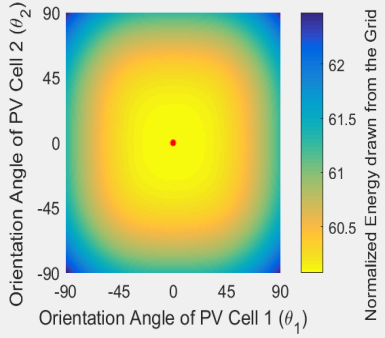
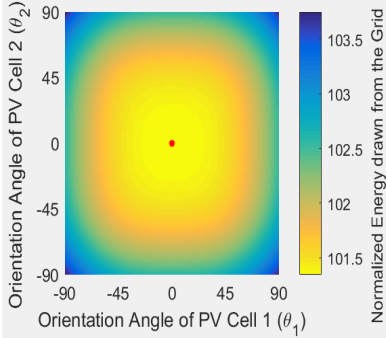
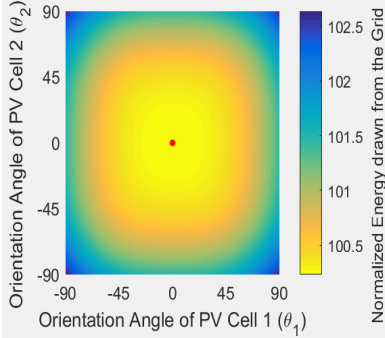
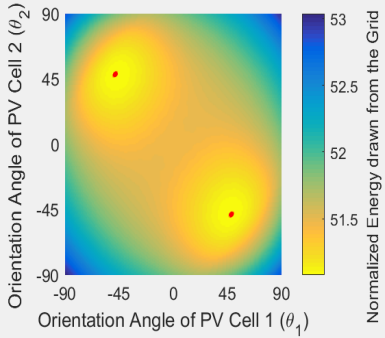
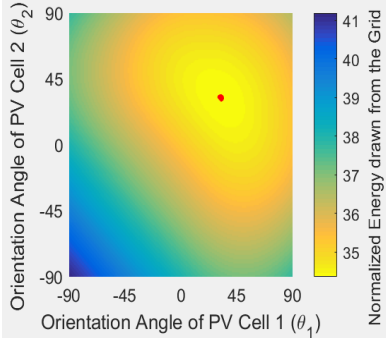
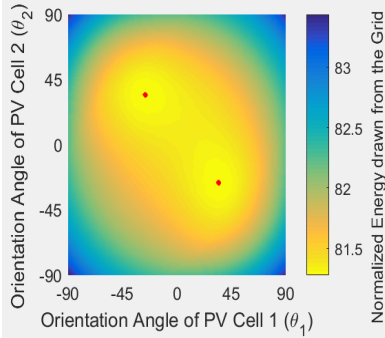
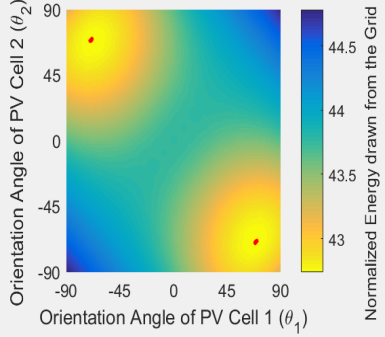
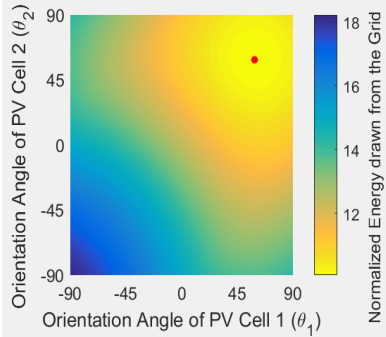
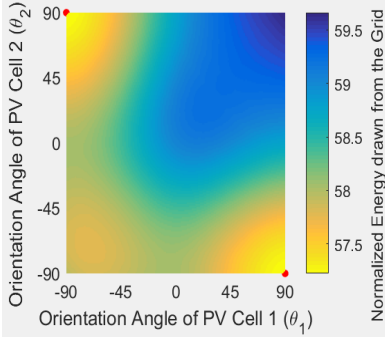
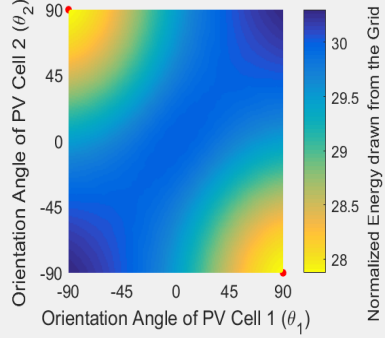
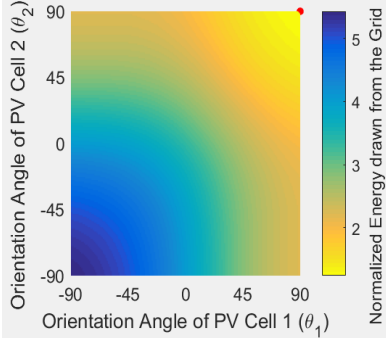
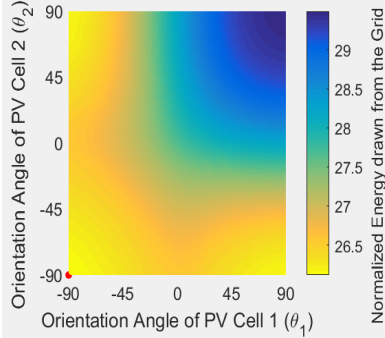
	Constant Load Profile	Business Load Profile	Residential Load Profile
$G \ll C$	<p>Table cell (a):</p>  <p>$C(t) = 1$ (Figure 2.9 yellow line)</p>	<p>Table cell (b):</p>  <p>$C(t) = C_{\text{bus}}(t) + 1$ (Figure 2.10 yellow line)</p>	<p>Table cell (c):</p>  <p>$C(t) = C_{\text{res}}(t) + 1$ (Figure 2.11 yellow line)</p>
	<p>Table cell (d):</p>  <p>$C(t) = 0.9$ (Figure 2.9 green line)</p>	<p>Table cell (e):</p>  <p>$C(t) = C_{\text{bus}}(t) + 0.3$ (Figure 2.10 green line)</p>	<p>Table cell (f):</p>  <p>$C(t) = C_{\text{res}}(t) + 0.8$ (Figure 2.11 green line)</p>
	<p>Table cell (g):</p>  <p>$C(t) = 0.8$ (Figure 2.9 gray line)</p>	<p>Table cell (h):</p>  <p>$C(t) = C_{\text{bus}}(t)$ (Figure 2.10 gray line)</p>	<p>Table cell (i):</p>  <p>$C(t) = C_{\text{res}}(t) + 0.5$ (Figure 2.11 gray line)</p>
	<p>Table cell (j):</p>  <p>$C(t) = 0.6$ (Figure 2.9 light blue line)</p>	<p>Table cell (k):</p>  <p>$C(t) = \frac{1}{2}C_{\text{bus}}(t)$ (Figure 2.10 light blue line)</p>	<p>Table cell (l):</p>  <p>$C(t) = C_{\text{res}}(t)$ (Figure 2.11 light blue line)</p>

Table 2.5:
Summary of all optimal orientation angles for 2 PV cells with the different load profiles from Table 2.4

	Constant Load Profile	Business Load Profile	Residential Load Profile
$G < < C$	(θ_1^*, θ_2^*)	Table cell (a) of Table 2.4: 1 optimal point $\in \{(0^\circ, 0^\circ)\}$	Table cell (b) of Table 2.4: 1 optimal point $\in \{(0^\circ, 0^\circ)\}$
	$f(\theta_1^*, \theta_2^*)$	60.0712	101.3440
	Δ_2	0	0
$G < C$	(θ_1^*, θ_2^*)	Table cell (d) of Table 2.4: 2 optimal points $\in \{(-48^\circ, 48^\circ), (48^\circ, -48^\circ)\}$	Table cell (e) of Table 2.4: 1 optimal point $\in \{(32^\circ, 32^\circ)\}$
	$f(\theta_1^*, \theta_2^*)$	51.0780	34.3548
	Δ_2	0.3918	0
$G > C$	(θ_1^*, θ_2^*)	Table cell (g) of Table 2.4: 2 optimal points $\in \{(-69^\circ, 69^\circ), (69^\circ, -69^\circ)\}$	Table cell (h) of Table 2.4: 1 optimal point $\in \{(59^\circ, 59^\circ)\}$
	$f(\theta_1^*, \theta_2^*)$	42.7376	10.0621
	Δ_2	1.0154	0
$G > > C$	(θ_1^*, θ_2^*)	Table cell (j) of Table 2.4: 2 optimal points $\in \{(-90^\circ, 90^\circ), (90^\circ, -90^\circ)\}$	Table cell (k) of Table 2.4: 1 optimal point $\in \{(90^\circ, 90^\circ)\}$
	$f(\theta_1^*, \theta_2^*)$	27.8739	1.2400
	Δ_2	2.0891	0
			Table cell (c) of Table 2.4: 1 optimal point $\in \{(0^\circ, 0^\circ)\}$
			100.2310
			0
			Table cell (f) of Table 2.4: 2 optimal points $\in \{(-26^\circ, 35^\circ), (35^\circ, -26^\circ)\}$
			81.2773
			0.0757
			Table cell (i) of Table 2.4: 2 optimal points $\in \{(-90^\circ, 90^\circ), (90^\circ, -90^\circ)\}$
			57.2246
			0.5424
			Table cell (l) of Table 2.4: 1 optimal point $\in \{(-90^\circ, -90^\circ)\}$
			26.1165
			0

2.5.1.3 Results for 3 PV Cells (N=3)

Table 2.6 and Table 2.7 show the results for 3 PV cells.

The orientation angles are optimized for three different types of load profiles: the constant load profile $C_{\text{con}}(t)$, the business load profile $C_{\text{bus}}(t)$, and the residential load profile $C_{\text{res}}(t)$ (cf. Figure 2.8). The left, middle, and right columns in Table 2.6 represent the constant, business, and residential load profiles, respectively. Each row in Table 2.6 represents the relative relationship between the energy generation profile and energy consumption profile. In other words, the first, second, third, and fourth rows in Table 2.6 represent the scenario that the energy generation is significantly smaller, is slightly smaller, is slightly greater, is significantly greater than the energy consumption, denoted by $G \ll C$, $G < C$, $G > C$, and $G \gg C$, respectively. The red points in each cube in Table 2.6 are the optimal orientation angles. Each cube in Table 2.6 has three planes of symmetry as follows:

$$P_1 := \{(\theta_1, \theta_2, \theta_3) \in [-90^\circ, 90^\circ]^3 \mid \theta_2 = \theta_3\}, \quad (2.30)$$

$$P_2 := \{(\theta_1, \theta_2, \theta_3) \in [-90^\circ, 90^\circ]^3 \mid \theta_1 = \theta_3\}, \text{ and} \quad (2.31)$$

$$P_3 := \{(\theta_1, \theta_2, \theta_3) \in [-90^\circ, 90^\circ]^3 \mid \theta_1 = \theta_2\}. \quad (2.32)$$

The y-axis (θ_2 -axis) is reversed in all business load profile scenarios (second column of Table 2.6) so that the optimal points (red points) are visible. Because it is not possible to show all values from a solid 3D cube on a 2D paper, every solid cube in Table 2.6 is visualized by 6 planes slicing through the cube. The six planes are

$$S_1 := \{(\theta_1, \theta_2, \theta_3) \in [-90^\circ, 90^\circ]^3 \mid \theta_3 = 90^\circ\}, \quad (2.33)$$

$$S_2 := \{(\theta_1, \theta_2, \theta_3) \in [-90^\circ, 90^\circ]^3 \mid \theta_3 = 45^\circ\}, \quad (2.34)$$

$$S_3 := \{(\theta_1, \theta_2, \theta_3) \in [-90^\circ, 90^\circ]^3 \mid \theta_3 = 0^\circ\}, \quad (2.35)$$

$$S_4 := \{(\theta_1, \theta_2, \theta_3) \in [-90^\circ, 90^\circ]^3 \mid \theta_3 = -45^\circ\}, \quad (2.36)$$

$$S_5 := \{(\theta_1, \theta_2, \theta_3) \in [-90^\circ, 90^\circ]^3 \mid \theta_3 = -90^\circ\}, \text{ and} \quad (2.37)$$

$$S_6 := \{(\theta_1, \theta_2, \theta_3) \in [-90^\circ, 90^\circ]^3 \mid \theta_2 = 0^\circ\}. \quad (2.38)$$

The optimal orientation angles (red points in Table 2.6) might float between the six slicing planes. Table 2.7 presents the exact values of the optimal orientation angles, hence the exact position of the red points in the cube.

Table 2.6:
Orientation angles optimization for 3 PV cells with different load profiles

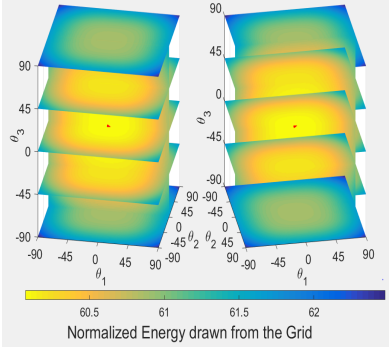
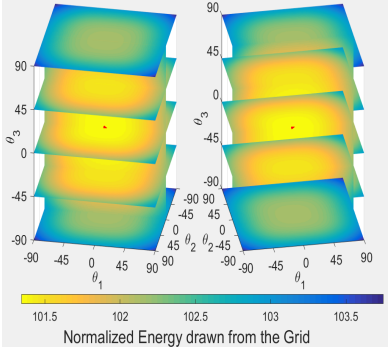
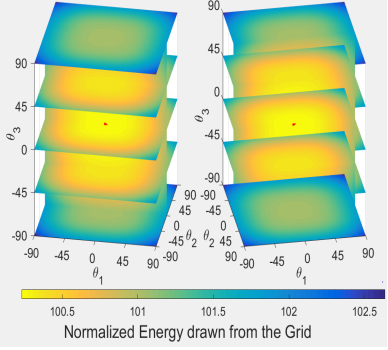
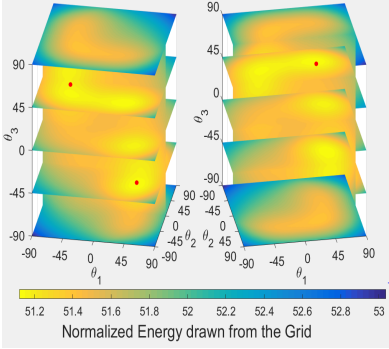
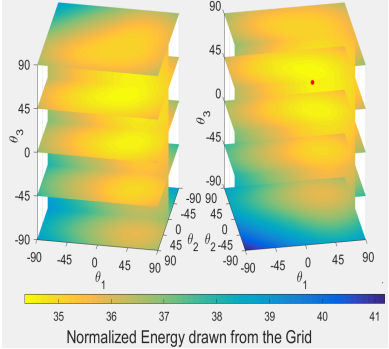
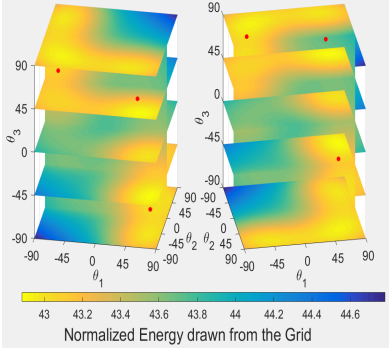
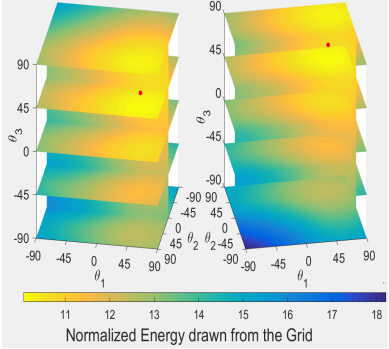
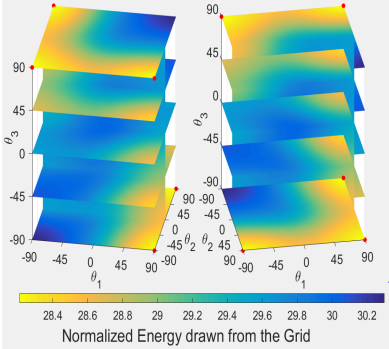
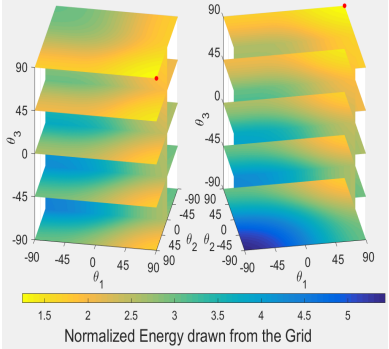
	Constant Load Profile	Business Load Profile	Residential Load Profile
$G \ll C$	Table cell (a):  $C(t) = 1$ (Figure 2.9 yellow line)	Table cell (b):  $C(t) = C_{bus}(t) + 1$ (Figure 2.10 yellow line)	Table cell (c):  $C(t) = C_{res}(t) + 1$ (Figure 2.11 yellow line)
	$G < C$	Table cell (d):  $C(t) = 0.9$ (Figure 2.9 green line)	Table cell (e):  $C(t) = C_{bus}(t) + 0.3$ (Figure 2.10 green line)
$G > C$		Table cell (g):  $C(t) = 0.8$ (Figure 2.9 gray line)	Table cell (h):  $C(t) = C_{bus}(t)$ (Figure 2.10 gray line)
	$G \gg C$	Table cell (j):  $C(t) = 0.6$ (Figure 2.9 light blue line)	Table cell (k):  $C(t) = \frac{1}{2}C_{bus}(t)$ (Figure 2.10 light blue line)

Table 2.7:
Summary of all optimal orientation angles for 3 PV cells with the different load profiles from Table 2.6

	Constant Load Profile	Business Load Profile	Residential Load Profile
$G << C$	$(\theta_1^*, \theta_2^*, \theta_3^*)$ 1 optimal point $\in \{(0^\circ, 0^\circ, 0^\circ)\}$	Table cell (a) of Table 2.6: 1 optimal point $\in \{(0^\circ, 0^\circ, 0^\circ)\}$	Table cell (b) of Table 2.6: 1 optimal point $\in \{(0^\circ, 0^\circ, 0^\circ)\}$
	$f(\theta_1^*, \theta_2^*, \theta_3^*)$ Δ_3	60.0712 0	101.3440 0
$G < C$	$(\theta_1^*, \theta_2^*, \theta_3^*)$ 6 optimal points $\in \{(-55^\circ, 42^\circ, 42^\circ), (-42^\circ, -42^\circ, 55^\circ), (-42^\circ, 55^\circ, -42^\circ), (42^\circ, -55^\circ, 42^\circ), (42^\circ, 42^\circ, -55^\circ), (55^\circ, -42^\circ, -42^\circ)\}$	Table cell (d) of Table 2.6: 6 optimal points $\in \{(-55^\circ, 42^\circ, 42^\circ), (-42^\circ, -42^\circ, 55^\circ), (-42^\circ, 55^\circ, -42^\circ), (42^\circ, -55^\circ, 42^\circ), (42^\circ, 42^\circ, -55^\circ), (55^\circ, -42^\circ, -42^\circ)\}$	Table cell (e) of Table 2.6: 1 optimal point $\in \{(32^\circ, 32^\circ, 32^\circ)\}$
	$f(\theta_1^*, \theta_2^*, \theta_3^*)$ Δ_3	51.1204 -0.0424	34.3548 0
$G > C$	$(\theta_1^*, \theta_2^*, \theta_3^*)$ 6 optimal points $\in \{(-76^\circ, 60^\circ, 60^\circ), (-60^\circ, -60^\circ, 76^\circ), (-60^\circ, 76^\circ, -60^\circ), (60^\circ, -76^\circ, 60^\circ), (60^\circ, 60^\circ, -76^\circ), (76^\circ, -60^\circ, -60^\circ)\}$	Table cell (g) of Table 2.6: 6 optimal points $\in \{(-76^\circ, 60^\circ, 60^\circ), (-60^\circ, -60^\circ, 76^\circ), (-60^\circ, 76^\circ, -60^\circ), (60^\circ, -76^\circ, 60^\circ), (60^\circ, 60^\circ, -76^\circ), (76^\circ, -60^\circ, -60^\circ)\}$	Table cell (f) of Table 2.6: 3 optimal points $\in \{(-33^\circ, 31^\circ, 31^\circ), (31^\circ, -33^\circ, 31^\circ), (31^\circ, 31^\circ, -33^\circ)\}$
	$f(\theta_1^*, \theta_2^*, \theta_3^*)$ Δ_3	42.8827 -0.1451	10.0621 0
$G >> C$	$(\theta_1^*, \theta_2^*, \theta_3^*)$ 6 optimal points $\in \{(-90^\circ, -90^\circ, 90^\circ), (-90^\circ, 90^\circ, -90^\circ), (-90^\circ, 90^\circ, 90^\circ), (90^\circ, -90^\circ, -90^\circ), (90^\circ, -90^\circ, 90^\circ), (90^\circ, 90^\circ, -90^\circ)\}$	Table cell (i) of Table 2.6: 6 optimal points $\in \{(-90^\circ, -90^\circ, 90^\circ), (-90^\circ, 90^\circ, -90^\circ), (-90^\circ, 90^\circ, 90^\circ), (90^\circ, -90^\circ, -90^\circ), (90^\circ, -90^\circ, 90^\circ), (90^\circ, 90^\circ, -90^\circ)\}$	Table cell (h) of Table 2.6: 1 optimal point $\in \{(59^\circ, 59^\circ, 59^\circ)\}$
	$f(\theta_1^*, \theta_2^*, \theta_3^*)$ Δ_3	28.2100 -0.3361	1.2400 0
			Table cell (c) of Table 2.6: 1 optimal point $\in \{(0^\circ, 0^\circ, 0^\circ)\}$
			Table cell (j) of Table 2.6: 3 optimal points $\in \{(-90^\circ, -90^\circ, 90^\circ), (-90^\circ, 90^\circ, -90^\circ), (90^\circ, -90^\circ, -90^\circ)\}$
			Table cell (k) of Table 2.6: 1 optimal point $\in \{(90^\circ, 90^\circ, 90^\circ)\}$
			Table cell (l) of Table 2.6: 3 optimal points $\in \{(-90^\circ, -90^\circ, 90^\circ), (-90^\circ, 90^\circ, -90^\circ), (90^\circ, -90^\circ, -90^\circ)\}$
			25.9671 0.1494

2.5.2 Summary of the Key Findings and Discussions of the Results

To evaluate the effects of different numbers of PV cells, the same consumption profile $C(t)$ is used among corresponding table cells in different tables whenever possible. For example, the table cell (a) of Table 2.2 corresponds to the table cell (a) of Table 2.4 and to the table cell (a) of Table 2.6. The comparisons between the different tables are fair because the total surface area A is constant. In other words, there will be no more surface area added by adding another PV cell, instead the total surface area A is divided among N PV cells in each scenario. The only exception is that the table cells (d), (g), and (j) of Table 2.2 cannot be compared directly to Table 2.4 or Table 2.6 because their energy consumption profile $C(t)$ is different.

From a practical point of view, the optimization algorithm is faster for only a few PV cells (1 or 2 PV cells) than for several PV cells (more than 2 PV cells). In addition, if there are several PV cells with different optimal orientation angles, the spacing between the differently oriented PV cells has to be sufficient enough to avoid shadowing effects on the panels. This increases the area needed for deployment of the PV cells. Furthermore, it is not possible to mount PV cells with different orientation angles on the same array or support structure which increases the material cost for buying several arrays or support structures. Hence, it is recommended to use as less differently oriented PV cells as possible.

If $G \ll C$ (first rows in Table 2.3, Table 2.5, and Table 2.7), all PV cells should be oriented towards the south, i.e., the optimal orientation angles are $\theta_1^* = \theta_2^* = \dots = \theta_N^* = 0^\circ$. If $G \ll C$, the optimal orientation angles are independent of the shape of the energy consumption profile.

The optimal orientation angles change from south orientation in the $G \ll C$ scenarios towards the east and/or west orientation in the $G \gg C$ scenarios in every column of the Table 2.2, Table 2.4, and Table 2.6. The optimal orientation angles

in the $G < C$ scenarios are closer to the south orientation than the east and/or west orientation, whereas the optimal orientation angles in the $G > C$ scenarios are closer to the east and/or west orientation than the south orientation.

The gains of adding the first, second, and third PV cell with optimized orientation angle to the system model 1 are evaluated in the following paragraphs.

2.5.2.1 PV Cells with Default Orientation Angles

The centers of the stripes, squares, and cubes in Table 2.2, Table 2.4, and Table 2.6 are the normalized energy drawn from the main grid, i.e. $f(0^\circ)$, $f(0^\circ, 0^\circ)$, and $f(0^\circ, 0^\circ, 0^\circ)$, if no orientation angle optimization is performed, respectively. PV cells are oriented towards the south in the northern hemisphere by default (cf. Table 1.1). $f(0^\circ) = f(0^\circ, 0^\circ) = f(0^\circ, \dots, 0^\circ)$ if the same consumption profile $C(t)$ is used because the total surface area A in the system model 1 is constant. For example, $f(0^\circ)$ in Table 2.2(a) equals to $f(0^\circ, 0^\circ)$ in Table 2.4(a) and $f(0^\circ, 0^\circ, 0^\circ)$ in Table 2.6(a).

2.5.2.2 Adding the First PV Cell with Optimized Orientation Angle

A positive (negative) Δ_1 value represents an improvement (deterioration) in performance of the system if the first PV cell is added. $\Delta_1 > 0$ for the table cells (d)-(l) and $\Delta_1 = 0$ for the table cells (a)-(c) in Table 2.3. The greatest Δ_1 values for the constant, business, and residential load profiles in Table 2.3 are 0.3829 (table cell (j)), 2.3318 (table cell (h)), and 1.5493 (table cell (l)), respectively. The optimized values $f(\theta_1^*)$ (red lines in Table 2.2) are usually significantly greater than the default values $f(0^\circ)$ (centers of the stripes in Table 2.2). In other words, orientation angle optimization improves the system performance in most scenarios. Δ_1 is always greater or equal to 0 because $f(0^\circ) \geq f(\theta_1^*)$. That means the system performance can only be improved and will never worsen by adding the first PV cell. It should be pointed out that a load profile type can have an optimal orientation angle on

the east side ($\theta^* < 0^\circ$), on the west side ($\theta^* > 0^\circ$), as well as oriented southwards ($\theta^* = 0^\circ$) in different scenarios as it can be seen for the residential load profiles (third column) in Table 2.2.

2.5.2.3 Adding the Second PV Cell with Optimized Orientation Angle

$\Delta_2 > 0$ for all table cells in Table 2.5 with two optimal points, i.e., (d), (f)-(g), and (i)-(j). $\Delta_2 = 0$ for all table cells in Table 2.5 with only one optimal point, i.e., (a)-(c), (e), (h), and (k)-(l). The greatest Δ_2 values for the constant, business, and residential load profiles in Table 2.5 are 2.0891 (table cell (j)), 0 (table cells (b), (e), (h), and (k)), and 0.5424 (table cell (i)), respectively. The Δ_2 values are usually smaller than the Δ_1 values for the business and residential load profiles, whereas the Δ_2 values are usually greater than the Δ_1 values for the constant load profiles. Consumption profiles which are similar to the constant profile, e.g., the scenarios in the first column, can often improve their performance ($\Delta_2 > 0$) by choosing orientation angles with opposite algebraic signs, e.g., $\theta_1^* > 0^\circ$ and $\theta_2^* < 0^\circ$, as seen in table cells (d), (g), and (j) in Table 2.5. Consumption profiles which have significant local maxima in the morning as well as in the afternoon, e.g., the residential load profile scenarios in the third column, can often improve their performance ($\Delta_2 > 0$) by choosing orientation angles with opposite algebraic signs, e.g., $\theta_1^* > 0^\circ$ and $\theta_2^* < 0^\circ$, as seen in table cells (f), and (i) in Table 2.5. Consumption profiles which have only one significant maximum, e.g., the business load profile scenarios in the second column, cannot improve their performance ($\Delta_2 = 0$) by adding a second PV cell.

2.5.2.4 Adding the Third PV Cell with Optimized Orientation Angle

$\Delta_3 > 0$ for the table cell (l) in Table 2.7. $\Delta_3 = 0$ for all table cells in Table 2.7 with only one optimal point, i.e., (a)-(c), (e), (h), and (k). $\Delta_3 < 0$ for the table cells (d), (f)-(g), and (i)-(j) in Table 2.7. The greatest and lowest Δ_3 values for the constant, business, and residential load profiles in Table 2.7 are 0 and -0.3361 , 0 and 0, and

0.1494 and -0.0296 , respectively. The Δ_3 values are usually smaller than the Δ_2 values and sometimes even negative. That means that adding the third PV cell only improves the system performance slightly in some rare scenarios, whereas the system performance worsens in most other scenarios. Consumption profiles which are similar to the constant profile worsen their performance ($\Delta_3 < 0$) in most scenarios because 3 PV cells cannot equally shift the energy generation peak towards the morning and afternoon hours. Either two PV cells have positive algebraic signs and one PV cell has a negative algebraic sign or the other way around, as seen in table cells (d), (g), and (j) in Table 2.7. Consumption profiles which have two significant local maxima in the morning as well as in the afternoon, e.g., the residential load profile scenarios in the third column, can slightly improve ($\Delta_3 > 0$) or slightly worsen ($\Delta_3 < 0$) their performance, as seen in table cells (l), and (i) in Table 2.7. Consumption profiles which have only one significant maximum, e.g., the business load profile scenarios in the second column, cannot improve their performance ($\Delta_3 = 0$) by adding a third PV cell. In general, consumption profiles which have three significant local maxima between sunrise and sunset or consumption profiles which have two significant local maxima (with one maxima significantly greater than the other one) might benefit in some scenarios from 3 PV cells. But it becomes more and more difficult to find such specific consumption profiles and scenarios to justify that 3 or more PV cells are necessary to improve the system performance significantly.

2.6 Summary of Chapter 2

In Chapter 2, the orientation angles of N PV cells powering one BS were jointly optimized to improve the match between the two profiles on a daily timescale. The energy generation profiles of randomly inclined and oriented PV cells were analytically derived by the irradiance values received at a horizontally-mounted PV cell at the same location. The energy drawn per day from the main grid by the BS given

its energy consumption profile was used as the performance metric to determine the optimal set of orientation angles. The main results are that the system performance ($\Delta_1 > 0$) can be increased significantly by deploying one PV cell with optimal orientation angle θ_1^* (or several PV cells with the same orientation angle θ_1^*) if the energy generation of the PV cell is slightly smaller ($G < C$), is slightly greater ($G > C$), or is significantly greater ($G \gg C$) than the energy consumption of the BS. This is caused by the ability to shift the energy generation peak from noon towards the most significant local maximum between sunrise and sunset of the energy consumption profile. Furthermore, the system performance ($\Delta_2 > 0$) can be further increased by deploying two PV cells with jointly optimized orientation angles θ_1^* and θ_2^* (or several PV cells where half of them are deployed with θ_1^* and the other half with θ_2^*) if a constant energy consumption profile or a consumption profile with significant local maxima in the morning as well as in the afternoon are given. This is caused by the ability to shift the energy generation peak from noon towards the morning with east-oriented PV cells, while the other west-oriented PV cells shift the energy generation peak towards the afternoon in the northern hemisphere. Because there are only two directions (morning and afternoon) that the energy can be shifted to, the system performance can not be further increased significantly by deploying more than 2 differently oriented PV cells. More than 2 differently oriented PV cells may even degrade the system performance ($\Delta_3 < 0$) in some scenarios.

Chapter 3

Impact of the Battery Capacity on the Optimal Orientation Angle of a PV Cell

Chapter 3 will extend the system model in Chapter 2 by adding a battery to the BS. The battery is modeled by a Markov chain in this chapter. The system model in Chapter 2 has no batteries deployed at the BS. Nonetheless, Chapter 2 can be seen as special case of Chapter 3 because the batteries can have a battery capacity of 0 in the system model of Chapter 3.

3.1 Literature Review: Batteries at BSs

It has been shown that the resiliency of cellular networks in disaster events, such as earthquakes and hurricanes, is higher if the energy mix of the cellular networks includes harvest renewable energy instead of relying solely on the power from the main grid [57]. The service of the cellular network usually breaks down during a disaster event because power lines are damaged and the BSs run out of energy. In addition, back-up generators rely on petrol, which has to be transported to the

sites of the BSs via roads, which are often damaged as well in disaster events. Because the cellular network service is so vital during a disaster event to coordinate rescue missions, police operations, and military operations, the cellular network is required to be operational 99.999% of the time during a year, whereas the power grid is required to be operational only 99.9% in the U.S. [13]. In other words, the total yearly outage time of the power grid is less than nine hours, whereas the requirements for cellular networks is much higher than that. Because power grids have lower reliability requirements than that of cellular networks, BSs are typically equipped with batteries that last for a few hours. The capacity of the batteries is usually around four hours but can be higher for some BSs as well [13].

PV cells have a very strong diurnal cycle. [37, 58] showed that a storage capacity of six hours of the average consumption of the appliance is sufficient to smoothen the diurnal cycle of the PV cells. In scenarios where only solar energy is harvested and no other energy sources are available, a storage capacity of twelve hours was recommended by [37, 58].

A life cycle energy cost assessment at a stand-alone PV system was conducted in [59] to evaluate the long term benefits of shifting the energy consumption profile towards the energy generation profile. A better match of both profiles led to a longer battery lifetime due to less battery charging-discharging cycles and the opportunities to downsize the battery capacity and PV cell surface area.

A good match between the energy generation profile of the PV cell and the energy consumption profile of the BS can be achieved by either installing a small battery (or no battery) with orientation angle optimization or installing a large battery without orientation angle optimization. Nonetheless, batteries are expensive (25 - 250€, 220€ and 1500€ per kWh for the battery types Lead-Acid, NaS and Li-Ion, respectively [60]) and have a short lifetime (3 - 9 years [61]) compared with the warranty lifetimes of PV cells (PV cell manufacturers guarantee a 80% system performance warranty for around 20 years [62]). Therefore, battery replacements significantly

contribute to the system lifetime cost [61]. Small batteries with orientation angle optimization are practically the more cost-effective option compared with large batteries without orientation angle optimization.

Markov chain models have been used in the literature to model batteries, as seen in [63–65].

3.2 Contributions of Chapter 3

The contributions of Chapter 3 are summarized as follows:

- Developing a PV cell's orientation angle optimization algorithm with Markov chain based battery model of a solar-powered BS with battery. The algorithm takes into account the battery capacity and the energy consumption profile of the BS. The number of user equipments (UEs) served by the BS throughout the day $\overline{S_{\text{UE}}}(\theta)$ is used as the performance metric to identify the optimal orientation angle.
- Verifying the accuracy of the proposed algorithm by showing that simulation trials converge based on the law of large numbers to the output $\overline{S_{\text{UE}}}(\theta)$ of the proposed algorithm.
- Showing that the proposed algorithm (depends on the number of battery states) requires a shorter running time than the simulation trials (depends on the number of trials) for moderate battery state resolutions.
- Investigating the dependency of the optimal PV cell orientation angle on the given battery capacity.

3.3 System Model 2 - One PV Cell Powering a BS with Battery

Figure 3.1 depicts the system model 2 considered in this chapter. It consists of an energy generation part with one PV cell, an energy storage part made of a battery, and an energy consumption part composed of a BS. The energy flow follows the arrows in Figure 3.1 and can only be altered by choosing different orientation angles for the PV cell. All other parameters will be fixed. The energy generation flow is denoted by $G_{\theta,1}(t)$ in Figure 3.1. The energy consumption flow is divided in a load-independent part, denoted by c_{con} , and a load-dependent part, denoted by $c_{\theta}(t)$, in Figure 3.1.

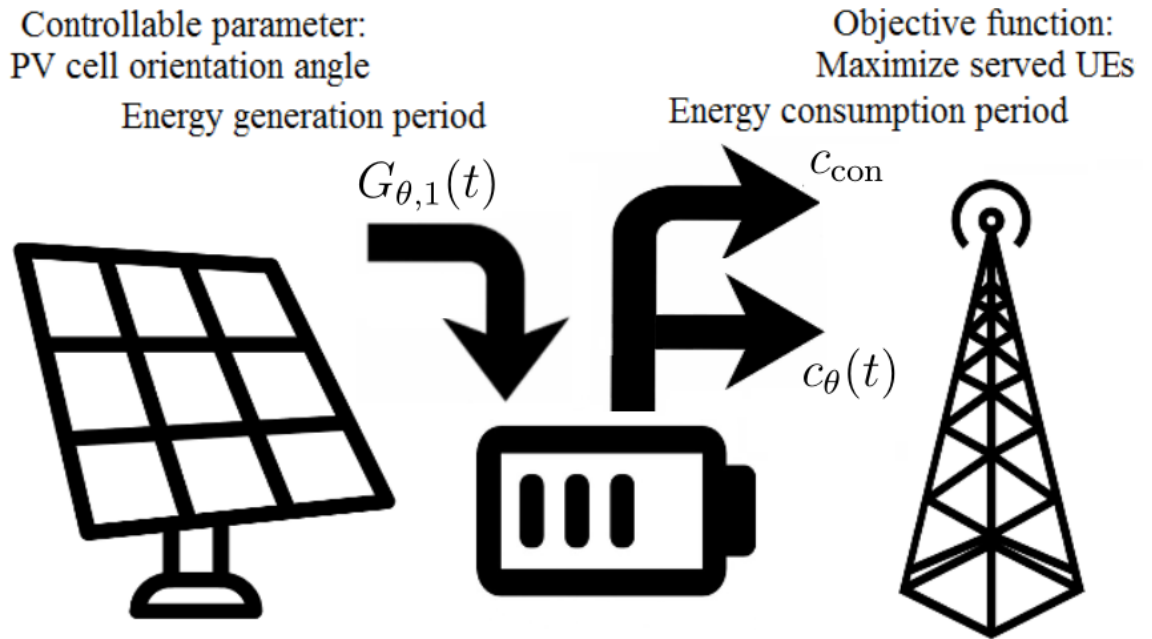


Figure 3.1: Illustration of system model 2

3.3.1 Solar Energy Storage Model

The BS is only powered by a PV cell. The only controllable parameter in the system model 2 is the PV cell orientation angle. The day is divided into T time steps. The index of a time step is denoted by $t \in \{1, \dots, T\}$. Each time step has

three distinguish flows, first the energy generation flow will be executed followed by the load-independent energy consumption flow and then the load-dependent energy consumption flow (cf. Figure 3.1). During the energy generation flow, the amount of generated energy in this time step is calculated and stored in the battery. During the energy consumption flows, the amount of consumed energy by the BS in this time step is subtracted from the battery. In reality all three periods occur simultaneously. For applications that require a simultaneous energy generation and consumption, the length of the time steps can be chosen small enough to achieve a nearly simultaneous energy generation and consumption.

3.3.2 Energy Generation Flow and Load-independent Energy Consumption Flow

The formula for the normalized energy generated by one PV cell deployed with orientation angle θ at time step t , denoted by $G_{\theta,1}(t)$, has been derived in Chapter 2 and can be calculated by (2.2).

The battery has an upper bound and a lower bound that determine how much of the generated energy $G_{\theta,1}(t)$ can be stored in the battery. In addition, the load-independent energy consumption of the BS, denoted by c_{con} , has to be subtracted from the battery at the beginning of each time step.

The available energy, denoted by $a_{\theta}(t)$, in the battery at time step t is as follows:

$$a_{\theta}(t) = \max\{0, \min\{b_{\theta}(t-1) + G_{\theta,1}(t) - c_{\text{con}}, b_{\text{max}}\}\}, \quad (3.1)$$

where $b_{\theta}(t-1)$ is the stored energy in the battery in time step $t-1$, c_{con} is the load-independent energy consumption of the BS during one time step, and b_{max} is the maximum battery capacity. The min in (3.1) ensures that the stored energy in the battery is less or equal the maximum battery capacity. The max in (3.1) ensures

that the stored energy in the battery is greater or equal 0.

The amount of energy stored in the battery at time step 0 is b_{begin} as follows:

$$b_{\theta}(0) = b_{\text{begin}}. \quad (3.2)$$

3.3.3 Load-dependent Energy Consumption Flow

To model the temporal fluctuation of the BS's energy consumption, the number of user equipments (UEs) connected to the BS at time step t is modeled by a random variable $l(t)$, which follows a Poisson distribution (PD) with density parameter $\lambda(t)$. The number of UEs in the coverage area of a BS is commonly modeled as a Poisson point process in the literature [66–68]. Hence, $l(t)$ is as follows:

$$l(t) := \text{PD}(\lambda(t)). \quad (3.3)$$

Without loss of generality, it is assumed that the BS is located in a business-area. The traffic load profile of a BS in a business-area, denoted by $C_{\text{bus}}(t)$, has been derived in Chapter 2 and is given in Figure 2.8. Nonetheless, the analysis can be applied to any other location and traffic load profile as well. Hence, the density parameter $\lambda(t)$ is as follows:

$$\lambda(t) = C_{\text{bus}}(t). \quad (3.4)$$

The number of served UEs¹ by the BS at time step t , denoted by $s_{\theta}(t)$, is limited either by the number of UEs connected to the BS or the available energy as follows:

¹UEs that cannot be served by the BS due to a lack of renewable stored energy in the battery might be off-loaded to other BSs or the BS uses main grid energy to serve these UEs. Only UEs which are served by the available renewable energy will be counted by $s_{\theta}(t)$.

$$s_{\theta}(t) = \min \left\{ l(t), \left\lfloor \frac{a_{\theta}(t)}{c_{\text{UE}}} \right\rfloor \right\}, \quad (3.5)$$

where $a_{\theta}(t)$ is the available energy at time step t , and c_{UE} is the average amount of energy needed to serve one UE.

The load-dependent energy consumption $c_{\theta}(t)$ of the BS in time step t is given by

$$c_{\theta}(t) = s_{\theta}(t) \cdot c_{\text{UE}}. \quad (3.6)$$

The residual energy in the battery at the end of time step t can be calculated by

$$b_{\theta}(t) = a_{\theta}(t) - c_{\theta}(t). \quad (3.7)$$

3.3.4 Determination of the Average Number of Served UEs

Eq. (3.5) ensures that the consumed energy by the BS is less than or equal to the stored energy in the battery. As a result, it is possible that some UEs cannot be served² by the BS due to a lack of renewable stored energy. Therefore, the number of served UEs $S_{\text{UE}}(\theta)$ throughout the day by a PV cell with orientation angle θ is used as the performance metric, where $S_{\text{UE}}(\theta)$ is as follows:

$$S_{\text{UE}}(\theta) = \sum_{t=1}^T s_{\theta}(t). \quad (3.8)$$

Because the $l(t)$ values are random variables, $\overline{S_{\text{UE}}}(\theta)$ denotes the average value of $S_{\text{UE}}(\theta)$.

²UEs that cannot be served by the BS due to a lack of renewable stored energy might be off-loaded to other BSs or the BS uses main grid energy to serve these UEs. Only UEs which are served by the available renewable stored energy will be counted by $s_{\theta}(t)$.

The orientation angle θ which achieves the highest $\overline{S_{\text{UE}}}(\theta)$ value is considered as optimal orientation angle θ^* as follows:

$$\theta^* = \arg \max_{\theta} \overline{S_{\text{UE}}}(\theta). \quad (3.9)$$

3.4 Orientation Angle Optimization Algorithm with Markov Chain Based Battery

The following PV cell's orientation angle optimization algorithm with Markov chain based battery model (Algorithm 1) can efficiently determine the optimal orientation angle of the PV cell at a BS with battery. To show the effectiveness of the proposed algorithm, a simulation algorithm (Algorithm 2) will be developed in the Section 3.5 as well. The advantages of the proposed algorithm in comparison with the simulation algorithm (Algorithm 2) with respect to accuracy and running time will be evaluated in Section 3.6.

All energy values are discretized with a precision of μ , i.e., $\tilde{G}_{\theta,1}(t)$ will be the closest multiple of μ from $G_{\theta,1}(t)$. For example, if $\mu = \frac{1}{1000}$, and $G_{\theta,1}(t) = 1.2756$, then $\tilde{G}_{\theta,1}(t) = 1.276$.

There are $S_{\text{max}} = \frac{b_{\text{max}}}{\mu} + 1$ battery energy states. The battery energy states $0, 1, 2, 3, \dots$, and $\frac{b_{\text{max}}}{\mu}$ represent $0, \mu, 2 \cdot \mu, 3 \cdot \mu, \dots$, and b_{max} units of normalized energy, respectively. Without loss of generality, $b_{\text{begin}}, b_{\text{max}}, c_{\text{UE}}$, and c_{con} are multiple of μ .

The expression $\mathbb{P}(a_{\theta}(t) = i) = x$ means that the probability of having i units of normalized energy available in the battery at the beginning of time step t is x . The expression $\mathbb{P}(b_{\theta}(t) = i) = x$ means that the probability of the battery having stored i units of normalized energy at the end of time step t is x .

The following subsections will go through the Algorithm 1 line by line. The expres-

sion $\lfloor x \rfloor$ means that the variable x is rounded down to the nearest integer value.

3.4.1 Markov Chain Initialization

Because $l(t)$ is a Poisson distributed random variable, $\mathbb{P}(l(t) = r)$, and $\mathbb{P}(l(t) \geq r)$ are $\frac{\lambda(t)^r \cdot e^{-\lambda(t)}}{r!}$, and $1 - \sum_{w=0}^{r-1} \frac{\lambda(t)^w \cdot e^{-\lambda(t)}}{w!}$, respectively [69] (Algorithm 1 line: 1 - 2).

S_{\max} is initialized (Algorithm 1 line: 5). The initial battery state $b_{\theta}(0)$ is equal to b_{begin} at the beginning of Algorithm 1. Therefore, the probability of the battery state being b_{begin} at time step 0 is 1, whereas all the other battery states have a probability of 0 (Algorithm 1 line: 6 - 7). There are no UEs served at the beginning of Algorithm 1 (Algorithm 1 line: 8). Eq. (3.4) is used to calculate the UE density parameters $\lambda(t)$ for all time steps (Algorithm 1 line: 10).

3.4.2 Energy Generation Flow and Load-independent Energy Consumption Flow of Algorithm 1

All $\mathbb{P}(a_{\theta}(t) = i)$ values are set at 0 at the beginning (Algorithm 1 line: 14). If the battery is in state i , S_{Shift} calculates the new battery state after the generated energy $\tilde{G}_{\theta,1}(t)$ is added to the battery and the load-independent energy consumption of the BS c_{con} is subtracted from the battery (Algorithm 1 line: 16). S_{Shift} takes into account the upper bound and the lower bound of the battery (Algorithm 1 line: 16). If $\tilde{G}_{\theta,1}(t) > c_{\text{con}}$, then every battery state increases by $\frac{\tilde{G}_{\theta,1}(t) - c_{\text{con}}}{\mu}$ battery states or reaches the maximum battery state $S_{\max} - 1$ if it comes to a battery overflow. This is depicted in Figure 3.2. If $\tilde{G}_{\theta,1}(t) < c_{\text{con}}$, then every battery state decreases by $\frac{c_{\text{con}} - \tilde{G}_{\theta,1}(t)}{\mu}$ battery states or reaches the minimum battery state 0 if the battery depletes. This is depicted in Figure 3.3. If $\tilde{G}_{\theta,1}(t) = c_{\text{con}}$, there is no energy added or subtracted from the battery. Each transition occurs with a probability of 1, which is depicted on top of each arrow in Figures 3.2 - 3.3.

The probability of the battery state being i at the time step $t-1$, i.e., $\mathbb{P}(b_\theta(t-1) = i)$, is added to the probability of the new battery state, i.e., $\mathbb{P}(a_\theta(t) = S_{\text{Shift}})$ (Algorithm 1 line: 17).

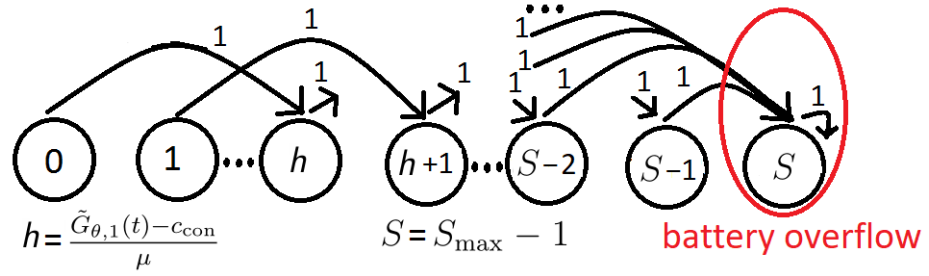


Figure 3.2: Energy generation flow and load-independent energy consumption flow if $\tilde{G}_{\theta,1}(t) > c_{\text{con}}$

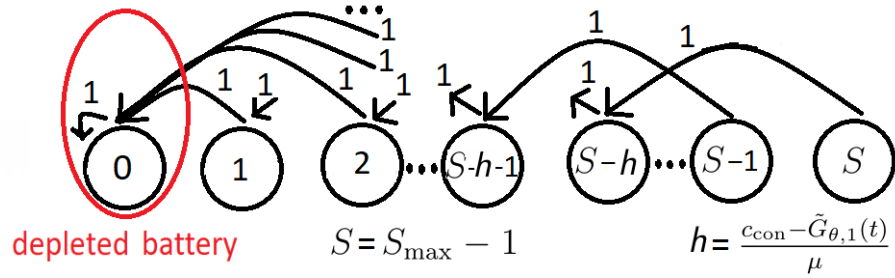


Figure 3.3: Energy generation flow and load-independent energy consumption flow if $\tilde{G}_{\theta,1}(t) < c_{\text{con}}$

3.4.3 Load-dependent Energy Consumption Flow of Algorithm 1

The number of UEs in the coverage area of the BS, denoted by $l(t)$, is Poisson distributed with density parameter $\lambda(t)$, i.e., $l(t) := \text{PD}(\lambda(t))$. The probability of $l(t)$ to be equal to an integer value r , denoted by $\mathbb{P}(l(t) = r)$, is given for a Poisson distribution by $\frac{\lambda(t)^r \cdot e^{-\lambda(t)}}{r!}$ [69] (Algorithm 1 line: 1). The expression $\mathbb{P}(l(t) \geq r)$ is given for a Poisson distribution by $1 - \sum_{w=0}^{r-1} \frac{\lambda(t)^w \cdot e^{-\lambda(t)}}{w!}$ [69] (Algorithm 1 line: 2).

Each served UE consumes c_{UE} units of normalized energy in each time step. Therefore, every battery state has to be decreased by $\frac{c_{\text{UE}}}{\mu}$ battery states for every served UE in each time step.

This paragraph derives the update formulas for the battery states from $\frac{c_{\text{UE}}}{\mu}$ to $S_{\text{max}} -$

1 (Algorithm 1 line: 29 - 30). Figure 3.4 shows only the incoming arrows for the battery state $\frac{c_{UE}}{\mu}$ as an example. The battery state $i \in \{\frac{c_{UE}}{\mu}, \dots, S_{\max} - 1\}$ has $\lfloor \frac{(S_{\max}-1-i) \cdot \mu}{c_{UE}} \rfloor + 1$ incoming arrows. $r \in \{0, \dots, \lfloor \frac{(S_{\max}-1-i) \cdot \mu}{c_{UE}} \rfloor\}$ describes the transition from battery state $i + r \cdot \frac{c_{UE}}{\mu}$ to battery state i when exactly r UEs are served. The transition probability is $\mathbb{P}(l(t) = r)$ for this transition which is depicted next to the transition arrow in Figure 3.4.

This paragraph derives the update formulas for the battery states from 0 to $\frac{c_{UE}}{\mu} - 1$ (Algorithm 1 line: 27 - 28). Figure 3.5 shows only the incoming arrows for the battery state 0 as an example. The battery state $i \in \{0, \dots, \frac{c_{UE}}{\mu} - 1\}$ has $\lfloor \frac{(S_{\max}-1-i) \cdot \mu}{c_{UE}} \rfloor + 1$ incoming arrows. $r \in \{0, \dots, \lfloor \frac{(S_{\max}-1-i) \cdot \mu}{c_{UE}} \rfloor\}$ describes the transition from battery state $i + r \cdot \frac{c_{UE}}{\mu}$ to battery state i when more than $r - 1$ UEs are in the coverage area of the BS, which means the BS can only serve r UEs and the remaining UEs cannot be served due to the lack of available renewable stored energy. The transition probability is $\mathbb{P}(l(t) \geq r)$ for this transition which is depicted next to the transition arrow in Figure 3.5.

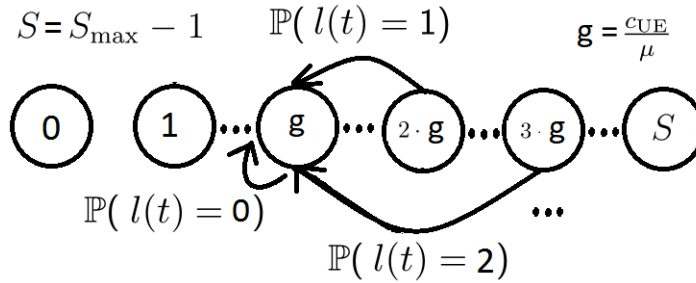


Figure 3.4: Energy consumption flow for the battery state $\frac{c_{UE}}{\mu}$

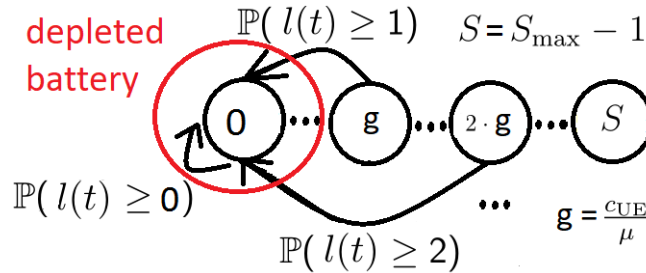


Figure 3.5: Energy consumption flow for the battery state 0

3.4.4 Determination of the Average Number of Served UEs of Algorithm 1

When the battery is in state i , it can serve $r \in \{0, \dots, \lfloor \frac{i \cdot \mu}{c_{\text{UE}}} \rfloor\}$ UEs. When $r \in \{0, \dots, \lfloor \frac{i \cdot \mu}{c_{\text{UE}}} \rfloor - 1\}$, the energy in the battery is decreased from battery state i with the transition probability of $\mathbb{P}(l(t) = r)$. Exactly r UEs were served, that is why the expression in Algorithm 1 line: 22 is multiplied by r . When $r = \lfloor \frac{i \cdot \mu}{c_{\text{UE}}} \rfloor$, the energy in the battery is decreased from battery state i with the transition probability of $\mathbb{P}(l(t) \geq \lfloor \frac{i \cdot \mu}{c_{\text{UE}}} \rfloor)$. Exactly $\lfloor \frac{i \cdot \mu}{c_{\text{UE}}} \rfloor$ UEs were served, that is why the expression in Algorithm 1 line: 24 is multiplied by $\lfloor \frac{i \cdot \mu}{c_{\text{UE}}} \rfloor$.

The PV cell's orientation angle optimization algorithm with Markov chain based battery model is summarized as follows:

Algorithm 1: PV cell's orientation angle optimization algorithm with Markov chain based battery model

Input: $\gamma, \mu, T, b_{\text{begin}}, b_{\text{max}}, c_{\text{con}}, c_{\text{UE}}, \tilde{G}_{\theta,1}(t) \forall t \forall \theta$, and $C_{\text{bus}}(t) \forall t$

Output: θ^*

```

1: %  $\mathbb{P}(l(t) = r) = \frac{\lambda(t)^r \cdot e^{-\lambda(t)}}{r!}$ 
2: %  $\mathbb{P}(l(t) \geq r) = 1 - \sum_{w=0}^{r-1} \frac{\lambda(t)^w \cdot e^{-\lambda(t)}}{w!}$ 
3: for all  $\theta \in \{-40^\circ, -35^\circ, \dots, 90^\circ\}$  do
4:   % Initialization
5:    $S_{\text{max}} = \frac{b_{\text{max}}}{\mu} + 1$ 
6:    $\mathbb{P}(b_\theta(0) = \frac{b_{\text{begin}}}{\mu}) = 1$ 
7:    $\mathbb{P}(b_\theta(0) = i) = 0 \quad \forall i \in \{0, \dots, S_{\text{max}} - 1\} \setminus (\frac{b_{\text{begin}}}{\mu})$ 
8:    $\overline{S_{\text{UE}}}(\theta) = 0$ 
9:   for  $t = 1 : T$  do
10:     $\lambda(t) = C_{\text{bus}}(t)$ 
11:   end for
12:  for  $t = 1 : T$  do
13:    % Energy generation flow and load-independent energy consumption flow
14:     $\mathbb{P}(a_\theta(t) = i) = 0 \quad \forall i \in \{0, \dots, S_{\text{max}} - 1\}$  % Initialization
15:    for  $i \in \{0, \dots, S_{\text{max}} - 1\}$  do
16:       $S_{\text{Shift}} = \max\{0, \min\{i + \frac{\tilde{G}_{\theta,1}(t) - c_{\text{con}}}{\mu}, \frac{b_{\text{max}}}{\mu}\}\}$ 
17:       $\mathbb{P}(a_\theta(t) = S_{\text{Shift}}) = \mathbb{P}(a_\theta(t) = S_{\text{Shift}}) + \mathbb{P}(b_\theta(t-1) = i)$ 

```

```

18:     end for

19:     % Adding the average number of UEs served at time step  $t$  to  $\overline{S_{\text{UE}}}(\theta)$ 
20:     for  $i = 0 : S_{\text{max}} - 1$  do
21:         for  $r = 0 : \lfloor \frac{i \cdot \mu}{c_{\text{UE}}} \rfloor - 1$  do
22:              $\overline{S_{\text{UE}}}(\theta) = \overline{S_{\text{UE}}}(\theta) + r \cdot \mathbb{P}(l(t) = r) \cdot \mathbb{P}(a_{\theta}(t) = i)$ 
23:         end for
24:          $\overline{S_{\text{UE}}}(\theta) = \overline{S_{\text{UE}}}(\theta) + \lfloor \frac{i \cdot \mu}{c_{\text{UE}}} \rfloor \cdot \mathbb{P}(l(t) \geq \lfloor \frac{i \cdot \mu}{c_{\text{UE}}} \rfloor) \cdot \mathbb{P}(a_{\theta}(t) = i)$ 
25:     end for

26:     % Load-dependent energy consumption flow
27:      $\mathbb{P}(b_{\theta}(t) = i) = \sum_{r=0}^{\lfloor \frac{(S_{\text{max}}-1-i) \cdot \mu}{c_{\text{UE}}} \rfloor} \left( \mathbb{P}(l(t) \geq r) \cdot \mathbb{P}(a_{\theta}(t) = i + r \cdot \frac{c_{\text{UE}}}{\mu}) \right)$ 
28:      $\forall i \in \{0, \dots, \frac{c_{\text{UE}}}{\mu} - 1\}$ 
29:      $\mathbb{P}(b_{\theta}(t) = i) = \sum_{r=0}^{\lfloor \frac{(S_{\text{max}}-1-i) \cdot \mu}{c_{\text{UE}}} \rfloor} \left( \mathbb{P}(l(t) = r) \cdot \mathbb{P}(a_{\theta}(t) = i + r \cdot \frac{c_{\text{UE}}}{\mu}) \right)$ 
30:      $\forall i \in \{\frac{c_{\text{UE}}}{\mu}, \dots, S_{\text{max}} - 1\}$ 
31: end for
32: end for
33: return  $\theta^* = \arg \max_{\theta \in [-90^\circ, 90^\circ]} \overline{S_{\text{UE}}}(\theta)$ 

```

3.5 Derivation of a Simulation Algorithm as Baseline

Eqs. (3.1) - (3.9) are used to derive the following simulation algorithm (Algorithm 2). Algorithm 2 is the baseline for the performance comparison with the shown proposed algorithm (Algorithm 1).

Algorithm 2 Simulation algorithm**Input:** $\gamma, L, T, b_{\text{begin}}, b_{\text{max}}, c_{\text{con}}, c_{\text{UE}}, G_{\theta,1}(t) \forall t \forall \theta$, and $C_{\text{bus}}(t) \forall t$ **Output:** θ^*

```

1: for all  $\theta \in \{-40^\circ, -35^\circ, \dots, 90^\circ\}$  do

2:    $\overline{S_{\text{UE}}}(\theta) = 0$ 
3:   for  $l = 1 : L$  do

4:     % Initialization
5:      $b_\theta(0) = b_{\text{begin}}$ 
6:     for  $t = 1 : T$  do
7:       % Energy generation flow
8:        $a_\theta(t) = \max\{0, \min\{b_\theta(t-1) + G_{\theta,1}(t) - c_{\text{con}}, b_{\text{max}}\}\}$ 

9:       % Energy consumption flow
10:       $\lambda(t) = C_{\text{bus}}(t)$ 
11:       $s_\theta(t) = \min\{\text{PD}(\lambda(t)), \lfloor \frac{a_\theta(t)}{c_{\text{UE}}} \rfloor\}$ ,
12:       $b_\theta(t) = a_\theta(t) - s_\theta(t) \cdot c_{\text{UE}}$ 
13:    end for
14:     $\overline{S_{\text{UE}}}(\theta) = \overline{S_{\text{UE}}}(\theta) + \sum_{t=1}^T s_\theta(t)$ 
15:  end for
16:   $\overline{S_{\text{UE}}}(\theta) = \overline{S_{\text{UE}}}(\theta) / L$ 
17: end for
18: return  $\theta^* = \arg \max_{\theta \in [-90^\circ, 90^\circ]} \overline{S_{\text{UE}}}(\theta)$ 

```

The simulation algorithm (Algorithm 2) has to be run for a large number L until the average of the $S_{\text{UE}}(\theta)$ value converges to a fixed value, denoted by $\overline{S_{\text{UE}}}(\theta)$.

3.6 Results and Discussion

3.6.1 Running Time of the proposed Algorithm and the Simulation Algorithm

The simulation algorithm has a running time of $\mathcal{O}(L \cdot T)$, whereas the proposed algorithm has a running time of $\mathcal{O}(S_{\text{max}}^2 \cdot T)$. Therefore, the proposed algorithm outperforms the simulation algorithm when the battery is not divided into too many battery states S_{max} . Especially for small BSs with small battery capacities, the

proposed algorithm is an effective tool to determine the optimal PV cell orientation.

3.6.2 Accuracy of the Proposed Algorithm and the Simulation Algorithm

The proposed algorithm has the advantage that it can generate the exact $\overline{S_{UE}}(\theta)$ value, whereas the simulation algorithm only converges to the $\overline{S_{UE}}(\theta)$ value. The parameters in Table 3.1 are used for the simulation algorithm and the proposed algorithm. Both algorithms are run for every orientation angle $\theta \in \{-40^\circ, -35^\circ, \dots, 85^\circ, 90^\circ\}$ with constant inclination angle $\gamma = 36^\circ$ (optimal inclination angle for Greenwich (London, UK) in summer). The simulation algorithm is run $L = 100000$ times to achieve a good convergence.

Table 3.1:
Input parameters of system model 2

Parameter	Description	Value
θ	Orientation angle of PV cell	$\in \{-40^\circ, -35^\circ, \dots, 90^\circ\}$
θ^*	Optimal orientation angle of PV cell	$\in \{-40^\circ, -35^\circ, \dots, 90^\circ\}$
γ	Inclination angle of PV cell	36°
$\lambda(t)$	Density parameter of Poisson distributed random variable at time step t	Eq. (3.4)
μ	Precision of the discretization of the energy values/ battery states	$\frac{1}{1000}$
$C_{\text{bus}}(t)$	Business-area traffic load profile at time step t	Figure 2.8
$G_{\theta,1}(t)$	Normalized energy generated by one PV cell installed with θ at time step t	Eq. (2.2)
$\tilde{G}_{\theta,1}(t)$	Closest multiple of μ from $G_{\theta,1}(t)$	
L	Number of loops in simulation algorithm	100000
S_{Shift}	New battery state after $\tilde{G}_{\theta,1}(t)$ is added and c_{con} is subtracted	(Algorithm 1 line: 16)

S_{\max}	Number of battery energy states	$\frac{b_{\max}}{\mu} + 1$
$S_{\text{UE}}(\theta)$	Number of served UEs throughout the day	Eq. (3.8)
$\overline{S_{\text{UE}}}(\theta)$	Average number of served UEs throughout the day	Eq. (3.8)
T	Number of time steps	96
$a_{\theta}(t)$	Available energy in the battery at the beginning of time step t	Eq. (3.1)
$b_{\theta}(t)$	Stored energy in the battery at the end of time step t	Eq. (3.7)
b_{begin}	Amount of energy stored in the battery at time step 0	0
b_{\max}	Battery capacity	$\in \{1, 3, 10\}$
$c_{\theta}(t)$	Load-dependent energy consumption of the BS at time step t	Eq. (3.6)
c_{con}	Load-independent energy consumption of the BS in one time step	0.5
c_{UE}	Average amount of energy needed to serve one UE	0.2
d	Day of the year	165 (June)
lat	Latitude	51.4767° North (Greenwich)
lon	Longitude	0.0003° West (Greenwich)
$l(t)$	Number of UEs connected to the BS at time step t	Eq. (3.3)
$s_{\theta}(t)$	Number of served UEs at time step t	Eq. (3.5)

Figure 3.6 compares the simulation algorithm and the proposed algorithm. It shows

that the simulation algorithm and the proposed algorithm calculate the same $\overline{S_{UE}}(\theta)$ value for each orientation angle θ ($L = 100000$). Therefore, the proposed algorithm accurately describes the limit of the simulation algorithm convergence.

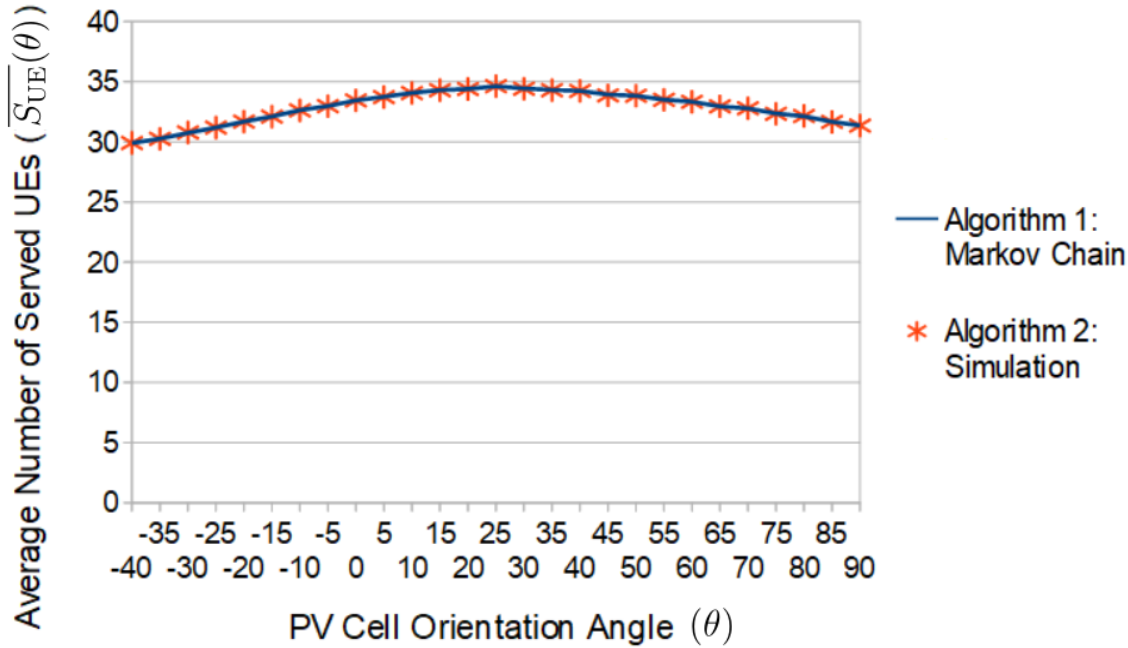


Figure 3.6: Comparison between the proposed algorithm and the simulation algorithm. b_{\max} was set at 3.

3.6.3 Dependency of the Optimal PV Cell Orientation Angle on the Given Battery Capacity

Figure 3.7 plots the average number of served UEs $\overline{S_{UE}}(\theta)$ versus the PV cell orientation angle θ for the three battery capacities: $b_{\max} = 1, 3$, and 10. Figure 3.7 shows that not only the given energy generation and consumption profile is important for the outcome of the optimization but also the battery capacity.

If the battery capacity is small, i.e., $b_{\max} = 1$, a lot of energy is wasted in the morning and midday hours, whereas UEs cannot be served in the afternoon due to a lack of available renewable stored energy in the battery. Therefore, PV cells orientated to the west between 25° to 40° outperform the other orientation angles because west-orientated PV cells shift the energy generation towards the load profile.

If the battery capacity is large, i.e., $b_{\max} = 10$, less energy is wasted in the morning and midday hours due to the larger battery capacity. Therefore, the optimal orientation angle is $\theta^* = 0^\circ$ and the PV cell should be oriented towards the south. South-oriented PV cells generate the most energy throughout the day among all possible orientation angles.

If the battery capacity is moderate, i.e., $b_{\max} = 3$, the optimal orientation angle is between the optimal orientation angles of the other two cases.

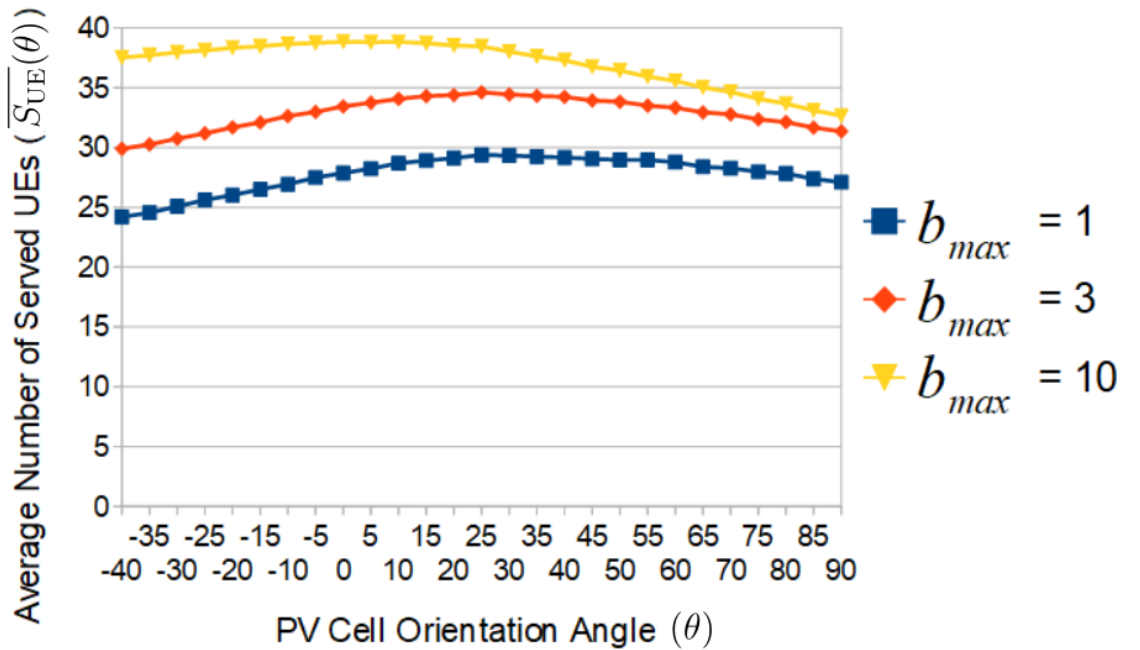


Figure 3.7: Average number of served UEs per day $\overline{S_{UE}}(\theta)$ vs. PV cell orientation angle θ for different battery capacities b_{\max}

3.7 Summary of Chapter 3

In Chapter 3, a battery model was added to the system model. The battery model is based on a Markov chain. The proposed PV cell's orientation angle optimization algorithm with Markov chain based battery model has a running time dependent on the squared number of energy states of the battery S_{\max} and the time resolution T . The number of UEs served by the BS throughout the day $\overline{S_{UE}}(\theta)$ was used as the performance metric to identify the optimal orientation angle. The accuracy

of the proposed algorithm was verified by showing that simulation trials converge based on the law of large numbers to the output $\overline{S_{\text{UE}}}(\theta)$ of the proposed algorithm. The effects of different battery capacities on the optimal PV cell orientation angle were investigated. Whereas BSs with small battery capacities significantly improved their performance by orientation angle optimization, BSs with large battery capacities should orient the PV cells towards the south. The importance of the PV cell orientation angle optimization was verified for a BS with small battery capacity $b_{\text{max}} = 1$ located in a business-area in Greenwich (London, UK) in summer. Also PV cells are normally orientated to the south in Greenwich (London, UK), the algorithm revealed that the optimal orientation angle is between 25° to 40° to the west.

Chapter 4

Optimal Deployment of Energy Harvesters with Anti-correlated Energy Generation Profiles at Base Stations

Chapter 4 will extend the previous system model to a multi-cell cellular network. There are now several BSs distributed in an area and some of them are connected by distribution lines to share the renewable energy among them. The problem investigated in this chapter is how renewable energy harvesters (e.g., a PV cell or a small wind turbine) with anti-correlated energy generation profiles should be deployed to every BS so that the renewable energy can be shared most efficiently in the multi-cell cellular network. Two PV cells that have significantly different orientation angles, such as east-oriented and west-oriented PV cells, are an example for energy harvesters with anti-correlated energy generation profiles.

4.1 Background: Different Power Sharing Methods

The amount of harvested power as well as the power consumption of the BSs vary over time and space resulting in power surpluses or power deficits at the BSs. To avoid wasting precious harvested power, power can be transmitted from surplus BSs to deficit BSs via distribution lines. Other options for power sharing are wireless power transfer, traffic offloading, smart grid/ main grid trading and batteries. These options are discussed separately and are compared with power sharing via distribution lines in the following sections.

4.1.1 Wireless Power Transfer

Power can be shared through wireless power transfer. Nonetheless, this is limited to very short distances due to the high power losses associated with long wireless power transmission [70].

4.1.2 Traffic Offloading

The authors in [71] proposed to offload UEs at the cell edge of BSs with power deficit to neighboring BSs with power surplus. The authors in [72, 73] proposed to offload UEs from tiers with power deficit to tiers with power surplus, e.g., between macro BSs and small BSs, in a heterogeneous cellular network. The authors in [74–76] proposed to offload UEs from BSs with power deficit to BSs with power surplus by switching BSs with power deficit into a sleep mode. Nonetheless, traffic offloading causes a deterioration in the signal-to-interference-plus-noise ratio (SINR) of the offloaded UEs, whereas power sharing via distribution lines does not affect the SINR.

4.1.3 Smart Grid/ Main Grid Trading

The authors in [77,78] proposed to sell and buy power from the grid and use the grid to conduct virtual power transfer in addition to power sharing via distribution lines. Power sharing via distribution lines requires high capital expenditure for deploying physical distribution lines, whereas grid trading implies operational expenditure in the form of a price that has to be paid to the grid operator. To evaluate if the initial investment for deploying physical distribution lines is justified in the long-term or each BS should rather sell and buy its power from the grid, the local price structure has to be evaluated. BSs can buy power from the grid at a price p_b and sell it to the grid at a price p_s (feed-in tariff), where the grid operator typically requires that $p_b > p_s$ [79]. The difference in price, denoted by Δ_p , is as follows: $\Delta_p = p_b - p_s$ [80]. If Δ_p is great, it is more cost-efficient to share power via distribution lines. If Δ_p is small, it is more cost-efficient to sell and buy power from the grid. Even if Δ_p is small, cellular network operators may prefer to rely on their own local power sharing infrastructure to avoid reliance on the grid and to avoid the risk of future power price changes beyond their control. In general, power sharing via distribution lines is usually cost-efficient in dense cellular networks with small to medium inter-site distances, where the power losses in the distribution lines are low, expensive step-up and step-down transformers are not needed, and direct current (DC) to alternating current (AC) conversion losses are negligible or DC distribution lines are deployed between DC energy harvesters, such as PV cells. In contrast, sparse cellular networks with long inter-site distances are not suitable for power sharing via distribution lines due to the high power losses in the distribution lines, the high capital expenditures, and the right-of-way clearances needed for the transmission corridors. In the latter case, power will be more likely bought and sold to the grid.

4.1.4 Batteries

Since batteries are expensive and have a short lifetime (3 - 9 years), battery replacements significantly contribute to the system lifetime cost [61]. Employing both, distribution lines for power sharing and batteries to balance the mismatch between the power generation and consumption at the BSs, would greatly increase the capital expenditures. Hence, only distribution lines are considered in the system model of Chapter 4 to reduce the capital expenditures. Nonetheless, if batteries are deployed as well, efficient power sharing algorithm can reduce the required battery capacities, as seen in [81].

4.2 Literature Review: Benefits of Anti-correlated Energy Generation

BSs powered by renewable energy face the problem of temporal variations in the energy supply. These variations have to be managed properly to make efficient use of the harvested renewable energy. Energy harvesters with anti-correlated energy generation can mitigate the temporal variations in the energy supply. Thus, the energy deficit in one profile can be compensated by an energy surplus of another profile. For instance, 80% of energy was saved in [82] between a pair of energy-sharing BSs with anti-correlated sinusoidal energy profiles.

Instead of relying on only one energy source with one only characteristic energy generation profile, it is recommended to rely on a mix of different energy sources with anti-correlated energy generation profiles. The benefits of relying on a mix of different energy sources have been comprehensively studied in smart grids and conventional power grids [83–86]. Relying on a mix of different renewable energy sources to power cellular networks has been mainly studied in literature by combining wind energy and solar energy [13, 14]. The anti-correlation between solar

and wind energy generation profiles is justified on a daily timescale by the fact that high pressure (low pressure) areas tend to be sunny (cloudy) with low (high) surface wind, and on a seasonal timescale by the fact that solar (wind) energy is higher in summer (winter) than in winter (summer) for many locations [14].

It is especially promising to connect nearby BSs with power distribution lines [1,4,87] and to deploy energy harvesters with anti-correlated energy generation profiles at nearby BSs that are connected by power distribution lines. As a result, power can be transmitted from surplus BSs to deficit BSs via short distribution lines and the distance-dependent power losses in the distribution lines are small. Most papers in the literature do not consider the distance-dependent power loss in the distribution lines. For example, [88] introduced an energy hub for power sharing in cellular networks but assumed that the resistive power loss in the distribution lines is independent of the power propagation distance.

On the one hand, the greater the distance between two PV cells, the more anti-correlated are their energy generation profiles and the more power can be transmitted from the surplus BS to the deficit BS [89,90]. On the other hand, the greater the distance between two PV cells, the more power is lost in the distribution line.

4.3 Proof of Concept

To demonstrate the concept of energy harvesters with anti-correlated energy generation profiles, a southeast-orientated PV cell (energy harvester type 0) and a southwest-orientated PV cell (energy harvester type 1) in Greenwich (London, UK) in June are used as an example. Southeast-, and southwest-orientated PV cells have an orientation angle of -45° , and 45° with respect to the southern direction, respectively (cf. Figure 1.1). While energy harvester type 0 has a high power generation during time step 1 (potential surplus), energy harvester type 1 suffers from a low power generation (potential deficit), as seen in Figure 4.1. Vice versa in time

step 2, while energy harvester type 0 has a low power generation (potential deficit), energy harvester type 1 has a high power generation (potential surplus). Each BS is deployed with one of the two energy harvester types and all BSs have the same constant energy consumption profile for simplicity in this example, as seen in Figure 4.1. To make efficient use of the renewable power, power should be transmitted via distribution lines from BSs equipped with energy harvester type 0 to BSs equipped with energy harvester type 1 in time step 1. Vice versa in time step 2, power should be transmitted via distribution lines from BSs equipped with energy harvester type 1 to BSs equipped with energy harvester type 0.

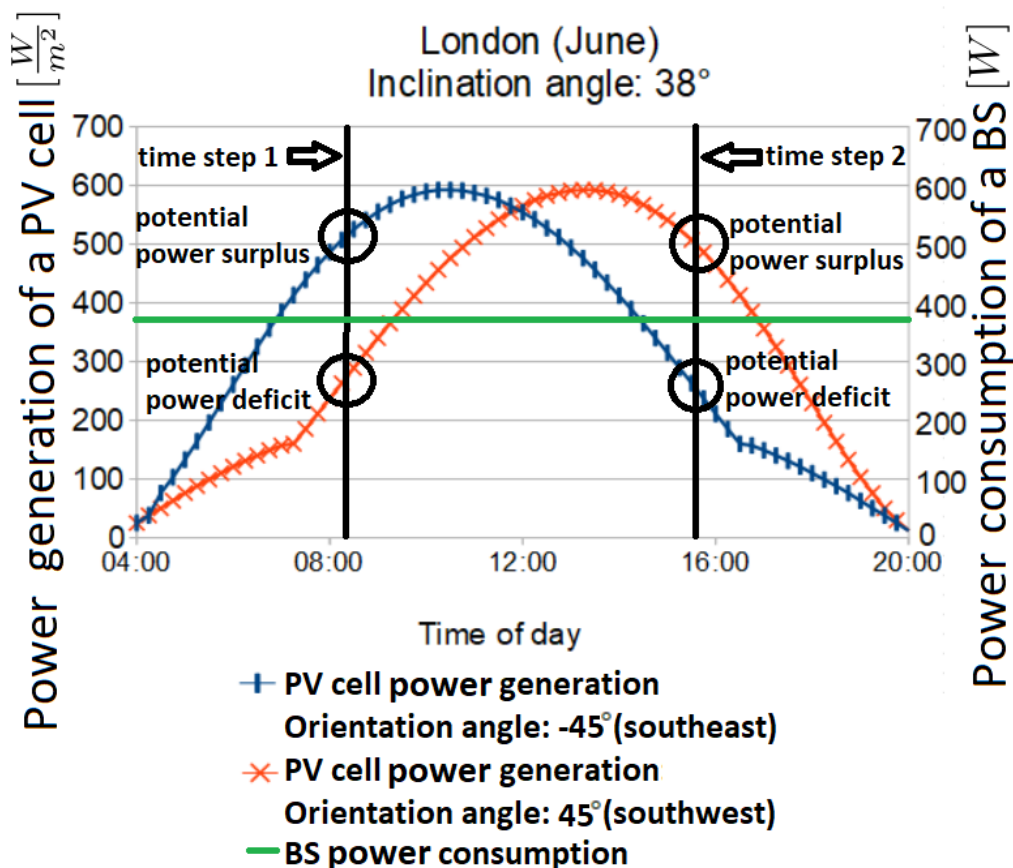


Figure 4.1: A southeast-orientated PV cell and a southwest-orientated PV cell in Greenwich (London, UK) in June are used to demonstrate the concept of energy harvesters with anti-correlated energy generation profiles. The historical average time series data of the PV cells were derived from PVGIS [10].

4.4 Contributions of Chapter 4

The contributions of Chapter 4 are summarized as follows:

- Developing an optimization algorithm that can be run once during the cellular network planning to determine what type of energy harvesters should be deployed to every BS in a cellular network. There are two different types of energy harvesters available for deployment which have anti-correlated energy generation profiles.
- Taking into account the topology of the cellular network as well as the distance-dependent power loss in the distribution lines during the optimization.
- Developing an optimization objective that maximizes the power that can be transmitted from surplus BSs to deficit BSs in the cellular network.
- Comparing the proposed optimization algorithm with randomly deploying anti-correlated energy harvesters to the BSs. The effects of different numbers of BSs, different distribution line existence probabilities, different distribution line power loss coefficients, and different power surplus values are investigated.

4.5 System Model 3 - Deployment of Anti-correlated Energy Harvesters to Every BS in a Cellular Network

There are $B \in \mathbb{N}$ uniformly distributed BSs in a square area of l^2 square meters, $l \in \mathbb{N}$, which are denoted by BS_i , $i \in \{1, \dots, B\}$ (cf. Figure 4.2). The parameter $c_i \in \{0, 1\}$ denotes if BS_i is equipped with the energy harvesting device type 0 or the energy harvesting device type 1, e.g., either with a solar cell or a wind turbine. A BS_i with energy harvesting device type 0, i.e., $c_i = 0$, belongs to cluster 0 and is

depicted with a black node in Figure 4.3. A BS_i with energy harvesting device type 1, i.e., $c_i = 1$, belongs to cluster 1 and is depicted with a red node in Figure 4.3.

The BS clustering optimization algorithm will be run once during the cellular network planning to determine for every BS its cluster and the corresponding energy harvesting device type.

4.5.1 Power Surplus/Deficit Values

The difference between the power generation and consumption of BS_i is denoted by the power surplus/deficit value $p_i^t[W]$ in watts for time step $t \in \{1, 2\}$. A surplus in power, and a deficit in power at BS_i are indicated by a positive value p_i^t , and a negative value p_i^t , respectively. The power surplus/deficit values of BSs in the same cluster at a given time step are similar because they are equipped with the same energy harvesting device type and have a similar BS load. As a result, all BSs in the same cluster are assumed to have the same power surplus/deficit value at a given time step.

The energy generation profile of BSs in cluster 0 is anti-correlated to the energy generation profile of BSs in cluster 1. In other words, BSs of cluster 0, and cluster 1 have a power surplus of $b_0 \in \mathbb{R}^+$, and a power deficit of $b_1 \in \mathbb{R}^-$ in time step 1, respectively. Vice versa in time step 2, BSs of cluster 0, and cluster 1 have a power deficit of b_1 , and a power surplus of b_0 , respectively. The power surplus/deficit values p_i^{t1} are summarized as follows:

¹It is assumed that every BS has a similar total daily energy consumption. Therefore, the energy harvesting device types should have similar capacities. The capacity of an energy harvesting device should not be oversized or undersized for powering one BS, that means it can be assumed that every BS will experience power surpluses and power deficits throughout the day. The time during a day where energy harvesting device 0 produces more power than the energy harvesting device 1 is represented by time step 1, whereas the time during a day where energy harvesting device 1 produces more power than the energy harvesting device 0 is represented by time step 2. Hence, it is justified to use only two time steps $t \in \{1, 2\}$ in the system model 3 to represent a 24-hour day. Because the optimization is done only once in a BS's lifetime, p_i^t represents the average daily power surplus/deficit value at the BS throughout the lifetime of the BS. Thus, it can be assumed that throughout the lifetimes of the BSs, the power surplus/deficit values at the BSs in the same cluster at a given time step are the same because they are equipped with the same energy harvesting

$$p_i^t = \begin{cases} b_0 & c_i = 0 \text{ and } t = 1 \\ b_1 & c_i = 1 \text{ and } t = 1 \\ b_1 & c_i = 0 \text{ and } t = 2 \\ b_0 & c_i = 1 \text{ and } t = 2. \end{cases} \quad (4.1)$$

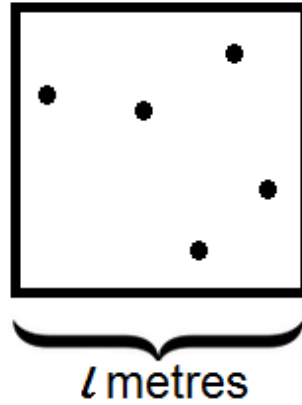


Figure 4.2: Illustration of the considered cellular network with $B = 5$ BSs uniformly distributed in a square area of l^2 square meters.

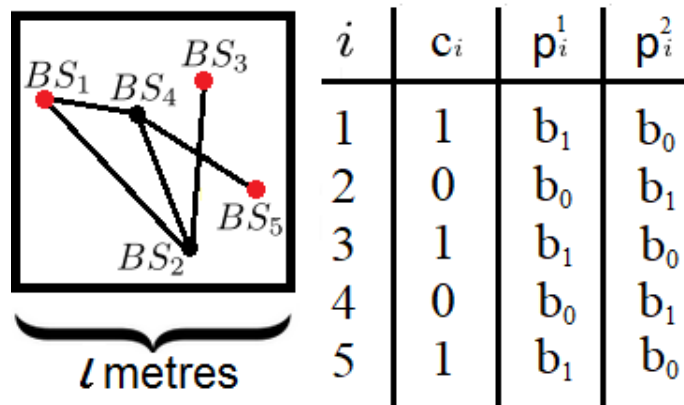


Figure 4.3: The graph representation of the cellular network with example BS cluster allocation values c_i , surplus/deficit power values p_i^1 in time step 1 and surplus/deficit power values p_i^2 in time step 2 given for the BSs.

device type and have a similar BS load. Because the energy harvesting device types have similar capacities, it can be assumed that $p_0^1 = p_1^2 = b_0$ and $p_1^1 = p_0^2 = b_1$.

4.5.2 Distance-dependent Power Loss in the Distribution Lines

The normalized Euclidean distance $d((i, j))$ between BS_i and BS_j with respect to l meters is as follows:

$$d((i, j)) = \frac{\|BS_i - BS_j\|}{l}, \quad (4.2)$$

where $\|BS_i - BS_j\|$ [m] in meters is the Euclidean distance between BS_i and BS_j , and l [m] in meters is the side length of the square in Figure 4.3.

Power can be transmitted from a surplus BS in one cluster to a deficit BS in the other cluster at each time step if the two BSs are connected by a distribution line. The power flow in the distribution line is subject to power loss due to resistive heating. The power loss $P_{\text{loss}}((i, j))$ [W] in watts in the distribution line from BS_i to BS_j can be calculated by Ohm's law and the formula for the distribution line resistance [91] as follows:

$$P_{\text{loss}}((i, j)) = I_{\text{ele}}^2 \cdot \rho \cdot \frac{l \cdot d((i, j))}{A_c} = I_{\text{ele}}^2 \cdot C \cdot d((i, j)), \quad (4.3)$$

where I_{ele} [A] in amperes is the electric current traveling through the distribution line, ρ [Ωm] in ohm-meters is the resistivity of the distribution line, l [m] in meters is the side length of the square in Figure 4.3, $d((i, j))$ is defined in (4.2), A_c [m^2] in square meters is the cross-sectional area of the distribution line, and C [Ω] in ohms is the power loss coefficient per l meters of distribution line, i.e., $C = \frac{\rho \cdot l}{A_c}$.

4.5.3 Topology of the Cellular Network

The topology of the cellular network is represented by a graph (cf. Figure 4.3), where V is the set of vertices which denotes the BSs, and E is the set of directed

edges which denotes the distribution lines as follows:

$$\begin{aligned}
 V &= \{1, 2, \dots, B\}, \\
 E &= \{(i, j), (j, i) \mid i \in V, j \in V, BS_i \text{ and } BS_j \text{ are} \\
 &\quad \text{connected by a distribution line}\},
 \end{aligned} \tag{4.4}$$

where (i, j) denotes the directed edge from BS_i to BS_j .

The power flow on the edge (i, j) is denoted by $f^t((i, j))$ in time step $t \in \{1, 2\}$.

All power values are normalized with respect to the constant value of $\max\{b_0, |b_1|\}$ as follows:

$$\begin{aligned}
 \hat{f}^t((i, j)) &= \frac{f^t((i, j))}{\max\{b_0, |b_1|\}} \\
 \hat{b}_0 &= \frac{b_0}{\max\{b_0, |b_1|\}} \\
 \hat{b}_1 &= \frac{b_1}{\max\{b_0, |b_1|\}}.
 \end{aligned} \tag{4.5}$$

The power values $\hat{f}^t((i, j))$, \hat{b}_0 , \hat{b}_1 are the normalized power values of $f^t((i, j))$, b_0 , b_1 , respectively.

4.5.4 Justification of Assumptions

The following two assumptions in the system model 3 are justified in this section.

- Assumption 1: The power flow is equivalent to the second power of the electric current flow in the distribution line.

The electric power P in the distribution line can be calculated as follows:

$$P = V_{\text{ele}} \cdot I_{\text{ele}}, \tag{4.6}$$

where V_{ele} is the electric potential, and I_{ele} is the electric current. The power loss $P_{\text{loss}}((i, j))$ in the distribution line is caused by the electric current and not the electric potential of the power, as seen in (4.3). Nonetheless, it is outside of the scope of this thesis to model the relationship between the power flow and the electric current flow in the distribution line. Hence, it is assumed for simplicity and in accordance with (4.6) that if the power increases/decreases in the distribution line, the electric current and the electric potential increase/decrease equally. In other words, a power flow in the distribution line of x watts is equivalent to a flow of $I_{\text{ele}} = \sqrt{x}$ amperes and $V_{\text{ele}} = \sqrt{x}$ voltages in the system model 3. Hence, the parameter $f^t((i, j))[W/A^2]$ can be interpreted as the power flow on the edge (i, j) in watts or the second power of the current flow I_{ele}^2 on the edge (i, j) in square amperes.

- Assumption 2: $C \in [0, \frac{1}{\sqrt{2}}]$.

The maximum normalized distance $d((i, j))$ in a square is $\sqrt{2}$. If C were greater than $\frac{1}{\sqrt{2}}$, then $C \cdot d((i, j))$ could be greater than 1. That would imply that more power is lost in the distribution line than was sent through the distribution line.

4.6 Mixed-Integer Linear Programming Problem

The objective is to find the optimal BS cluster allocation values c_n for all $BS_n, n \in V$, i.e., deploying either an energy harvesting device type 0 or an energy harvesting device type 1 at every BS, so that the renewable power in the cellular network can be used most efficiently. c_n , $\hat{f}^1((i, j))$, and $\hat{f}^2((i, j))$ are the parameters to be determined for all $n \in V$ and $(i, j) \in E$. Because the parameters c_n are integers, whereas the power flow values $\hat{f}^t((i, j))$ are real numbers, a mixed-integer linear programming solver is needed for this problem.

The optimization objective is to maximize the total normalized renewable power M

received at the deficit BSs during the two time steps as follows:

$$M = \max_{\substack{c_n, \hat{f}^1((i,j)), \hat{f}^2((i,j)) \\ \forall n \in V, \forall (i,j) \in E}} \left\{ \underbrace{\sum_{(i,j) \in E} \hat{f}^1((i,j)) (1 - C \cdot d((i,j)))}_{\text{time step 1}} + \underbrace{\sum_{(i,j) \in E} \hat{f}^2((i,j)) (1 - C \cdot d((i,j)))}_{\text{time step 2}} \right\} \quad (4.7)$$

subject to

Lower bounds and upper bounds for the parameters to be determined:

$$\begin{aligned} 0 \leq c_n \leq 1, \quad c_n \in \mathbb{Z}, \quad \forall n \in V \\ 0 \leq \hat{f}^1((i,j)) \leq 1 \quad \forall (i,j) \in E \quad \left. \vphantom{\hat{f}^1} \right\} \text{time step 1} \\ 0 \leq \hat{f}^2((i,j)) \leq 1 \quad \forall (i,j) \in E \quad \left. \vphantom{\hat{f}^2} \right\} \text{time step 2} \end{aligned} \quad (4.8)$$

Power flow only on edges from surplus BSs to deficit BSs:

$$\begin{aligned} \hat{f}^1((i,j)) + c_i \leq 1 \quad \forall (i,j) \in E \\ \hat{f}^1((i,j)) - c_j \leq 0 \quad \forall (i,j) \in E \\ \hat{f}^2((i,j)) + c_j \leq 1 \quad \forall (i,j) \in E \\ \hat{f}^2((i,j)) - c_i \leq 0 \quad \forall (i,j) \in E \end{aligned} \quad \left. \vphantom{\hat{f}^1} \right\} \begin{array}{l} \text{time step 1} \\ \text{time step 2} \end{array} \quad (4.9)$$

Power flow out of the surplus BSs:

$$\begin{aligned}
& \left. \begin{aligned} \sum_{\substack{(i,j) \in E \\ j \in V}} \hat{f}^1((i,j)) \leq \hat{b}_0 \quad \forall i \in V \end{aligned} \right\} \text{time step 1} \\
& \left. \begin{aligned} \sum_{\substack{(i,j) \in E \\ j \in V}} \hat{f}^2((i,j)) \leq \hat{b}_0 \quad \forall i \in V \end{aligned} \right\} \text{time step 2}
\end{aligned} \tag{4.10}$$

Power flow into the deficit BSs:

$$\begin{aligned}
& \underbrace{\sum_{\substack{(i,j) \in E \\ i \in V}} \hat{f}^1((i,j)) (1 - C \cdot d((i,j))) \leq |\hat{b}_1| \quad \forall j \in V}_{\text{time step 1}} \\
& \underbrace{\sum_{\substack{(i,j) \in E \\ i \in V}} \hat{f}^2((i,j)) (1 - C \cdot d((i,j))) \leq |\hat{b}_1| \quad \forall j \in V}_{\text{time step 2}}
\end{aligned} \tag{4.11}$$

The optimization objective (4.7) adds the normalized power flows on all edges and subtracts the normalized power losses (cf. (4.3)) on all edges.

The inequalities (4.8) represent the lower bounds and the upper bounds for the parameters to be determined, i.e., for the parameters c_n , $\hat{f}^1((i,j))$ and $\hat{f}^2((i,j))$ for all $n \in V$ and $(i,j) \in E$. In addition, the inequalities (4.8) state that the parameters c_n are integers for all $n \in V$.

The inequalities (4.9) ensure that power only flows on edges from surplus BSs to deficit BSs. Power can only flow on an edge (i,j) in time step 1 if BS_i belongs to cluster 0, i.e., $c_i = 0$, and BS_j belongs to cluster 1, i.e., $c_j = 1$. $\hat{f}^1((i,j)) + c_i \leq 1$ implies that the power flow $\hat{f}^1((i,j))$ is 0 if c_i is not 0 and $\hat{f}^1((i,j)) - c_j \leq 0$ implies that the power flow $\hat{f}^1((i,j))$ is 0 if c_j is not 1 in time step 1. Vice versa in time step 2, power can only flow on an edge (i,j) if BS_i belongs to cluster 1, i.e., $c_i = 1$, and BS_j belongs to cluster 0, i.e., $c_j = 0$. $\hat{f}^2((i,j)) + c_j \leq 1$ implies that the power flow $\hat{f}^2((i,j))$ is 0 if c_j is not 0 and $\hat{f}^2((i,j)) - c_i \leq 0$ implies that the power flow

$\hat{f}^2((i, j))$ is 0 if c_i is not 1 in time step 2.

The inequalities (4.10) ensure that the normalized power flow out of a surplus BS is not greater than \hat{b}_0 . If $i \in V$ is a deficit BS in time step t , then $\sum_{\substack{(i,j) \in E \\ j \in V}} \hat{f}^t((i, j)) \leq \hat{b}_0$ is already fulfilled because all power flows out of the deficit BS_i are 0 due to the inequalities (4.9).

The inequalities (4.11) ensure that the normalized power flow into a deficit BS is not greater than $|\hat{b}_1|$. The power received at the deficit BSs is subject to power losses in the distribution lines. If $j \in V$ is a surplus BS in time step t , then $\sum_{\substack{(i,j) \in E \\ i \in V}} \hat{f}^t((i, j))(1 - C \cdot d((i, j))) \leq |\hat{b}_1|$ is already fulfilled because all power flows into the surplus BS_j are 0 due to the inequalities (4.9).

4.7 Numerical Results

The `intlinprog(f, intcon, A, b)` function implemented in MATLAB is used to solve the mixed-integer linear programming problem (MILPP) defined in (4.7) - (4.11). Unless otherwise stated, the values² from Table 4.1 are used for the parameters to evaluate the performance of the proposed MILPP.

1000 random graphs are generated to determine the average normalized renewable power M received at the deficit BSs during the two time steps. The random graphs are generated by placing the B BSs uniformly in the square and connecting any two BSs with a probability of $q \in [0, 1]$ with a distribution line.

Table 4.1:
Input parameters of system model 3

Parameter	Description	Value
$B \in \mathbb{N}$	Number of BSs	8
$q \in [0, 1]$	Distribution line existence probability	0.3

²Without loss of generality, b_0 is set at 1 and b_1 is set at -1 because the energy harvesting device types should have similar capacities and all power values will be normalized in (4.5) anyway.

$C \in [0, \frac{1}{\sqrt{2}}]$	Power loss coefficient per l meters of distribution line	0.6
$b_0 \in \mathbb{R}^+$	Power surplus value	1
$b_1 \in \mathbb{R}^-$	Power deficit value	-1

The performance of the proposed MILPP is investigated in comparison with randomly allocating BSs into clusters, i.e., without considering the topology of the cellular network or the power losses in the distribution lines by setting the cluster allocation values c_i at 0, and 1 with a probability of 50%, and 50%, respectively. In other words, $\mathbb{P}(c_i = 0) = \mathbb{P}(c_i = 1) = 0.5 \quad \forall i$ for the random cluster allocation.

Figure 4.4 shows the performance of the proposed MILPP and of random BS cluster allocation for different numbers of BSs B . The performance gap between the two BS cluster allocations increases with the number of BSs. This is because a denser cellular network offers more opportunities for BS clustering optimization, and hence the superiority of the MILPP over the random BS cluster allocation increases with the cellular network density.

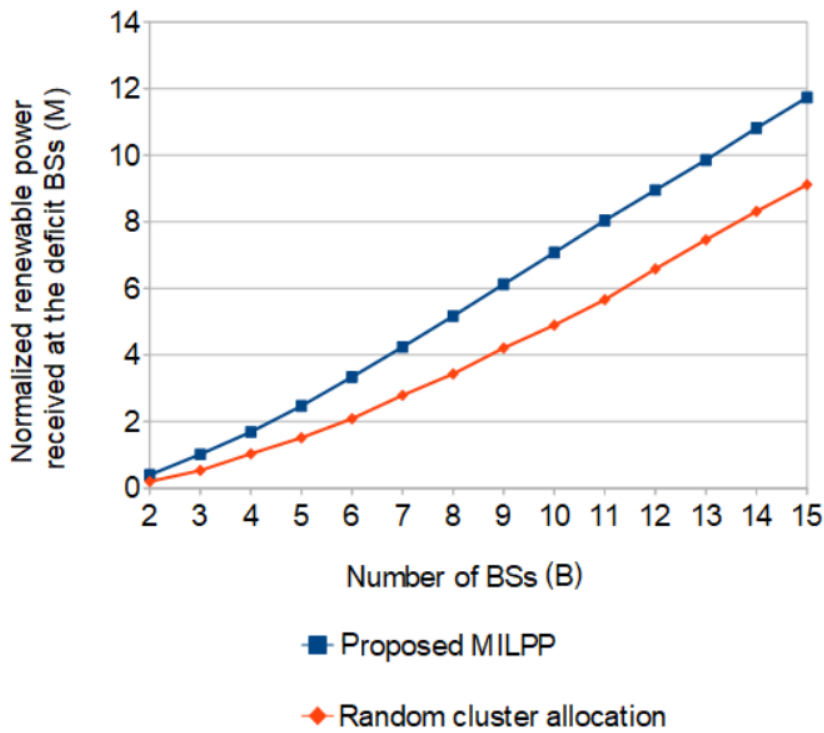


Figure 4.4: Average normalized renewable power received at the deficit BSs M of the proposed MILPP and of random BS cluster allocation vs. number of BSs B .

Figure 4.5 shows the performance of the proposed MILPP and of random BS cluster allocation for different distribution line existence probabilities q . The performance gap between the two BS cluster allocations increases with the distribution line existence probability in the range of 0 to 0.3, whereas it is nearly constant in the range of 0.3 to 1.

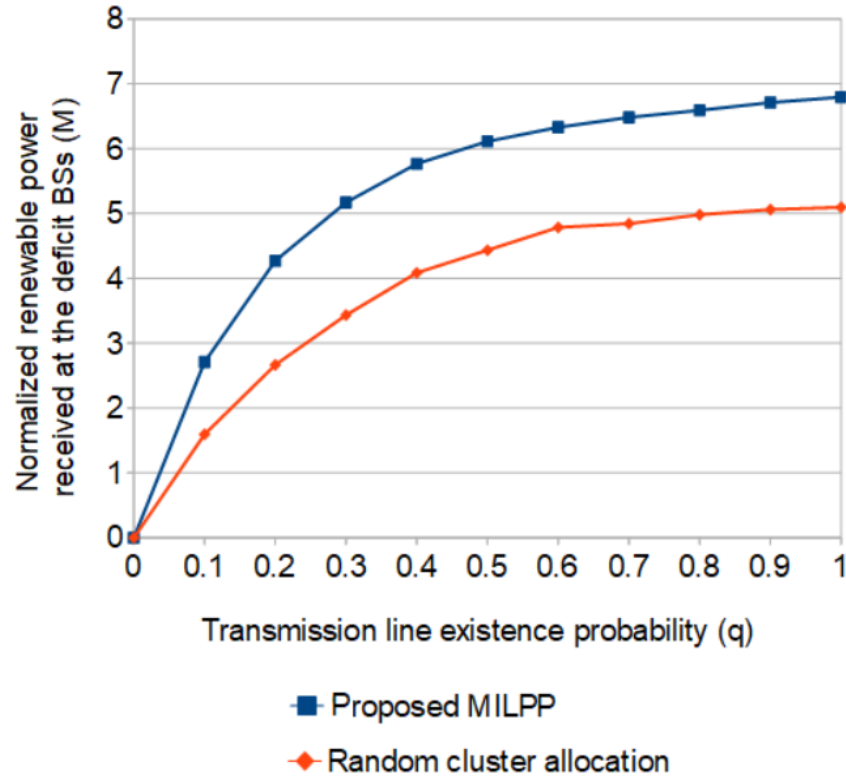


Figure 4.5: Average normalized renewable power received at the deficit BSs M of the proposed MILPP and of random BS cluster allocation vs. distribution line existence probability q .

Figure 4.6 shows the performance of the proposed MILPP and of random BS cluster allocation for different power loss coefficients per l meters of distribution line C^3 . The performance gap between the two BS cluster allocations decreases slightly with the power loss coefficient per l meters of distribution line.

³The normalized Euclidean distance $d((i,j)) = \frac{\|BS_i - BS_j\|}{l}$ is used in all formulas, derived parameters and the proposed MILPP. Hence, the results in Figure 4.6 do not change with different values of l , only the scale of the x-axis changes. If the BSs are deployed in an area of, e.g., 1000 m x 1000 m, Figure 4.6 should be read with the x-axis label “Power loss coefficient per 1000 meters.”

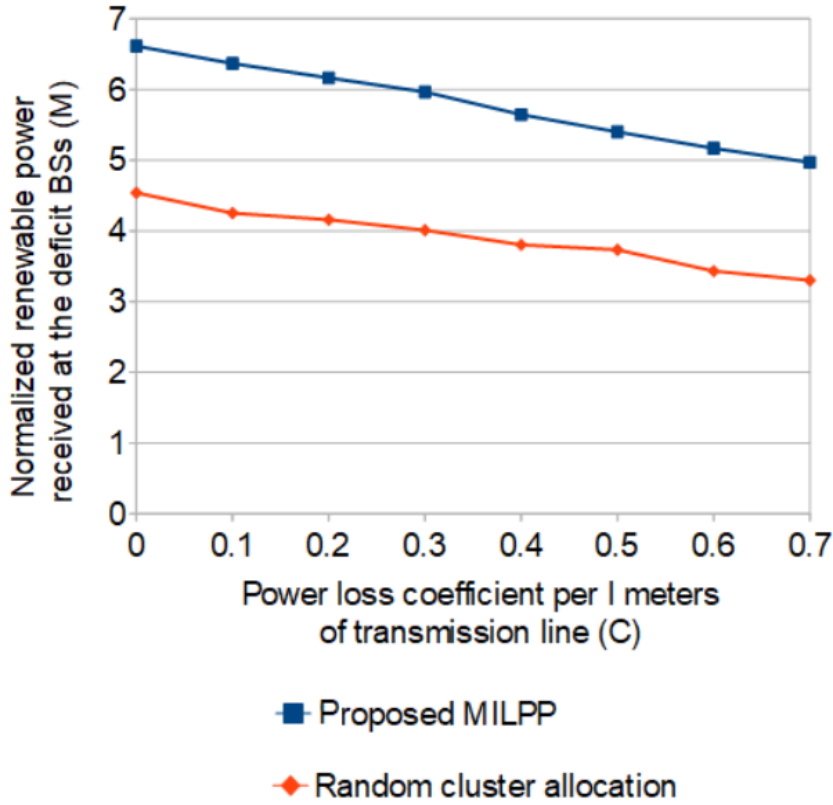


Figure 4.6: Average normalized renewable power received at the deficit BSs M of the proposed MILPP and of random BS cluster allocation vs. power loss coefficient per l meters of distribution line C .

Figure 4.7 shows the performance of the proposed MILPP and of random BS cluster allocation for different power surplus values b_0 . b_1 was fixed to -1 . The performance gap between the two BS cluster allocations increases with the power surplus value in the range of 0 to 1, whereas it decreases in the range of 1 to 2. This is because the power was normalized with respect to $\max\{b_0, |b_1|\}$. If $b_0 \neq 1$, either \hat{b}_0 or $|\hat{b}_1|$ is smaller than 1 because a mismatch exists between the power surplus value and the power deficit value. Only if $b_0 = 1$, \hat{b}_0 and $|\hat{b}_1|$ are both 1 because the power surplus value and the power deficit value have the same absolute value.

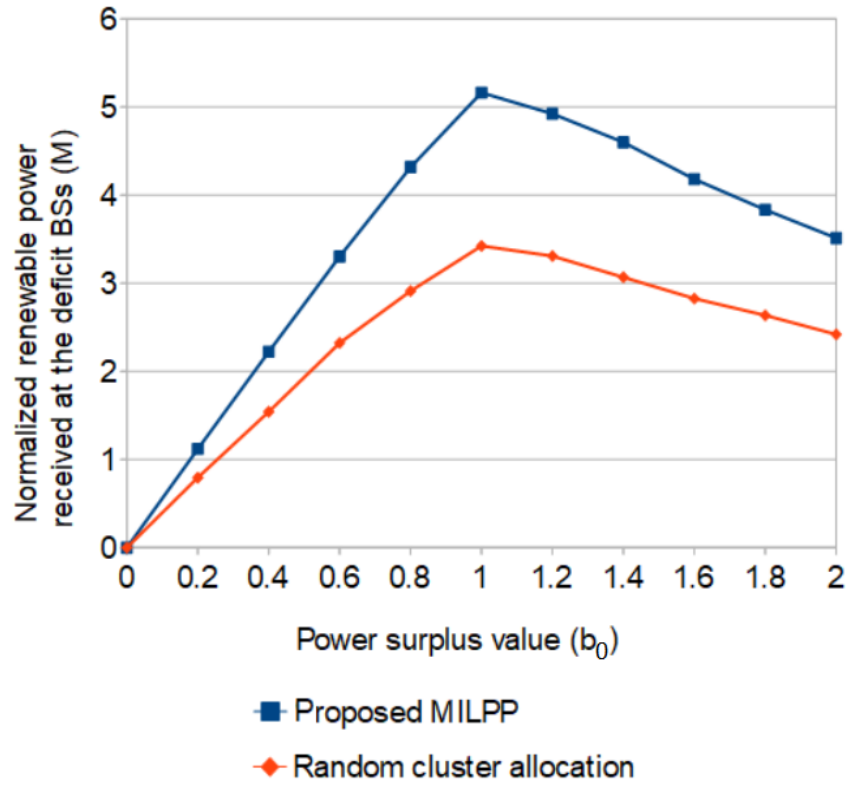


Figure 4.7: Average normalized renewable power received at the deficit BSs M of the proposed MILPP and of random BS cluster allocation vs. power surplus value b_0 . b_1 was fixed to -1 .

Figures 4.4 - 4.7 show that the proposed MILPP always outperforms the random BS cluster allocation because the MILPP considers the topology of the cellular network and the power losses in the distribution lines. Because the proposed MILPP takes into account the topology of the cellular network, it increases the probability that a BS is deployed with an energy harvester type that is anti-correlated to those deployed at its connected neighboring BSs. In addition, the shorter the distribution line between a pair of BSs, the more likely that these two BSs are deployed with anti-correlated energy harvesters, because the proposed MILPP takes into account the distance-dependent power loss in the distribution lines. The MILPP has an average system performance improvement of around 40% in comparison with the random BS cluster allocation.

4.8 Summary of Chapter 4

In Chapter 4, the system model was extended to a multi-cell cellular network. The system model consisted of several BSs that were distributed in an area and some of them were connected by distribution lines to share the renewable energy among them. There were two different types of energy harvesters, which have anti-correlated energy generation profiles, available for deployment in the system model. Two PV cells that have significantly different orientation angles, such as east-oriented and west-oriented PV cells, are an example for energy harvesters with anti-correlated energy generation profiles. A mixed-integer linear programming problem (MILPP) was developed to determine what type of energy harvester should be deployed to every BS to share the renewable power most efficiently in the cellular network. The MILPP can be run once during the cellular network planning and it maximizes the power that can be transmitted from surplus BSs to deficit BSs in the cellular network. The algorithm takes into account the topology of the cellular network, i.e., whether or not a distribution line exists between a pair of BSs. Hence, the proposed algorithm increases the probability that a BS is deployed with an energy harvester type that is anti-correlated to those deployed at its connected neighboring BSs. In addition, the shorter the distribution line between a pair of BSs, the more likely that these two BSs are deployed with anti-correlated energy harvesters, because the proposed algorithm takes into account the distance-dependent power loss in the distribution lines. The renewable power that can be transmitted from the surplus BSs to the deficit BSs in the cellular network is on average around 40% higher with the proposed MILPP in comparison with randomly deploying anti-correlated energy harvesters to the BSs.

Chapter 5

Conclusion and Future Work

5.1 Summary of Thesis Achievements

Chapter 2 focused on matching the energy generation profile of PV cells with the energy consumption profile of a BS in time. The orientation angles of N PV cells powering one BS were jointly optimized to improve the match between the two profiles. The proposed optimization algorithm only needs to be run a single time offline and the obtained optimal angles can be used for all solar-powered BSs with similar geographic locations and energy consumption profiles. The energy generation profile of any randomly inclined and oriented PV cell were analytically derived from the irradiance values received at a horizontally-mounted PV cell at the same location. The thesis identified and discussed analytically to what extent the orientation angle θ shifts the energy generation profile away from noon if the PV cells are not south-oriented ($\theta^* = 0^\circ$). The energy drawn per day from the main grid by the BS given its energy consumption profile was used as the performance metric to determine the optimal set of orientation angles. To evaluate the effectiveness of the proposed orientation angle optimization, three different types of BS energy consumption profiles were investigated: constant traffic load profiles, business-area traffic load profiles, and residential-area traffic load profiles.

The main results are that the system performance ($\Delta_1 > 0$) can be increased significantly by deploying one PV cell with optimal orientation angle θ_1^* (or several PV cells with the same orientation angle θ_1^*) if the energy generation of the PV cell is slightly smaller ($G < C$), is slightly greater ($G > C$), or is significantly greater ($G \gg C$) than the energy consumption of the BS. This is caused by the ability to shift the energy generation peak from noon towards the most significant local maximum between sunrise and sunset of the energy consumption profile. Furthermore, the system performance ($\Delta_2 > 0$) can be further increased by deploying two PV cells with jointly optimized orientation angles θ_1^* and θ_2^* (or several PV cells where half of them are deployed with θ_1^* and the other half with θ_2^*) if a constant energy consumption profile or a consumption profile with significant local maxima in the morning as well as in the afternoon are given. This is caused by the ability to shift the energy generation peak from noon towards the morning with east-oriented PV cells, while the other west-oriented PV cells shift the energy generation peak towards the afternoon in the northern hemisphere. Because there are only two directions (morning and afternoon) that the energy can be shifted to, the system performance can not be further increased significantly by deploying more than 2 differently oriented PV cells. More than 2 differently oriented PV cells may even deteriorate the system performance ($\Delta_3 < 0$) in some scenarios.

Chapter 3 added a battery model to the system model. The battery model is based on a Markov chain. The PV cell's orientation angle optimization algorithm with Markov chain based battery model has a running time dependent on the squared number of energy states of the battery S_{\max} and the time resolution T . The number of UEs served by the BS throughout the day $\overline{S_{\text{UE}}}(\theta)$ was used as the performance metric to identify the optimal orientation angle. The accuracy of the proposed algorithm was verified by showing that simulation trials converge based on the law of large numbers to the output $\overline{S_{\text{UE}}}(\theta)$ of the proposed algorithm. The effects of different battery capacities on the optimal PV cell orientation angle were investigated. Whereas BSs with small battery capacities significantly improved their performance

by orientation angle optimization, BSs with large battery capacities should orient the PV cells towards the south. The importance of the PV cell orientation angle optimization was verified for a BS with small battery capacity ($b_{\max} = 1$) located in a business-area in Greenwich (London, UK) in summer. Also PV cells are normally orientated to the south in Greenwich (London, UK), the proposed algorithm revealed that the optimal orientation angle is between 25° to 40° to the west.

In the last chapter, the system model was extended to a multi-cell cellular network. The system model consisted of several BSs that were distributed in an area and some of them were connected by distribution lines to share the renewable energy among them. There were two different types of energy harvesters, which have anti-correlated energy generation profiles, available for deployment in the system model. Two PV cells that have significantly different orientation angles, such as east-oriented and west-oriented PV cells, are an example for energy harvesters with anti-correlated energy generation profiles. If energy harvesters with anti-correlated energy generation profiles are deployed at BSs that are connected by distribution lines, the power can be transmitted from surplus BSs to deficit BSs via the distribution lines. A mixed-integer linear programming problem (MILPP) was developed to determine how energy harvesters with anti-correlated energy generation profiles should be deployed to every BS to share the renewable power most efficiently in the cellular network. The MILPP can be run once during the cellular network planning. The MILPP takes into account the topology of the cellular network, i.e., whether or not a distribution line exists between a pair of BSs. Hence, the proposed algorithm increases the probability that a BS is deployed with an energy harvester type that is anti-correlated to those deployed at its connected neighboring BSs. In addition, the shorter the distribution line between a pair of BSs, the more likely that these two BSs are deployed with anti-correlated energy harvesters, because the proposed algorithm takes into account the distance-dependent power loss in the distribution lines. The renewable power that can be transmitted from the surplus BSs to the deficit BSs in the cellular network was on average around 40% higher with the proposed op-

timization algorithm in comparison with randomly deploying anti-correlated energy harvesters to the BSs.

5.2 Future Work and Applications

In the age of internet, online tools, and publicly available data, future applications and optimization tools on basis of this thesis are likely to be implemented. There are already an increasing amount of geographic information systems (GISs) online available, which provide PV cell performance guides for various geographical areas free of charge, such as for the USA [30], for Europe [10], and worldwide [31,32]. An online tool for PV cell orientation angle optimization can be easily implemented on basis of this thesis. Such an online tool would greatly increase the impact of this thesis and will be beneficial for mankind and the environment. For that purpose, the source code of Chapter 2 is given in the Appendix B of this thesis and is publicly available on GitHub [56].

This thesis derived the optimization methods necessary to optimize PV cells' orientation angles and their deployment at BSs for many different scenarios. For that purpose, the methods presented in this thesis are kept general and normalized energy generation values and normalized energy consumption values are used. The advantage of generalization and normalization is that the derived optimization methods presented in this thesis can be applied to nearly any scenario in the real world. If the input parameters for a specific scenario in the real world, such as PV cell types, energy profiles, and cellular network topology, are given, the optimal orientation angles and deployment strategy can be derived with the methods presented in this thesis. The disadvantage of generalization and normalization is that the thesis did not focus on deriving a comprehensive practical worldwide guide for a specific input parameter set. Future extension to this work can be done by evaluation typical specific input parameter sets and deriving for each set a comprehensive practical

worldwide guide. In addition, if the specific input parameter set is derived from a real world system, future work can be done by evaluating the performance of the real world system deployed with the optimal PV cells' orientation angles and deployment strategy.

An interesting future extension is to increase the optimization horizon to an entire year. Optimizing the inclination angle of a PV cell is done on a yearly timescale. As a result, it is a method to shift the energy generation peak from a surplus season (e.g. summer) to a deficit season (e.g. winter). In contrast, optimizing the PV cell orientation angle is done on a daily timescale. As a result, it is a method to shift the energy generation peak from a surplus time (e.g. noon) to a deficit time (e.g. morning or afternoon). Nonetheless, most geographical locations have different seasonal energy generation profiles. Hence, the optimal PV cells' orientation angles and deployment strategies are different in different seasons. Our derived optimization method can be applied to several days distributed throughout the year (e.g. one day in winter, one day in spring, one day in summer, and one day in autumn) and the average derived PV cells' orientation angles and deployment strategy can be used for deployment. In spite of that strategy, many locations in the northern hemisphere might emphasize on improving the performance of the system during the winter season since this is usually the most energy sparse season. A higher weight can be given on the optimal PV cells' orientation angles and deployment strategy in winter compared with the other seasons. Increasing the optimization horizon to an entire year and weighting the different seasons are an interesting extension to this thesis.

Furthermore, future work can jointly optimize the orientation and inclination angles of PV cells.

Some of the models in this thesis can be extended to model the real world more accurately in the future. For example, the battery model could include input/output efficiency coefficients since there is always a leakage when charging/discharging a

battery. Another example, since the energy needed to serve one UE at the BS during one time step varies considerably dependent on the UEs distance to the BS, the requested service, and priority or interference issues with other UEs, the average amount of energy needed to serve an UE could be modeled more realistically in future extensions of this work.

Appendix A

Normalization Example

A practical example will be used in this appendix to show step by step the process of normalization and the derived recommendations for the orientation angles optimization from Chapter 2.

An area of 5m^2 is given for PV cell deployment in Greenwich. There are N PV cells to deploy. The energy conversion efficiency of all PV cells η is set at 0.2 and the inclination angle of all PV cells γ is set at 36° (optimal inclination angle for Greenwich (London, UK) in summer). The time step duration τ is set at $15\text{min} = 15 \cdot 60\text{s} = 900\text{s}$ and the total number of time steps T is set at 96. We assume that the BS is located near a school. Hence, the energy consumption $C^{\text{original}}(t)$ of the BS is $600000\text{J}=0.6\text{MJ}$ per 15 minutes during school hours, i.e., 8am-1pm ($t \in \{32, \dots, 52\}$), and $300000\text{J}=0.3\text{MJ}$ per 15 minutes during the rest of the day, i.e., $t \in \{1, \dots, 31\}$ or $t \in \{53, \dots, 96\}$.

Among all orientation angle settings and among all time steps throughout the day, the peak energy generation occurs during noon when all PV cells are south-oriented in Greenwich. This is because Greenwich is located on the reference meridian of its time zone. This peak energy generation value PEG is used to normalize the energy generation profiles of the PV cells as well as the energy consumption profile of the BS for convenience. This has the convenient effect that the normalized peak energy generation is exactly 1 unit of normalized energy as seen in Figure 2. The time step $t = \frac{T}{2}$ is noon. The peak energy generation value of all PV cells (south-oriented) at noon in this example is 552600J as follows:

$$PEG = G_{0^\circ,1}^{\text{original}}\left(\frac{T}{2}\right) = \sum_{n=1}^N G_{0^\circ,N}^{\text{original}}\left(\frac{T}{2}\right) = \sum_{n=1}^N I_{0^\circ_n}\left(\frac{T}{2}\right) \cdot \eta \cdot \frac{A}{N} \cdot \tau = \quad (1)$$

$$\sum_{n=1}^N 614 \cdot 0.2 \cdot \frac{5}{N} \cdot 900 = 614 \cdot 0.2 \cdot 5 \cdot 900 = 552600. \quad (2)$$

$614 \frac{\text{W}}{\text{m}^2}$ is obtained from the PVGIS database as seen in Figure 1.

```

Latitude:      51°28'36" North,
Longitude:     0°0'1" West

Results for:   June

Inclination of plane:  36    deg.
Orientation (azimuth) of plane:  0    deg.
Time           G
•             •
•             •
•             •
11:52         614
12:07         614
•             •
•             •
•             •
G: Global irradiance on a fixed plane (W/m2)
PVGIS (c) European Communities, 2001-2012

```

Figure 1: PVGIS data sheet from [10]. γ is set at 36° , θ is set at 0° , month is set at June, and the location is Greenwich ($lat = 51.4767^\circ$ North, $lon = 0.0003^\circ$ West).

Hence, $G_{\theta,N}(t)$ is the normalized energy generated by one PV cell (out of the N PV cells) installed with orientation angle θ at time step t and can be calculated by

$$G_{\theta,N}(t) = \frac{G_{\theta,N}^{\text{original}}(t)}{G_{0^\circ,1}^{\text{original}}\left(\frac{T}{2}\right)} = \frac{G_{\theta,N}^{\text{original}}(t)}{552600} = \frac{I_\theta(t)}{I_{0^\circ}\left(\frac{T}{2}\right) \cdot N} = \frac{I_\theta(t)}{614 \cdot N}. \quad (3)$$

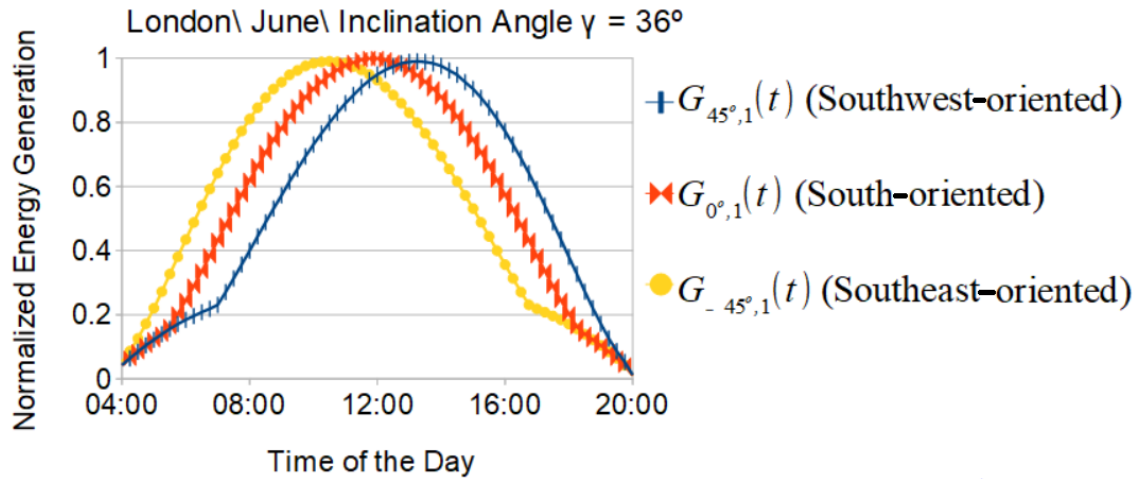


Figure 2: Normalized energy generation profiles of a southeast-oriented, south-oriented, and southwest-oriented PV cell. Each of the PV cells is covering the total surface area $A = 5\text{m}^2$. The south-oriented PV cell generates at noon the most energy among all orientation angle settings and among all time steps throughout the day. This normalized peak energy generation is exactly 1 unit of normalized energy.

Hence, $C(t)$ is the normalized energy consumption by the BS at time step t and can be calculated by

$$C(t) = \frac{C^{\text{original}}(t)}{G_{0^\circ,1}^{\text{original}}\left(\frac{T}{2}\right)} = \frac{C^{\text{original}}(t)}{552600}. \quad (4)$$

I want to point out, that the energy generation profiles as well as the energy consumption profile are normalized by the same value 552600J . But because the irradiance $I_\theta(t)$ value was calculated in Chapter 2, the irradiance $I_\theta(t)$ has to be normalized by $614\frac{\text{W}}{\text{m}^2} \cdot N$ to achieve the same normalization, cf. (3)-(4).

I want to point out, that the energy generation profiles as well as the energy consumption profile are normalized by the same value 552600J . This is because I want to keep the same relationship between the two types of profiles after the normalization. That means if the energy consumption at time step t is double the amount of the energy generated by the PV cells at time step t before the normalization, the same should be true after the normalization, i.e., the normalized energy consumption at time step t is double the amount of the normalized energy generated by the PV cells at time step t . This can be proven mathematically by

$$\frac{C(t)}{G_{\theta,N}(t)} = \frac{\frac{C^{\text{original}}(t)}{552600}}{\frac{G_{\theta,N}^{\text{original}}(t)}{552600}} = \frac{C^{\text{original}}(t)}{G_{\theta,N}^{\text{original}}(t)}. \quad (5)$$

Figure 3, and Figure 4 show the energy generation profile of one PV cell and the energy consumption profile of the BS before normalization, and after normalization for the given example, respectively. The energy generation profile of a south-oriented PV cell covering the total surface area ($A = 5\text{m}^2$) is depicted. The shapes of the two profiles are the same in both figures. The relationship between the energy generation profile and the energy consumption profile is the same in both figures. Only the description of the primary y-axis and secondary y-axis changes between the two figures.

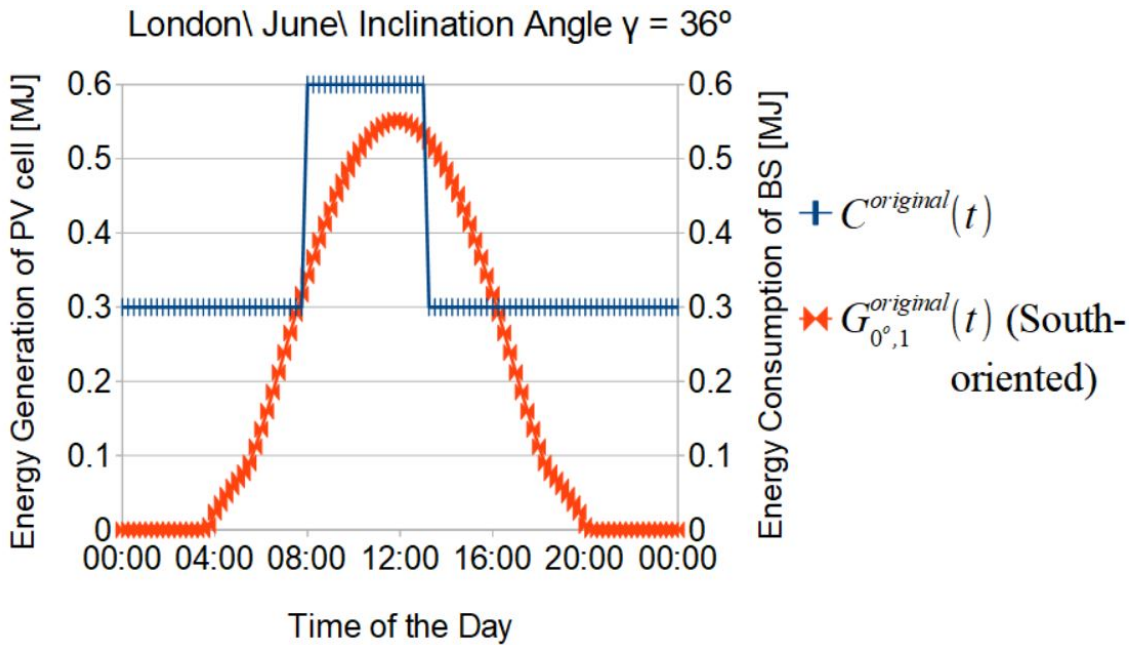


Figure 3: Energy generation profile $G_{0^\circ,1}^{\text{original}}(t)$ and energy consumption profile $C^{\text{original}}(t)$ before normalization.

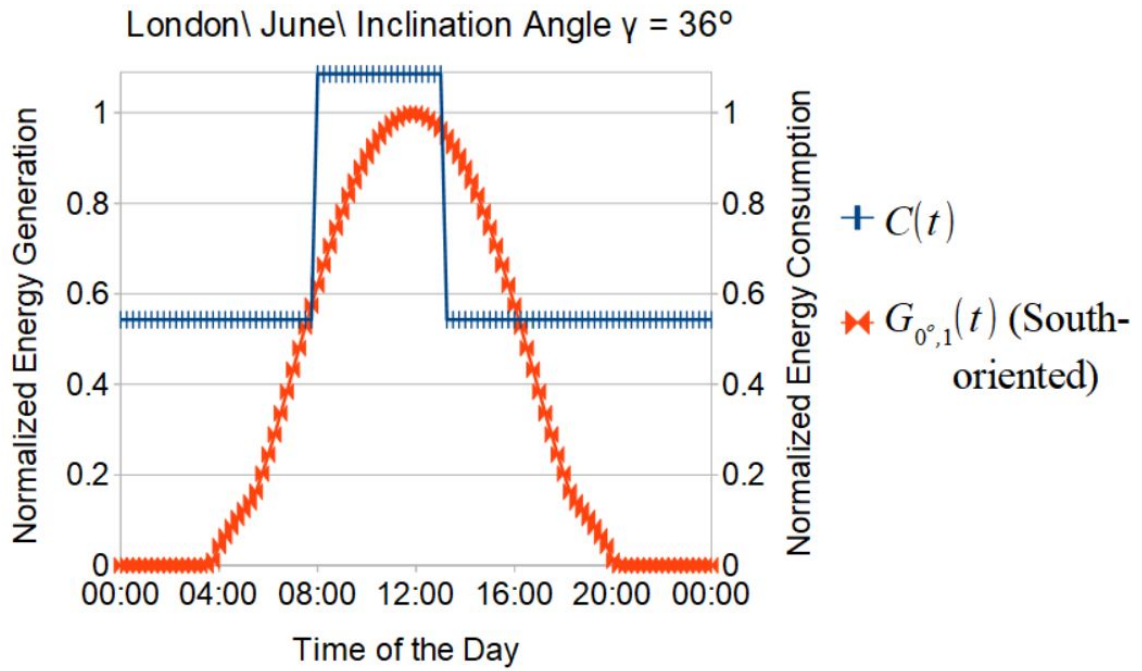


Figure 4: Energy generation profile $G_{0^\circ,1}(t)$ and energy consumption profile $C(t)$ after normalization.

Figure 4 reveals that the energy consumption profile is similar to the business-area traffic load profile from Chapter 2 (one significant peak during sunrise and sunset). In addition, Figure 4 reveals that the energy generation is slightly smaller than the energy consumption, i.e., $G < C$. That means, the orientation angle optimization for this example will show a similar behavior as that of table cell (e) in Table 2.2, Table 2.4, and Table 2.6, if 1 PV cell, 2 PV cells, and 3 PV cells are deployed on the total surface area of 5m^2 , respectively. The optimal solution in this example is to deploy one PV cell (or several PV cells) with the (same) optimized orientation angle on the total surface area of 5m^2 . The optimal orientation angle will be slightly to the east because the energy consumption peak is slightly shifted to the morning hours. The exact value of the optimal orientation can be calculate with the method presented in Chapter 2.

Appendix B

MATLAB Source Code of Chapter 2 [56]

Main File:

```

1 % All angles are in degree measures.
2 close all
3 clear()
4
5 albedo = 0.2; % grassland
6 theta = 0; % orientation angle, degree measure, south=0, west=90, east=-90
7 gamma_angle = 36; % inclination angle, degree measure, horizontally mounted:
   gamma_angle=0
8 Norm = 614; % normalization of energy values, 614 W/m^2 because this is highest
   value for gamma_angle=36 and theta=0 at noon in Jun in Greenwich
9 range_of_optimum_points = 100000; %if this parameter is very big then some of the
   optimum points/stripes are not visible in the output graph, if this parameter
   is very small then the red points (red stripes) are too thick in the graph (too
   many points are marked as optimum points/stripes)
10
11 N = 2; %Number of PV cells
12 T = 96; %Number of time steps
13 d = 165; %Day of the year (d=165 is day in June)( 1^st of January is d=1)
14
15 lon = 0.0003; %Longitude of Greenwich, degree measure
16 lat = 51.4767; %Latitude of Greenwich, degree measure
17
18 load_profile = 1; % 1==Constant Load Profile, 2==Business Load Profile, 3==
   Residential Load Profile
19 off_set = 0.9; %off_set (load_profile): C(t)=off_set (Constant Load Profile),C(
   t)=scale*C_bis+off_set (Business Load Profile), C(t)=scale*C_res+off_set (
   Residential Load Profile)
20 scale = 1; %scale (load_profile): C(t)=off_set (Constant Load Profile),C(t)
   =scale*C_bis+off_set (Business Load Profile), C(t)=scale*C_res+off_set (
   Residential Load Profile)
21 time_step_when_data_starts = 17; %to read in the data from text file (17 for June
   in Greenwich)
22 time_step_when_data_ends = T - time_step_when_data_starts + 2; %+2 for Greenwich
23
24 Input_t_GHI_DHI_DNI_Load = zeros(T,5);
25 at_bt_ct = zeros(T,3);

```

```

26 Output_t_I_Ib_ReindlId_Ig_At_omega_cosZeta = zeros(T,8);
27
28 fileID = fopen('jun-dailyrad512836N-000001W-0deg-0deg.txt','r'); %horizontally
    mounted PV cell in June at Greenwich as baseline to get GHI, DHI, DNI
29 for i = 1:7 % removes header from input data file
30     handle = fgetl(fileID);
31 end
32
33 for t = time_step_when_data_starts:time_step_when_data_ends
34     handle = fgetl(fileID);
35     handle = fscanf(fileID, '%s', 1 );
36     GHI = fscanf(fileID, '%s', 1 );
37     DHI = fscanf(fileID, '%s', 1 );
38     DNI = fscanf(fileID, '%s', 1 );
39
40     Input_t_GHI_DHI_DNI_Load(t,2) = str2num(GHI);
41     Input_t_GHI_DHI_DNI_Load(t,3) = str2num(DHI);
42     Input_t_GHI_DHI_DNI_Load(t,4) = str2num(DNI);
43 end
44
45 handle = fclose(fileID);
46 % symmetrisation of data
47 for t=1:T/2
48     Input_t_GHI_DHI_DNI_Load(t,2) = (Input_t_GHI_DHI_DNI_Load(t,2)+
        Input_t_GHI_DHI_DNI_Load(T-t+1,2))/2;
49     Input_t_GHI_DHI_DNI_Load(T-t+1,2) = Input_t_GHI_DHI_DNI_Load(t,2);
50     Input_t_GHI_DHI_DNI_Load(t,3) = (Input_t_GHI_DHI_DNI_Load(t,3)+
        Input_t_GHI_DHI_DNI_Load(T-t+1,3))/2;
51     Input_t_GHI_DHI_DNI_Load(T-t+1,3) = Input_t_GHI_DHI_DNI_Load(t,3);
52     Input_t_GHI_DHI_DNI_Load(t,4) = (Input_t_GHI_DHI_DNI_Load(t,4)+
        Input_t_GHI_DHI_DNI_Load(T-t+1,4))/2;
53     Input_t_GHI_DHI_DNI_Load(T-t+1,4) = Input_t_GHI_DHI_DNI_Load(t,4);
54 end
55
56 for t = 1:T
57     Input_t_GHI_DHI_DNI_Load(t,1) = t;
58 end
59
60 fileID = fopen('load_profiles.txt','r');
61 handle = fgetl(fileID); %removes header of table
62
63 for t = 1:T
64     handle = fscanf(fileID, '%s', 1 );
65     C_con = fscanf(fileID, '%s', 1 );

```

```

66     C_bis = fscanf(fileID, '%s', 1);
67     C_res = fscanf(fileID, '%s', 1);
68
69     if (load_profile==1)
70         Input_t_GHI_DHI_DNI_Load(t,5) = str2num(C_con)*scale+off_set;
71     else if load_profile==2
72         Input_t_GHI_DHI_DNI_Load(t,5) = str2num(C_bis)*scale+off_set;
73     else if load_profile==3
74         Input_t_GHI_DHI_DNI_Load(t,5) = str2num(C_res)*scale+off_set;
75     else
76         disp('Error load_profile_index');
77     end
78     end
79     end
80 end
81
82 handle = fclose(fileID);
83
84 E_con = 1367;
85 %Calculation of extraterrestrial radiation (depends on the day of the year), in
      degree measure
86 E_d = E_con*(1+0.033*cosd((360/365)*d));
87 %Calculation of declination angle (depends on the day of the year), in degree
      measure
88 delta = 23.45*sind(360/365*(284+d));
89
90 %the following for-loop calculates the the energy generation profile of 1 PV cell
      out of the N PV cells
91
92 for t = 1:T
93     % time step index
94     Output_t_I_Ib_ReindlId_Ig_At_omega_cosZeta(t,1) = t;
95
96     % Calculation of anisotropy index A_t
97     Output_t_I_Ib_ReindlId_Ig_At_omega_cosZeta(t,6) = Input_t_GHI_DHI_DNI_Load(t,4)/
          E_d;
98
99     % Calculation of omega at Greenwich
100    Output_t_I_Ib_ReindlId_Ig_At_omega_cosZeta(t,7) = -180+1.875+(t-1)/T*360;
101
102    % Calculation of cos(zeta), zeta is solar zenith angle
103    omega = Output_t_I_Ib_ReindlId_Ig_At_omega_cosZeta(t,7);
104    Output_t_I_Ib_ReindlId_Ig_At_omega_cosZeta(t,8)=sind(lat)*sind(delta)+cosd(lat)*
          cosd(delta)*cosd(omega);

```

```

105
106 % Calculation of a_t, b_t, and c_t
107 at_bt_ct(t,1) = sind(delta)*sind(lat)*cosd(gamma_angle)+cosd(delta)*cosd(lat)*
        cosd(gamma_angle)*cosd(omega);
108 at_bt_ct(t,2) = cosd(delta)*sind(gamma_angle)*sind(omega);
109 at_bt_ct(t,3) = -sind(delta)*cosd(lat)*sind(gamma_angle)+cosd(delta)*sind(lat)*
        sind(gamma_angle)*cosd(omega);
110
111 % Calculation of the direct-beam irradiance I_b = DNI*max(0,cos(AOI))
112 Output_t_I_Ib_ReindlId_Ig_At_omega_cosZeta(t,3) = I_beam(theta,t, Norm,N,
        Input_t_GHI_DHI_DNI_Load, at_bt_ct);
113
114 % Calculation of the sky-diffuse irradiance I_d (Reindl model)
115 Output_t_I_Ib_ReindlId_Ig_At_omega_cosZeta(t,4) = I_diffuse(theta,gamma_angle,t,
        Norm,N, Input_t_GHI_DHI_DNI_Load, Output_t_I_Ib_ReindlId_Ig_At_omega_cosZeta,
        at_bt_ct);
116
117 % Calculation of the ground-reflected irradiance I_g = GHI*albedo*(1-cosd(
        gamma_angle))/2
118 Output_t_I_Ib_ReindlId_Ig_At_omega_cosZeta(t,5) = I_ground(gamma_angle, albedo,t,
        Norm,N, Input_t_GHI_DHI_DNI_Load);
119
120 % Calculation of total irradiance I=I_b+I_d+I_g;
121 Output_t_I_Ib_ReindlId_Ig_At_omega_cosZeta(t,2) =
        Output_t_I_Ib_ReindlId_Ig_At_omega_cosZeta(t,3) +
        Output_t_I_Ib_ReindlId_Ig_At_omega_cosZeta(t,4) +
        Output_t_I_Ib_ReindlId_Ig_At_omega_cosZeta(t,5);
122
123 % Remove ground-reflected irradiance (it is independent of the orientation angle
        theta) from load profile
124 Input_t_GHI_DHI_DNI_Load(t,5) = Input_t_GHI_DHI_DNI_Load(t,5) - N*
        Output_t_I_Ib_ReindlId_Ig_At_omega_cosZeta(t,5);
125 end
126
127
128 % Creation of output graph for 1 PV cell/ 2 PV cells or 3 PV cells ,
129 % Ground-reflected irradiance is already removed from load profile
130
131 if (N==1)
132     [f, minimum, maximum, optimum_angles] = print_1D_graph(gamma_angle, N, T, Norm,
        Input_t_GHI_DHI_DNI_Load, Output_t_I_Ib_ReindlId_Ig_At_omega_cosZeta, at_bt_ct
        , range_of_optimum_points);
133 else if (N==2)
134     [f, minimum, maximum, optimum_angles] = print_2D_graph(gamma_angle, N, T, Norm,

```

```

        Input_t_GHI_DHI_DNI_Load , Output_t_I_Ib_ReindlId_Ig_At_omega_cosZeta ,
        at_bt_ct , range_of_optimum_points);
135     else if (N==3)
136         [f, minimum, maximum, optimum_angles] = print_3D_graph(gamma_angle, N, T, Norm,
            Input_t_GHI_DHI_DNI_Load , Output_t_I_Ib_ReindlId_Ig_At_omega_cosZeta ,
            at_bt_ct , range_of_optimum_points);
137     else
138         disp('Error: N is not 1, 2, or 3')
139     end
140 end
141 end

```

Ground-reflected Irradiance:

```

1 function [ I_g ] = I_ground(gamma_angle, albedo, t, Norm, N, Input_t_GHI_DHI_DNI_Load)
2 % Calculation of the ground-reflected irradiance  $I_g = GHI * albedo * (1 - \cos(\gamma)) / 2$ 
   gamma_angle) / 2
3 GHI = Input_t_GHI_DHI_DNI_Load(t, 2);
4
5 I_g = (GHI / (Norm * N)) * albedo * (1 - cosd(gamma_angle)) / 2;
6 end

```

Direct-beam Irradiance:

```

1 function [ I_b ] = I_beam(theta, t, Norm, N, Input_t_GHI_DHI_DNI_Load, at_bt_ct)
2 % Calculation of the direct-beam irradiance  $I_b = DNI * \max(0, \cos(AOI))$ 
3 cos_of_AOI = at_bt_ct(t, 1) + at_bt_ct(t, 2) * sind(theta) + at_bt_ct(t, 3) * cosd(theta)
   ; %AOI is angle of incidence
4 DNI = Input_t_GHI_DHI_DNI_Load(t, 4);
5
6 I_b = (DNI / (Norm * N)) * max(0, cos_of_AOI);
7 end

```

Sky-diffuse Irradiance:

```

1 function [ I_d ] = I_diffuse(theta, gamma_angle, t, Norm, N, Input_t_GHI_DHI_DNI_Load,
   Output_t_I_Ib_ReindlId_Ig_At_omega_cosZeta, at_bt_ct)
2 % Calculation of the sky-diffuse irradiance  $I_d$  (Reindl model)
3
4 small = 0.000001;
5 if Input_t_GHI_DHI_DNI_Load(t, 2) < small

```

```

6     % prevent division by zero
7     Input_t_GHI_DHI_DNI_Load(t,2) = small;
8 end
9
10 A_t = Output_t_I_Ib_ReindlId_Ig_At_omega_cosZeta(t,6); %A_t is anisotropy index
11 cos_of_zeta = Output_t_I_Ib_ReindlId_Ig_At_omega_cosZeta(t,8); %zeta is solar
    zenith angle
12 cos_of_AOI = at_bt_ct(t,1) + at_bt_ct(t,2)*sind(theta) + at_bt_ct(t,3)*cosd(theta)
    ; %AOI is angle of incidence
13 GHI = Input_t_GHI_DHI_DNI_Load(t,2);
14 DHI = Input_t_GHI_DHI_DNI_Load(t,3);
15 DNI = Input_t_GHI_DHI_DNI_Load(t,4);
16
17 I_d = (DHI/(Norm*N))*((A_t*max(0,cos_of_AOI)/max(0.000001,cos_of_zeta))+(1-A_t)
    *((1+cosd(gamma_angle))/2)*(1+sqrt(max(0,DNI*cos_of_zeta)/GHI)*(sind(
    gamma_angle/2)^3)));
18 end

```

Normalized Energy Drawn from the Main Grid:

```

1 function [normalized_energy] = normalized_energy_drawn_from_the_main_grid(
    gamma_angle,N,T,Norm,Input_t_GHI_DHI_DNI_Load ,
    Output_t_I_Ib_ReindlId_Ig_At_omega_cosZeta ,theta ,at_bt_ct)
2     normalized_energy = 0;
3
4     for t = 1:T
5         Load = Input_t_GHI_DHI_DNI_Load(t,5);
6         for n = 1:N
7             Load = Load - I_beam(theta(n),t,Norm,N,Input_t_GHI_DHI_DNI_Load ,
                at_bt_ct) - I_diffuse(theta(n),gamma_angle,t,Norm,N,
                Input_t_GHI_DHI_DNI_Load , Output_t_I_Ib_ReindlId_Ig_At_omega_cosZeta
                ,at_bt_ct);
8         end
9         normalized_energy = normalized_energy + max(Load ,0);
10    end
11 end

```

Output (1 PV Cell):

```

1 function [f,minimum,maximum,optimum_angles] = print_1D_graph(gamma_angle,N,T,Norm,
    Input_t_GHI_DHI_DNI_Load , Output_t_I_Ib_ReindlId_Ig_cosAOI_omega ,at_bt_ct ,
    range_of_optimum_points)

```

```

2
3  f = figure;
4  set(f, 'position', [50 50 700 700])
5
6  theta = zeros(1,1);
7  V(1:181,1:181) = 100000;
8  [X,Y] = meshgrid(-90:90);
9  optimum_angles = zeros(1,1);
10
11  for theta_1 = -90:90
12      theta(1) = theta_1;
13      for i = 1:181
14          V(theta_1+91,i) = normalized_energy_drawn_from_the_main_grid(
              gamma_angle,N,T,Norm,Input_t_GHI_DHI_DNI_Load ,
              Output_t_I_Ib_ReindIId_Ig_cosAOI_omega , theta , at_bt_ct);
15      end
16  end
17
18  minimum = min(min(V));
19  maximum = max(max(V));
20
21  axis([-90 90 -90 90 minimum maximum]);
22  xticks(-90:45:90);
23  yticks([]);
24  set(gca, 'FontSize', 16);
25  xlabel('Orientation Angle of PV Cell 1 (\theta_1)');
26
27  % mark all optimum points with red stripes
28  hold on
29  minimum = round(minimum*range_of_optimum_points)/range_of_optimum_points;
30  j = 1;
31  for theta_1 = -90:90
32      for theta_2 = -90:90
33          val = round(V(theta_1+91,theta_2+91)*range_of_optimum_points)/
              range_of_optimum_points;
34          if val <= minimum
35              view(0, 90);
36              set(gca, 'position', [0.5 0.5 0.4 0.05]);
37              plot3(Y(theta_1+91,theta_2+91),X(theta_1+91,theta_2+91),V(theta_1
                  +91,theta_2+91), 'r', 'markersize', 20);
38              if theta_2 == 0
39                  optimum_angles(j,1) = theta_1;
40                  j = j+1;
41              end

```

```

42         end
43     end
44 end
45
46     set(surf(Y,X,V), 'edgecolor', 'none');
47     colorBar = colorbar('southoutside');
48     colormap(colorBar, flipud(colormap));
49     colormap(flipud(colormap));
50     set(colorBar, 'position', [0.5 0.35 0.4 0.03]);
51     colorBar.Label.String = 'Normalized Energy drawn from the Grid';
52     colorBar.Label.FontSize = 16.5;
53 end

```

Output (2 PV Cells):

```

1 function [f, minimum, maximum, optimum_angles] = print_2D_graph(gamma_angle, N, T, Norm,
    Input_t_GHI_DHI_DNI_Load, Output_t_I_Ib_ReindIId_Ig_cosAOI_omega, at_bt_ct,
    range_of_optimum_points)
2
3     f = figure;
4     set(f, 'position', [100 100 550 450])
5
6     theta = zeros(1,2);
7     V(1:181,1:181) = 100000;
8     [X,Y] = meshgrid(-90:1:90);
9     optimum_angles = zeros(1,2);
10
11    for theta_1 = -90:90
12        for theta_2 = -90:90
13            theta(1) = theta_1;
14            theta(2) = theta_2;
15            V(theta_1+91, theta_2+91) = normalized_energy_drawn_from_the_main_grid(
                gamma_angle, N, T, Norm, Input_t_GHI_DHI_DNI_Load,
                Output_t_I_Ib_ReindIId_Ig_cosAOI_omega, theta, at_bt_ct);
16        end
17    end
18
19    minimum = min(min(V));
20    maximum = max(max(V));
21
22    set(surf(X,Y,V), 'edgecolor', 'none');
23    set(gca, 'position', [0.2 0.2 0.6 0.6]);
24    axis([-90 90 -90 90 minimum maximum]);
25    xticks(-90:45:90);

```



```

26     yticks(-90:45:90);
27     set(gca,'FontSize',14);
28
29     colormap( flipud(colormap) );
30     colorBar = colorbar;
31     colorBar.Label.String = 'Normalized Energy drawn from the Grid';
32     colorBar.Label.FontSize = 14;
33     set(gca,'FontSize',14)
34
35     xlabel('Orientation Angle of PV Cell 1 (\theta_1)');
36     ylabel('Orientation Angle of PV Cell 2 (\theta_2)');
37     zlabel('Normalized Energy drawn from the Grid');
38
39     % mark all optimum points with red points
40     hold on
41     minimum = round(minimum*range_of_optimum_points)/range_of_optimum_points;
42     j = 1;
43     for theta_1 = -90:90
44         for theta_2 = -90:90
45             val=round(V(theta_1+91,theta_2+91)*range_of_optimum_points)/
46                 range_of_optimum_points;
47             if val <= minimum
48                 view(0, 90);
49                 plot3(X(theta_1+91,theta_2+91),Y(theta_1+91,theta_2+91),V(theta_1
50                     +91,theta_2+91),'r','markersize',20);
51                 optimum_angles(j,1) = theta_1;
52                 optimum_angles(j,2) = theta_2;
53                 j = j+1;
54             end
55         end
56     end
57 end

```

Output (3 PV Cells):

```

1 function [f,minimum,maximum,optimum_angles] = print_3D_graph(gamma_angle,N,T,Norm,
2     Input_t_GHI_DHI_DNI_Load, Output_t_I_Ib_ReindIId_Ig_cosAOI_omega , at_bt_ct ,
3     range_of_optimum_points)
4
5
6     f = figure;
7     set(f,'position',[50 50 900 800])
8
9
10    theta = zeros(1,3);
11    V(1:181,1:181,1:181) = 100000;

```

```

8     [X,Y,Z] = meshgrid(-90:1:90);
9     optimum_angles = zeros(1,3);
10    maximum = 0;
11
12    %Generates several layers
13    for theta_1 = -90:1:90
14        for theta_2 = -90:1:90
15            for theta_3 = -90:1:90
16                theta(1) = theta_1;
17                theta(2) = theta_2;
18                theta(3) = theta_3;
19                V(theta_1+91,theta_2+91,theta_3+91) =
                    normalized_energy_drawn_from_the_main_grid(gamma_angle,N,T,Norm
                    ,Input_t_GHI_DHI_DNI_Load,
                    Output_t_I_Ib_ReindIId_Ig_cosAOI_omega ,theta , at_bt_ct );
20            end
21        end
22    end
23
24    minimum = min(min(min(V)));
25    maximum = max(max(max(V)));
26
27    for i = 1:2
28        if i == 1
29            subplot(3,2,[1,3]);
30        end
31        if i == 2
32            subplot(3,2,[2,4]);
33        end
34
35        xslice = [];
36        yslice = 0;
37        zslice = [-90,-45,0,45,90];
38
39        set(slice(X,Y,Z,V,xslice , yslice , zslice) , 'edgecolor' , 'none')
40        axis([-90 90 -90 90 -90 90 minimum maximum])
41        xticks(-90:45:90)
42        yticks(-90:45:90)
43        zticks(-90:45:90)
44        % set(gca, 'Ydir', 'reverse') % This should be active for the second column
45        % in Table V (see reference in thesis)
46
47        % mark all optimum points with red points
48        hold on

```

```

48     minimum = round(minimum*range_of_optimum_points)/range_of_optimum_points;
49     j = 1;
50     for theta_1 = -90:90
51         for theta_2 = -90:90
52             for theta_3 = -90:90
53                 val = round(V(theta_1+91,theta_2+91,theta_3+91)*
54                     range_of_optimum_points)/range_of_optimum_points;
55                 if val <= minimum
56                     plot3(theta_2,theta_1,theta_3,'.r','markersize',20)
57                     if i == 1
58                         optimum_angles(j,1) = theta_1;
59                         optimum_angles(j,2) = theta_2;
60                         optimum_angles(j,3) = theta_3;
61                         j = j+1;
62                     end
63                 end
64             end
65         end
66     end
67     if i == 1
68         view(10,20)
69     else
70         if i == 2
71             view(10,-20)
72         end
73     end
74
75     handle = get(gca,'xlabel');
76     pos = get(handle,'position');
77     pos(2) = 1.1*pos(2) ;
78     set(handle,'position',pos);
79
80     handle = get(gca,'ylabel');
81     pos = get(handle,'position');
82     pos(3) = -95 ;
83     pos(1) = pos(1)*1.05 ;
84     set(handle,'position',pos);
85
86     handle = get(gca,'zlabel');
87     pos = get(handle,'position');
88     pos(2) = 0.5*pos(2) ;
89     set(handle,'position',pos);
90

```

```

91         set(gca, 'FontSize', 17)
92         xlabel ('\theta_1');
93         ylabel ('\theta_2');
94         zlabel ('\theta_3');
95     end
96
97     set(gca, 'FontSize', 17)
98     colorBar = colorbar('southoutside');
99     colorBar.Label.FontSize = 22;
100    colormap(colorBar, flipud(colormap));
101    colormap(flipud(colormap));
102    set(colorBar, 'Position', [0.1 0.3 0.85 0.02])
103    colorBar.Label.String = 'Normalized Energy drawn from the Grid';
104 end

```

Input File (Load Profiles):

1	Time of the Day	/	Constant Load	/	Business Load	/	Residential Load
2	00:00	0	0	0.76			
3	00:15	0	0	0.76			
4	00:30	0	0	0.76			
5	00:45	0	0	0.76			
6	01:00	0	0	0.62			
7	01:15	0	0	0.62			
8	01:30	0	0	0.62			
9	01:45	0	0	0.62			
10	02:00	0	0	0.49			
11	02:15	0	0	0.49			
12	02:30	0	0	0.49			
13	02:45	0	0	0.49			
14	03:00	0	0	0.38			
15	03:15	0	0	0.38			
16	03:30	0	0	0.38			
17	03:45	0	0	0.38			
18	04:00	0	0	0.33			
19	04:15	0	0	0.33			
20	04:30	0	0	0.33			
21	04:45	0	0	0.33			
22	05:00	0	0	0.36			
23	05:15	0	0	0.36			
24	05:30	0	0	0.36			
25	05:45	0	0	0.36			
26	06:00	0	0	0.4			
27	06:15	0	0	0.4			

28	06:30	0	0	0.4
29	06:45	0	0	0.4
30	07:00	0	0.1136	0.51
31	07:15	0	0.1136	0.51
32	07:30	0	0.1136	0.51
33	07:45	0	0.1136	0.51
34	08:00	0	0.2273	0.6
35	08:15	0	0.2273	0.6
36	08:30	0	0.2273	0.6
37	08:45	0	0.2273	0.6
38	09:00	0	0.8636	0.13
39	09:15	0	0.8636	0.13
40	09:30	0	0.8636	0.13
41	09:45	0	0.8636	0.13
42	10:00	0	0.8863	0.13
43	10:15	0	0.8863	0.13
44	10:30	0	0.8863	0.13
45	10:45	0	0.8863	0.13
46	11:00	0	0.9091	0.13
47	11:15	0	0.9091	0.13
48	11:30	0	0.9091	0.13
49	11:45	0	0.9091	0.13
50	12:00	0	0.7727	0.22
51	12:15	0	0.7727	0.22
52	12:30	0	0.7727	0.22
53	12:45	0	0.7727	0.22
54	13:00	0	0.9205	0.13
55	13:15	0	0.9205	0.13
56	13:30	0	0.9205	0.13
57	13:45	0	0.9205	0.13
58	14:00	0	0.9432	0.13
59	14:15	0	0.9432	0.13
60	14:30	0	0.9432	0.13
61	14:45	0	0.9432	0.13
62	15:00	0	0.9659	0.13
63	15:15	0	0.9659	0.13
64	15:30	0	0.9659	0.13
65	15:45	0	0.9659	0.13
66	16:00	0	1	0.13
67	16:15	0	1	0.13
68	16:30	0	1	0.13
69	16:45	0	1	0.13
70	17:00	0	1	0.13
71	17:15	0	1	0.13

72	17:30	0	1	0.13
73	17:45	0	1	0.13
74	18:00	0	0.8409	0.24
75	18:15	0	0.8409	0.24
76	18:30	0	0.8409	0.24
77	18:45	0	0.8409	0.24
78	19:00	0	0.6023	0.47
79	19:15	0	0.6023	0.47
80	19:30	0	0.6023	0.47
81	19:45	0	0.6023	0.47
82	20:00	0	0.1705	0.82
83	20:15	0	0.1705	0.82
84	20:30	0	0.1705	0.82
85	20:45	0	0.1705	0.82
86	21:00	0	0.0455	0.98
87	21:15	0	0.0455	0.98
88	21:30	0	0.0455	0.98
89	21:45	0	0.0455	0.98
90	22:00	0	0.0341	1
91	22:15	0	0.0341	1
92	22:30	0	0.0341	1
93	22:45	0	0.0341	1
94	23:00	0	0.0227	0.82
95	23:15	0	0.0227	0.82
96	23:30	0	0.0227	0.82
97	23:45	0	0.0227	0.82

Input File (PVGIS [10]):

```

1 Latitude:      51o28'36'' North,
2 Longitude:    0o0'1'' West
3
4 Results for:   June
5
6 Inclination of plane:  0      deg.
7 Orientation (azimuth) of plane:  0      deg.
8 Time          G          Gd          DNI
9 04:07         30         29         31
10 04:22         48         44         52
11 04:37         67         59         76
12 04:52         88         74         102
13 05:07        111         88         127
14 05:22        134        102         150
15 05:37        159        116         172

```

16	05:52	184	129	191
17	06:07	209	141	209
18	06:22	234	152	226
19	06:37	260	163	241
20	06:52	285	173	255
21	07:07	309	183	267
22	07:22	333	191	279
23	07:37	356	199	289
24	07:52	378	206	299
25	08:07	400	212	308
26	08:22	420	218	316
27	08:37	439	223	323
28	08:52	457	227	330
29	09:07	474	230	335
30	09:22	489	234	341
31	09:37	503	236	345
32	09:52	516	238	350
33	10:07	527	240	353
34	10:22	537	241	356
35	10:37	545	242	359
36	10:52	552	243	361
37	11:07	558	244	363
38	11:22	562	244	364
39	11:37	565	245	365
40	11:52	566	245	366
41	12:07	566	245	366
42	12:22	565	245	365
43	12:37	562	244	364
44	12:52	558	244	363
45	13:07	552	243	361
46	13:22	545	242	359
47	13:37	537	241	356
48	13:52	527	240	353
49	14:07	516	238	350
50	14:22	503	236	345
51	14:37	489	234	341
52	14:52	474	230	335
53	15:07	457	227	330
54	15:22	439	223	323
55	15:37	420	218	316
56	15:52	400	212	308
57	16:07	378	206	299
58	16:22	356	199	289
59	16:37	333	191	279

60	16:52	309	183	267
61	17:07	285	173	255
62	17:22	260	163	241
63	17:37	234	152	226
64	17:52	209	141	209
65	18:07	184	129	191
66	18:22	159	116	172
67	18:37	134	102	150
68	18:52	111	88	127
69	19:07	88	74	102
70	19:22	67	59	76
71	19:37	48	44	52
72	19:52	30	29	31
73	20:07	14	14	16

74

75 G: Global irradiance on a fixed plane (W/m²)

76 Gd: Diffuse irradiance on a fixed plane (W/m²)

77 DNI: Direct normal irradiance (W/m²)

78

79 PVGIS (c) European Communities, 2001–2012

References

- [1] D. Benda, X. Chu, S. Sun, T. Q. S. Quek, and A. Buckley, “Renewable energy sharing among base stations as a min-cost-max-flow optimization problem,” *IEEE Transactions on Green Communications and Networking*, vol. 3, no. 1, pp. 67 – 78, March 2019.
- [2] D. Benda, S. Sun, X. Chu, T. Q. S. Quek, and A. Buckley, “PV cell angle optimization for energy generation-consumption matching in a solar powered cellular network,” *IEEE Transactions on Green Communications and Networking*, vol. 2, no. 1, pp. 40 – 48, March 2018.
- [3] D. Benda, X. Chu, S. Sun, T. Q. S. Quek, and A. Buckley, “Optimal clustering of energy-harvesting base stations,” in *Proc. IEEE VTS APWCS*, Hsinchu, Taiwan, Aug 2018.
- [4] D. Benda, X. Chu, S. Sun, T. Q. S. Quek, and A. Buckley, “Modeling and optimization of energy sharing among base stations as a minimum-cost-maximum-flow problem,” in *Proc. IEEE VTC-Spring*, Porto, Portugal, Jun 2018.
- [5] D. Benda, X. Chu, S. Sun, T. Q. S. Quek, and A. Buckley, “PV cell orientation angle optimization for a solar energy harvesting base station,” in *Proc. IEEE GLOBECOM*, Singapore, Dec 2017.
- [6] D. Benda, X. Chu, S. Sun, T. Q. S. Quek, and A. Buckley, “PV cell angle optimisation for energy arrival-consumption matching in a solar energy harvesting cellular network,” in *Proc. IEEE ICC*, Paris, France, May 2017.

- [7] D. Benda, S. Sun, X. Chu, T. Q. S. Quek, and A. Buckley, "PV cell orientation angles optimization for a base station equipped with several PV cells," submitted to *IEEE Transactions on Green Communications and Networking*.
- [8] D. Benda, S. Sun, X. Chu, T. Q. S. Quek, and A. Buckley, "Optimal deployment of energy harvesters with anti-correlated energy generation at base stations," submitted to *GLOBECOM 2019*.
- [9] A. Luque and S. Hegedus, *Handbook of Photovoltaic Science and Engineering*, 2nd ed. Chichester, United Kingdom: John Wiley & Sons, Ltd, 2011, pp. 8–9.
- [10] European Commission. (2019) Photovoltaic geographical information system (PVGIS). [Online]. Available: <http://re.jrc.ec.europa.eu/pvgis/>
- [11] A. Luque and S. Hegedus, *Handbook of Photovoltaic Science and Engineering*, 2nd ed. Chichester, United Kingdom: John Wiley & Sons, Ltd, 2011, p. 991.
- [12] Y. Wu, Y. Chen, J. Tang, D. K. C. So, Z. Xu, C. L. I, P. Ferrand, J. M. Gorce, C. H. Tang, P. R. Li, K. T. Feng, L. C. Wang, K. Borner, and L. Thiele, "Green transmission technologies for balancing the energy efficiency and spectrum efficiency trade-off," *IEEE Communications Magazine*, vol. 52, no. 11, pp. 112 – 120, Nov 2014.
- [13] A. Kwasinski and A. Kwasinski, "Increasing sustainability and resiliency of cellular network infrastructure by harvesting renewable energy," *IEEE Communications Magazine*, vol. 53, no. 4, pp. 110 – 116, Apr 2015.
- [14] Y. Mao, Y. Luo, J. Zhang, and K. B. Letaief, "Energy harvesting small cell networks: feasibility, deployment, and operation," *IEEE Communications Magazine*, vol. 53, no. 6, pp. 94 – 101, Jun 2015.
- [15] M. D. Mueck, I. Karls, R. Arefi, T. Haustein, R. J. Weiler, and K. Sakaguchi, "Global standards enabling a 5th generation communications system architecture vision," in *Proc. IEEE GLOBECOM Workshops*, Austin, TX USA, Dec 2014.

- [16] H. Zhang, X. Chu, W. Guo, and S. Wang, “Coexistence of Wi-Fi and heterogeneous small cell networks sharing unlicensed spectrum,” *IEEE Communications Magazine*, vol. 53, no. 3, pp. 158 – 164, Mar 2015.
- [17] S. Samarakoon, M. Bennis, W. Saad, M. Debbah, and M. Latva-Aho, “Ultra dense small cell networks: Turning density into energy efficiency,” *IEEE Journal on Selected Areas in Communications*, vol. 34, no. 5, pp. 1267 – 1280, May 2016.
- [18] G. Piro, M. Miozzo, G. Forte, N. Baldo, L. A. Grieco, G. Boggia, and P. Dini, “HetNets powered by renewable energy sources: Sustainable next-generation cellular networks,” *IEEE Internet Computing*, vol. 17, no. 1, pp. 32 – 39, Jan 2013.
- [19] H. Wang, H. Li, C. Tang, L. Ye, X. Chen, H. Tang, and S. Ci, “Modeling, metrics, and optimal design for solar energy-powered base station system,” *EURASIP Journal on Wireless Communications and Networking*, vol. 2015, no. 1, pp. 1 – 17, Feb 2015.
- [20] P. Nema, R. Nema, and S. Rangnekar, “Minimization of green house gases emission by using hybrid energy system for telephony base station site application,” *Renewable and Sustainable Energy Reviews*, vol. 14, no. 6, pp. 1635 – 1639, Aug 2010.
- [21] K. Huang, M. Kountouris, and V. O. K. Li, “Renewable powered cellular networks: Energy field modeling and network coverage,” *IEEE Transactions on Wireless Communications*, vol. 14, no. 8, pp. 4234 – 4247, Aug 2015.
- [22] H. Wang, H. Li, Z. Wang, X. Chen, and S. Ci, “Stochastic queue modeling and key design metrics analysis for solar energy powered cellular networks,” in *Proc. International Conference on Computing, Networking and Communications (ICNC)*, Feb 2014, pp. 472 – 477.

- [23] M. A. Marsan, G. Bucalo, A. Di Caro, M. Meo, and Y. Zhang, "Towards zero grid electricity networking: Powering BSs with renewable energy sources," in *Proc. IEEE ICC*, June 2013, pp. 596 – 601.
- [24] T. Han and N. Ansari, "Powering mobile networks with green energy," *IEEE Wireless Communications*, vol. 21, no. 1, pp. 90 – 96, Feb 2014.
- [25] R. Luthander, J. Widén, D. Nilsson, and J. Palm, "Photovoltaic self-consumption in buildings: A review," *Applied Energy*, vol. 142, pp. 80 – 94, Mar 2015.
- [26] R. Eke and A. Senturk, "Performance comparison of a double-axis sun tracking versus fixed PV system," *Solar Energy*, vol. 86, no. 9, pp. 2665 – 2672, Sep 2012.
- [27] T. Huld, "PVMAPS: software tools and data for the estimation of solar radiation and photovoltaic module performance over large geographical areas," *Solar Energy*, vol. 142, pp. 171 – 181, Jan 2017.
- [28] T. Huld, R. Gottschalg, H. G. Beyer, and M. Topič, "Mapping the performance of PV modules, effects of module type and data averaging," *Solar Energy*, vol. 84, no. 2, pp. 324 – 338, Feb 2010.
- [29] T. Huld and A. M. G. Amillo, "Estimating PV module performance over large geographical regions: The role of irradiance, air temperature, wind speed and solar spectrum," *Energies*, vol. 8, no. 6, pp. 5159 – 5181, Jun 2015.
- [30] National Renewable Energy Laboratory. (2019) Geographical information system USA. [Online]. Available: <https://www.nrel.gov/gis/solar.html>
- [31] Global Solar Atlas. (2019) Geographical information system - worldwide. [Online]. Available: <https://globalsolaratlas.info/>
- [32] Solargis. (2019) Geographical information system - every country. [Online]. Available: <https://solargis.com/maps-and-gis-data/overview>

- [33] J. Ordóñez, E. Jadraque, J. Alegre, and G. Martínez, “Analysis of the photovoltaic solar energy capacity of residential rooftops in Andalusia (Spain),” *Renewable and Sustainable Energy Reviews*, vol. 14, no. 7, pp. 2122 – 2130, Sep 2010.
- [34] L. G. Valladares-Rendón, G. Schmid, and S.-L. Lo, “Review on energy savings by solar control techniques and optimal building orientation for the strategic placement of façade shading systems,” *Energy and Buildings*, vol. 140, pp. 458 – 479, Apr 2017.
- [35] Y. S. Khoo, A. Nobre, R. Malhotra, D. Yang, R. Ruther, T. Reindl, and A. G. Aberle, “Optimal orientation and tilt angle for maximizing in-plane solar irradiation for PV applications in Singapore,” *IEEE Journal of Photovoltaics*, vol. 4, no. 2, pp. 647 – 653, Mar 2014.
- [36] B. P. Kemery, I. Beausoleil-Morrison, and I. H. Rowlands, “Optimal PV orientation and geographic dispersion: a study of 10 Canadian cities and 16 Ontario locations,” in *Proc. The Canadian Conference on Building Simulation*, Halifax Nova Scotia, Canada, May 2012.
- [37] K. Chattopadhyay, A. Kies, E. Lorenz, L. von Bremen, and D. Heinemann, “The impact of different PV module configurations on storage and additional balancing needs for a fully renewable European power system,” *Renewable Energy*, vol. 113, pp. 176 – 189, Dec 2017.
- [38] A. H. Khan, K. R. Zafreen, A. Islam, and M. Islam, “Shifting generation of energy of solar PV using OPTANG method-case study Sandwip area,” in *Proc. 3rd ICGET*, Dhaka, Bangladesh, Sep 2015.
- [39] O. Perpiñan, E. Lorenzo, and M. A. Castro, “On the calculation of energy produced by a PV grid-connected system,” *Progress in Photovoltaics: Research and Applications*, vol. 15, no. 3, pp. 265 – 274, 2007.

- [40] A. Luque and S. Hegedus, *Handbook of Photovoltaic Science and Engineering*, 2nd ed. Chichester, United Kingdom: John Wiley & Sons, Ltd, 2011, p. 1002.
- [41] A. Luque and S. Hegedus, *Handbook of Photovoltaic Science and Engineering*, 2nd ed. Chichester, United Kingdom: John Wiley & Sons, Ltd, 2011, p. 1005.
- [42] A. Luque and S. Hegedus, *Handbook of Photovoltaic Science and Engineering*, 2nd ed. Chichester, United Kingdom: John Wiley & Sons, Ltd, 2011, p. 986.
- [43] A. Luque and S. Hegedus, *Handbook of Photovoltaic Science and Engineering*, 2nd ed. Chichester, United Kingdom: John Wiley & Sons, Ltd, 2011, p. 989.
- [44] R. Mubarak, M. Hofmann, S. Riechelmann, and G. Seckmeyer, “Comparison of modelled and measured tilted solar irradiance for photovoltaic applications,” *Energies*, vol. 10, no. 11, Oct 2017.
- [45] C. Demain, M. Journée, and C. Bertrand, “Evaluation of different models to estimate the global solar radiation on inclined surfaces,” *Renewable Energy*, vol. 50, pp. 710 – 721, Feb 2013.
- [46] C. Bertrand, G. Vanderveken, and M. Journée, “Evaluation of decomposition models of various complexity to estimate the direct solar irradiance over Belgium,” *Renewable Energy*, vol. 74, pp. 618 – 626, Feb 2015.
- [47] C. A. Gueymard, “Direct and indirect uncertainties in the prediction of tilted irradiance for solar engineering applications,” *Solar Energy*, vol. 83, no. 3, pp. 432 – 444, Mar 2009.
- [48] P. G. Loutzenhiser, H. Manz, C. Felsmann, P. A. Strachan, T. Frank, and G. M. Maxwell, “Empirical validation of models to compute solar irradiance on inclined surfaces for building energy simulation,” *Solar Energy*, vol. 81, no. 2, pp. 254 – 267, Feb 2007.
- [49] A. Luque and S. Hegedus, *Handbook of Photovoltaic Science and Engineering*, 2nd ed. Chichester, United Kingdom: John Wiley & Sons, Ltd, 2011, p. 1004.

- [50] A. Luque and S. Hegedus, *Handbook of Photovoltaic Science and Engineering*, 2nd ed. Chichester, United Kingdom: John Wiley & Sons, Ltd, 2011, p. 988.
- [51] E. Akarslan, F. O. Hocaoglu, and R. Edizkan, “A novel M-D (multi-dimensional) linear prediction filter approach for hourly solar radiation forecasting,” *Energy*, vol. 73, pp. 978 – 986, Aug 2014.
- [52] CelPlan. (2014) White paper - customer experience optimization in wireless networks. [Online]. Available: [http://www.celplan.com/resources/whitepapers/Customer Experience Optimization rev3.pdf](http://www.celplan.com/resources/whitepapers/Customer%20Experience%20Optimization%20rev3.pdf)
- [53] European Commission. (2019) Photovoltaic geographical information system (PVGIS). [Online]. Available: http://re.jrc.ec.europa.eu/pvg_tools/en/tools.html#PVP
- [54] T. Muneer, “Solar radiation model for Europe,” *Building Services Engineering Research and Technology*, vol. 11, no. 4, pp. 153–163, Nov 1990.
- [55] European Commission. (2019) Photovoltaic geographical information system (PVGIS). [Online]. Available: http://re.jrc.ec.europa.eu/pvg_static/methods.html
- [56] D. Benda - GitHub repository. (2019) PV_cell_orientation_angle_optimization. [Online]. Available: https://github.com/DOBEN/PV_cell_orientation_angle_optimization
- [57] A. Kwasinski, “Lessons from field damage assessments about communication networks power supply and infrastructure performance during natural disasters with a focus on hurricane sandy,” in *Proc. FCC workshop on network resiliency*, New York, USA, Feb 2013.
- [58] M. G. Rasmussen, G. B. Andresen, and M. Greiner, “Storage and balancing synergies in a fully or highly renewable pan-European power system,” *Energy Policy*, vol. 51, pp. 642 – 651, Dec 2012.

- [59] Y. Thiaux, J. Seigneurbieux, B. Multon, and H. B. Ahmed, “Load profile impact on the gross energy requirement of stand-alone photovoltaic systems,” *Renewable Energy*, vol. 35, no. 3, pp. 602 – 613, Mar 2010.
- [60] V. Rudolf and K. D. Papastergiou, “Financial analysis of utility scale photovoltaic plants with battery energy storage,” *Energy Policy*, vol. 63, pp. 139 – 146, Dec 2013.
- [61] A. F. Crossland, O. H. Anuta, and N. S. Wade, “A socio-technical approach to increasing the battery lifetime of off-grid photovoltaic systems applied to a case study in Rwanda,” *Renewable Energy*, vol. 83, pp. 30 – 40, Nov 2015.
- [62] M. A. S. Alshushan and I. M. Saleh, “Power degradation and performance evaluation of pv modules after 31 years of work,” in *Proc. IEEE 39th Photovoltaic Specialists Conference (PVSC)*, Tampa, USA, June 2013, pp. 2977 – 2982.
- [63] F. Parzysz, M. Di Renzo, and C. Verikoukis, “Power-availability-aware cell association for energy-harvesting small-cell base stations,” *IEEE Transactions on Wireless Communications*, vol. 16, no. 4, pp. 2409 – 2422, Apr 2017.
- [64] A. H. Sakr and E. Hossain, “Analysis of k-tier uplink cellular networks with ambient RF energy harvesting,” *IEEE Journal on Selected Areas in Communications*, vol. 33, no. 10, pp. 2226 – 2238, Oct 2015.
- [65] T. Wang, J. Wang, C. Jiang, J. Wang, and Y. Ren, “Access strategy in super WiFi network powered by solar energy harvesting: A POMDP method,” in *Proc. IEEE 83rd Vehicular Technology Conference (VTC Spring)*, Nanjing, China, May 2016.
- [66] M. Haenggi, “Stochastic geometry for the analysis and design of 5G cellular networks,” in *Proc. IEEE GLOBECOM*, Austin, TX USA, Dec 2014.
- [67] F. Baccelli and B. Blaszczyszyn, *Stochastic Geometry and Wireless Networks, Volume I - Theory*. Paris, France: Now Publishers, 2009, pp. 1–164.

- [68] M. Haenggi and R. K. Ganti, *Interference in Large Wireless Networks*. Boston, USA: Now Publishers, 2009, pp. 127–248.
- [69] W. Thompson, “Poisson distributions,” *Computing in Science & Engineering*, vol. 3, no. 3, pp. 78 – 82, May 2001.
- [70] M. Sheng, L. Wang, X. Wang, Y. Zhang, C. Xu, and J. Li, “Energy efficient beamforming in MISO heterogeneous cellular networks with wireless information and power transfer,” *IEEE Journal on Selected Areas in Communications*, vol. 34, no. 4, pp. 954 – 968, Apr 2016.
- [71] Y. Guo, L. Duan, and R. Zhang, “Optimal pricing and load sharing for energy saving with cooperative communications,” *IEEE Transactions on Wireless Communications*, vol. 15, no. 2, pp. 951 – 964, Feb 2016.
- [72] M. Wildemeersch, T. Q. S. Quek, C. H. Slump, and A. Rabbachin, “Cognitive small cell networks: Energy efficiency and trade-offs,” *IEEE Transactions on Communications*, vol. 61, no. 9, pp. 4016 – 4029, Sep 2013.
- [73] P.-S. Yu, J. Lee, T. Q. S. Quek, and Y.-W. P. Hong, “Traffic offloading in heterogeneous networks with energy harvesting personal cells-network throughput and energy efficiency,” *IEEE Transactions on Wireless Communications*, vol. 15, no. 2, pp. 1146 – 1161, Feb 2016.
- [74] J. Wu, Y. Zhang, M. Zukerman, and E. K.-N. Yung, “Energy-efficient base-stations sleep-mode techniques in green cellular networks: A survey,” *IEEE Communications Surveys & Tutorials*, vol. 17, no. 2, pp. 803 – 826, 2015.
- [75] D. Huang, W. Wei, Y. Gao, M. Hou, Y. Li, and H. Song, “Energy efficient dynamic optimal control of LTE base stations: solution and trade-off,” *Telecommunication Systems*, vol. 66, no. 4, pp. 701 – 712, Dec 2017.
- [76] M. W. Kang and Y. W. Chung, “An efficient energy saving scheme for base stations in 5G networks with separated data and control planes using particle swarm optimization,” *Energies*, vol. 10, no. 9, Sep 2017.

- [77] M. J. Farooq, H. Ghazzai, A. Kadri, H. ElSawy, and M. S. Alouini, "A hybrid energy sharing framework for green cellular networks," *IEEE Transactions on Communications*, vol. 65, no. 2, pp. 918 – 934, Feb 2017.
- [78] M. J. Farooq, H. Ghazzai, A. Kadri, H. ElSawy, and M. S. Alouini, "Energy sharing framework for microgrid-powered cellular base stations," in *Proc. IEEE GLOBECOM*, Washington, DC USA, Dec 2016, pp. 1–7.
- [79] J. Xu and R. Zhang, "Cooperative energy trading in comp systems powered by smart grids," *IEEE Transactions on Vehicular Technology*, vol. 65, no. 4, pp. 2142 – 2153, Apr 2016.
- [80] J. Xu, L. Duan, and R. Zhang, "Cost-aware green cellular networks with energy and communication cooperation," *IEEE Communications Magazine*, vol. 53, no. 5, pp. 257 – 263, May 2015.
- [81] B. Xu, Y. Chen, J. Requena Carrion, J. Loo, and A. Vinel, "Energy-aware power control in energy cooperation aided millimeter wave cellular networks with renewable energy resources," *IEEE Access*, vol. 5, pp. 432 – 442, Dec 2017.
- [82] Y. K. Chia, S. Sun, and R. Zhang, "Energy cooperation in cellular networks with renewable powered base stations," *IEEE Transactions on Wireless Communications*, vol. 13, no. 12, pp. 6996 – 7010, Dec 2014.
- [83] J. N. V. Lucas, G. E. Francés, and E. S. M. González, "Energy security and renewable energy deployment in the EU: Liaisons dangereuses or virtuous circle?" *Renewable and Sustainable Energy Reviews*, vol. 62, pp. 1032 – 1046, Sep 2016.
- [84] X. Li, "Diversification and localization of energy systems for sustainable development and energy security," *Energy Policy*, vol. 33, no. 17, pp. 2237 – 2243, Nov 2005.

- [85] L. Cerović, D. Maradin, and S. Čegar, “From the restructuring of the power sector to diversification of renewable energy sources: Preconditions for efficient and sustainable electricity market,” *International Journal of Energy Economics and Policy*, vol. 4, no. 4, pp. 599 – 609, 2014.
- [86] J. Xu and R. Zhang, “CoMP meets smart grid: A new communication and energy cooperation paradigm,” *IEEE Transactions on Vehicular Technology*, vol. 64, no. 6, pp. 2476 – 2488, Jun 2015.
- [87] X. Huang and N. Ansari, “Energy sharing within EH-enabled wireless communication networks,” *IEEE Wireless Communications*, vol. 22, no. 3, pp. 144 – 149, Jun 2015.
- [88] X. Huang, T. Han, and N. Ansari, “Smart grid enabled mobile networks: Jointly optimizing BS operation and power distribution,” *IEEE ACM Transactions on Networking*, vol. 25, no. 3, pp. 1832 – 1845, June 2017.
- [89] T. E. Hoff and R. Perez, “Modeling PV fleet output variability,” *Solar Energy*, vol. 86, no. 8, pp. 2177 – 2189, Aug 2012.
- [90] J. Taylor, J. Leloux, A. Everard, J. Briggs, and A. Buckley, “Quantifying PV fleet output variability in the UK: Consequences for distribution network operators,” in *Proc. PVSAT-11*, Leeds, UK, Apr 2015.
- [91] H. Cole and D. Sang, *Revise AS Physics for AQA A*. Oxford, United Kingdom: Heinemann Educational Publishers, 2001, pp. 67–68.